



**Journal of
Mechanics of
Materials and Structures**

Volume 13, No. 2

March 2018



JOURNAL OF MECHANICS OF MATERIALS AND STRUCTURES

msp.org/jomms

Founded by Charles R. Steele and Marie-Louise Steele

EDITORIAL BOARD

ADAIR R. AGUIAR	University of São Paulo at São Carlos, Brazil
KATIA BERTOLDI	Harvard University, USA
DAVIDE BIGONI	University of Trento, Italy
MAENGHYO CHO	Seoul National University, Korea
HUILING DUAN	Beijing University
YIBIN FU	Keele University, UK
IWONA JASIUK	University of Illinois at Urbana-Champaign, USA
DENNIS KOCHMANN	ETH Zurich
MITSUTOSHI KURODA	Yamagata University, Japan
CHEE W. LIM	City University of Hong Kong
ZISHUN LIU	Xi'an Jiaotong University, China
THOMAS J. PENCE	Michigan State University, USA
GIANNI ROYER-CARFAGNI	Università degli studi di Parma, Italy
DAVID STEIGMANN	University of California at Berkeley, USA
PAUL STEINMANN	Friedrich-Alexander-Universität Erlangen-Nürnberg, Germany
KENJIRO TERADA	Tohoku University, Japan

ADVISORY BOARD

J. P. CARTER	University of Sydney, Australia
D. H. HODGES	Georgia Institute of Technology, USA
J. HUTCHINSON	Harvard University, USA
D. PAMPLONA	Universidade Católica do Rio de Janeiro, Brazil
M. B. RUBIN	Technion, Haifa, Israel

PRODUCTION production@msp.org

SILVIO LEVY Scientific Editor


Cover photo: Mando Gomez, www.mandolux.com

See msp.org/jomms for submission guidelines.

JoMMS (ISSN 1559-3959) at Mathematical Sciences Publishers, 798 Evans Hall #6840, c/o University of California, Berkeley, CA 94720-3840, is published in 10 issues a year. The subscription price for 2018 is US \$615/year for the electronic version, and \$775/year (+\$60, if shipping outside the US) for print and electronic. Subscriptions, requests for back issues, and changes of address should be sent to MSP.

JoMMS peer-review and production is managed by EditFLOW® from Mathematical Sciences Publishers.

PUBLISHED BY

 **mathematical sciences publishers**
nonprofit scientific publishing

<http://msp.org/>

© 2018 Mathematical Sciences Publishers

A SIMPLE TECHNIQUE FOR ESTIMATION OF MIXED MODE (I/II) STRESS INTENSITY FACTORS

SOMAN SAJITH, KONDEPUDI S. R. K. MURTHY AND PUTHUVEETIL S. ROBI

A simple and efficient finite element based technique using the crack face nodal displacements for the accurate estimation of mode I, mode II and mixed mode I/II stress intensity factors (SIF) is proposed in this paper. Finite element (FE) method is used to obtain the crack face nodal displacements of various cracked configurations. Convergence studies are conducted. The estimated SIFs are compared with the other techniques such as displacement extrapolation, J-integral, and interaction integral techniques, along with the published results. Results indicate that the proposed technique is found to be simple and provides accurate SIF even for the relatively coarser meshes. Results also indicate that the accuracy of the proposed technique is of the order of the path independent integrals in a given mesh. Further, the proposed technique also evaluates the sign of mode II SIF, K_{II} , which is vital in fatigue crack growth simulations.

1. Introduction

Stress intensity factor (SIF), K , proposed by Irwin [1957] plays a vital role in the strength and structural integrity assessment of cracked structures. It is used to describe the crack driving force, the level of singularity [Paris 2014], and the materials resistance to fracture. Further, it is also useful in fatigue crack growth studies. To this end, numerous analytical [Sih 1973], experimental [Ravi-Chandar 2008; Swamy et al. 2008; Kaushik et al. 2008], and numerical methods [Henshell and Shaw 1975; Barsoum 1976; Banks-Sills and Sherman 1986; Lim et al. 1992; Mukhopadhyay et al. 2000; Murthy and Mukhopadhyay 2001; Qian et al. 2016; Yan et al. 2010] are available for the SIF determination.

Analytical and semianalytical SIF solutions of some simple configurations are available in various handbooks [Tada et al. 2000; Murakami 1987; Laham 1999]. For complex configurations, numerical methods such as FE method and boundary element (BE) method are employed. Amongst the available numerical methods, FE method has been extensively used for accurately estimating SIFs of complex configurations. Other important areas which demand accurate estimation of the SIFs is FE simulations of quasistatic crack growths and fatigue crack growth in damage tolerance design philosophy. In these studies, a large number of finite element analyses of a given cracked configuration are necessary due to the incremental increase of the crack length. In such cases, it is cost effective if accurate SIFs are estimated for a given mesh in the simulation process. Moreover, the signs of individual SIFs are also important in estimating crack growth directions both in quasistatic and fatigue crack growth simulations.

In FE method, quarter point elements (QPEs) [Henshell and Shaw 1975; Barsoum 1976] are employed at the crack tip for modeling the crack tip inverse square root singularity. In relation to the QPEs and FE method, a number of SIF estimation techniques have also been developed. A review of some of these

Keywords: crack, stress intensity factor, fracture, fatigue, displacement, mixed mode.

commonly used techniques are available in works [Banks-Sills and Sherman 1986; Lim et al. 1992; Mukhopadhyay et al. 2000; Murthy and Mukhopadhyay 2001; Qian et al. 2016].

SIF estimation techniques (usually postprocessing techniques) are broadly classified into stress-based, displacement-based, and energy-based. The displacement-based techniques include: the limited displacement extrapolation technique by Lim et al. [1992], the displacement correlation technique [Tracey 1977], the displacement extrapolation techniques (DETs) [Chan et al. 1970; Shih et al. 1976; Rahulkumar et al. 1997; Guinea et al. 2000; ANSYS 2007; Kirthan et al. 2016], the quarter point displacement technique [Barsoum 1976; Henshell and Shaw 1975; Lim et al. 1992], and the interior collocation technique [Jogdand and Murthy 2010]. Some of the stress-based methods are the stress extrapolation [Chan et al. 1970] and the force method [Raju and Newman, Jr. 1977]. Examples of energy-based SIF extraction methods are the modified crack closure integral [Ramamurthy et al. 1986; Rybicki and Kanninen 1977; Sethuraman and Maiti 1988], virtual crack closure integral [Rybicki and Kanninen 1977; Shivakumar et al. 1988], J-integral [Rice 1968], stiffness derivative [Parks 1974], virtual crack extension [Hellen 1975], and interaction integral (I-integral) [Nakamura 1991; Shih et al. 1986].

Amongst the above methods, J-integral, interaction integral, and a kind of DET are integrated in various commercial software such as ANSYS and ABAQUS. Although the path independent integral techniques (J-integral and interaction integral) neatly avoid crack tip complications, they only provide accurate solutions of the SIFs by computing over several paths, which complicates the mesh generation process. The interior collocation technique [Jogdand and Murthy 2010], although it provides accurate values of the SIFs, demands a special mesh pattern around the crack tip. As a consequence, these are difficult to implement into the existing FE codes. On the other hand, techniques such as stiffness derivative and virtual crack extension require calculation of the structural stiffness matrix twice, which increases the computational cost. It is evident that the above techniques, apart from being difficult to incorporate into the existing codes, are also not very appropriate for employment in the crack growth simulations where large numbers of analysis steps are usually needed.

While the displacement-based techniques are simple and easy to implement into existing FE codes (they demand no other than quarter point elements), techniques such as displacement correlation [Tracey 1977] and quarter point displacement techniques [Barsoum 1976; Henshell and Shaw 1975; Lim et al. 1992] do not show convergence as the meshes are refined [Murthy and Mukhopadhyay 2001]. Clearly, use of these techniques is prohibitive especially in crack growth simulations. Coming to the case of displacement extrapolation methods, a form of displacement extrapolation was first proposed by Chan et al. [1970], which has the limitation of carrying out regression analysis for best-fit straight line. Subsequently, many variants of displacement extrapolation techniques have been proposed in the past [Shih et al. 1976; Rahulkumar et al. 1997; Guinea et al. 2000; ANSYS 2007; Kirthan et al. 2016].

The above extrapolation methods have been devised based on two types of formulations. In the first type of formulations [Rahulkumar et al. 1997; ANSYS 2007], the crack opening displacement (COD) and crack sliding displacement (CSD) are approximated using the singular solutions and these displacements are approximated using an assumed profile (containing singular and higher-order displacements) fitted to the edges of the finite elements attached to crack flanks. In the second type of formulation, the relative displacement of nodes on one of the two flanks of the crack were expressed in terms of known analytical expressions containing singular and higher-order terms and obtained the SIFs by correlating these expressions with the elemental displacement field [Shih et al. 1976; Guinea et al. 2000; Kirthan et al.

2016]. It has been shown using extensive numerical analyses that the techniques based on the second type of formulation [Shih et al. 1976; Guinea et al. 2000; Kirthan et al. 2016] do not converge as the meshes are refined [Murthy and Mukhopadhyay 2001]. Clearly, these existing displacement techniques are not reliable when estimating SIFs of complex configurations or during fatigue crack propagation simulations. A technique based on the first type of formulation is implemented in commercial software ANSYS, and although it estimates accurate values of the SIFs, it has a major limitation of not providing the signs of the SIFs, which are extremely important in fatigue crack growth simulations.

In view of the importance of accurately estimating SIFs along with their signs and various limitations of the existing SIF extraction methods (as described above), a new simple and efficient displacement extrapolation-type technique, which also provides signs of the estimated SIFs, is proposed in the present investigation. This work takes the advantage of both the types of formulations implemented in the existing techniques [Shih et al. 1976; Zhu and Smith 1995; Rahul Kumar et al. 1997] and formulates the COD and CSD using a combination of singular and higher-order terms. Due to the presence of higher-order terms, the technique can be used on coarse meshes to get the accurate values of SIFs. The mixed mode SIFs are then estimated directly by comparing the analytical expressions of COD and CSD with the computed values obtained at the nodes of the crack flanks. Further, the proposed technique employs the more elegant approach of the Generalized Westergaard proposed by Sanford [1979]. It is very easy to implement into the existing FE codes and provides very accurate SIFs even in the relatively course meshes. The solutions of the proposed technique converge as the meshes are refined. The efficacy of the proposed technique is substantiated by solving the SIFs of mode I, mode II, and mixed mode (I/II) benchmark problems and comparing the results with the values computed using J-integral and interaction integral and published results.

The organization of the paper is as follows. Section 2 describes the mathematical background and implementation steps of the proposed technique. Numerical validation of the proposed technique using benchmark problems is presented in Section 3. Finally, Section 4 presents the summary and conclusions.

2. Theoretical background

In the generalized Westergaard method [Sanford 1979], the modified Airy stress function for opening mode (ϕ_I) and shear mode (ϕ_{II}) are respectively given by

$$\phi_I = \text{Re}\bar{\bar{Z}}_I(z) + y\text{Im}\bar{\bar{Z}}_I(z) + y\text{Im}\bar{Y}_I(z), \quad \phi_{II} = -y\text{Re}\bar{\bar{Z}}_{II}(z) + \text{Im}\bar{Y}_{II}(z) - y\text{Re}\bar{Y}_{II}(z), \quad (1)$$

where

$$\frac{d\bar{\bar{Z}}_i}{dz} = \bar{\bar{Z}}_i, \quad \frac{d\bar{Z}_i}{dz} = Z_i, \quad i = \text{I, II}. \quad (2)$$

The complex analytic functions for opening mode ($Z_I(z)$, $Y_I(z)$) and those for shearing mode ($Z_{II}(z)$, $Y_{II}(z)$) are defined as

$$\begin{aligned} Z_I(z) &= \sum_{n=0}^{\infty} A_n Z^{n-1/2} \quad \text{and} \quad Y_I(z) = \sum_{m=0}^{\infty} B_m Z^m, \\ Z_{II}(z) &= \sum_{n=0}^{\infty} C_n Z^{n-1/2} \quad \text{and} \quad Y_{II}(z) = \sum_{m=0}^{\infty} D_m z^m. \end{aligned} \quad (3)$$

These are series-type functions in terms of the complex variable $z = x + iy$ ($z = x \cos \theta + iy \sin \theta$ in polar coordinates; see [Figure 1](#)) containing an infinite number of opening mode and shear mode ($A_0, A_1, \dots, A_\infty; B_0, B_1, \dots, B_\infty$) and shear coefficients ($C_0, C_1, \dots, C_\infty; D_0, D_1, \dots, D_\infty$). These coefficients are functions of the geometry and boundary conditions of a cracked configuration. Using Cauchy–Riemann relations and the modified Airy stress function (1), the stress components for mode I in the absence of body forces can be written as

$$\begin{Bmatrix} \sigma_{xx} \\ \sigma_{yy} \\ \tau_{xy} \end{Bmatrix} = \begin{Bmatrix} \operatorname{Re}Z_I - y\operatorname{Im}Z'_I - y\operatorname{Im}Y'_I + 2\operatorname{Re}Y_I \\ \operatorname{Re}Z_I + y\operatorname{Im}Z'_I + y\operatorname{Im}Y'_I \\ y\operatorname{Re}Z'_I - y\operatorname{Re}Y'_I - \operatorname{Im}Y_I \end{Bmatrix}, \quad (4)$$

and the stress components for mode II can be written as

$$\begin{Bmatrix} \sigma_{xx} \\ \sigma_{yy} \\ \tau_{xy} \end{Bmatrix} = \begin{Bmatrix} y\operatorname{Re}Z'_{II} + 2\operatorname{Im}Z_{II} + y\operatorname{Re}Y'_{II} + \operatorname{Im}Y_{II} \\ -y\operatorname{Re}Z'_{II} - y\operatorname{Re}Y'_{II} + \operatorname{Im}Y_{II} \\ \operatorname{Re}Z_{II} - y\operatorname{Im}Z'_{II} - y\operatorname{Im}Y'_{II} \end{Bmatrix}. \quad (5)$$

Integrating the strain components, the displacement components in terms of three parameters (A_0, A_1 , and B_0) for mode I can be shown to be

$$\begin{aligned} u^I &= \frac{A_0}{2G} r^{1/2} [(\kappa - 1) \cos \frac{1}{2}\theta + \sin \theta \sin \frac{1}{2}\theta] \\ &\quad + \frac{A_1}{2G} r^{3/2} \left[\frac{1}{3}(\kappa - 1) \cos \frac{3}{2}\theta - \sin \theta \sin \frac{1}{2}\theta \right] + \frac{B_0(\kappa + 1)}{4G} r \cos \theta, \\ v^I &= \frac{A_0}{2G} r^{1/2} [(\kappa + 1) \sin \frac{1}{2}\theta - \sin \theta \cos \frac{1}{2}\theta] \\ &\quad + \frac{A_1}{2G} r^{3/2} \left[\frac{1}{3}(\kappa + 1) \sin \frac{3}{2}\theta - \sin \theta \cos \frac{1}{2}\theta \right] - \frac{B_0\nu(\kappa + 1)}{4G} r \sin \theta, \end{aligned} \quad (6)$$

where u^I and v^I represent the mode I displacements in x and y directions, respectively ([Figure 1](#)) and $\kappa = 3 - 4\nu$ for plane strain and $(3 - \nu)/(1 + \nu)$ for plane stress conditions. In a similar way the displacement components in terms of three parameters (C_0, C_1 and D_0) for mode II can be obtained as

$$\begin{aligned} u^{II} &= \frac{C_0}{2G} r^{1/2} [(\kappa + 1) \sin \frac{1}{2}\theta + \sin \theta \cos \frac{1}{2}\theta] \\ &\quad + \frac{C_1}{2G} r^{3/2} \left[\frac{1}{3}(\kappa + 1) \sin \frac{3}{2}\theta + \sin \theta \cos \frac{1}{2}\theta \right] + \frac{D_0(\kappa + 1)}{4G} 4 \sin \theta, \\ v^{II} &= \frac{C_0}{2G} r^{1/2} [(1 - \kappa) \cos \frac{1}{2}\theta + \sin \theta \sin \frac{1}{2}\theta] \\ &\quad + \frac{C_1}{2G} r^{3/2} \left[\frac{1}{3}(1 - \kappa) \cos \frac{3}{2}\theta - \sin \theta \sin \frac{1}{2}\theta \right] - \frac{D_0(\kappa + 1)}{4G} 4 \cos \theta, \end{aligned} \quad (7)$$

where u^{II}, v^{II} are mode II displacements ([Figure 1](#)). Here, G and ν are the shear modulus and Poisson's ratio, respectively. Also, A_0, A_1, B_0 and C_0, C_1, D_0 represent coefficients of the Generalized Westergaard [[Sanford 1979](#)] in mode I and mode II, respectively. In the case of mixed mode (I/II) loading, the displacement components can be obtained using the principle of superposition as

$$u = u^I + u^{II}, \quad v = v^I + v^{II}. \quad (8)$$

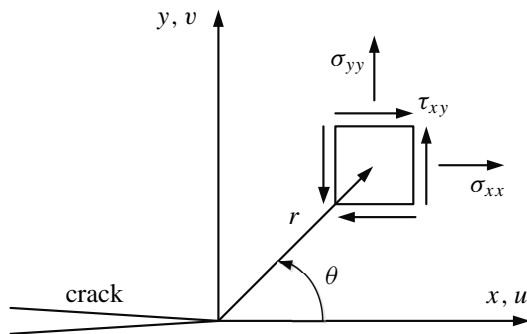


Figure 1. Crack tip coordinate system.

Figure 2 shows a typical crack tip mesh pattern with the QPEs deployed at the crack tip. The nodes 1 and 2 represent quarter point nodes on the crack flanks (with node 1 being at $\theta = +180^\circ$ and node 2 at $\theta = -180^\circ$, respectively), and nodes 3 and 4 represent corner nodes of the QPEs attached to the crack flanks. It is assumed that (7) and (8) are sufficient to represent the displacement components along the length of the QPEs lying on the crack flanks in any loading. Referring to Figure 2, for $\theta = \pm 180^\circ$ the v component of the displacement in mixed mode loading conditions is given as

$$\begin{aligned} v_{180^\circ} &= \frac{A_0(\kappa + 1)}{2G} r^{1/2} - \frac{A_1(\kappa + 1)}{6G} r^{3/2} + \frac{D_0(\kappa + 1)}{4G} r, \\ v_{-180^\circ} &= -\frac{A_0(\kappa + 1)}{2G} r^{1/2} + \frac{A_1(\kappa + 1)}{6G} r^{3/2} + \frac{D_0(\kappa + 1)}{4G} r. \end{aligned} \quad (9)$$

Similarly the u component of the displacement is given as

$$\begin{aligned} u_{180^\circ} &= \frac{C_0(\kappa + 1)}{2G} r^{1/2} - \frac{C_1(\kappa + 1)}{6G} r^{3/2} - \frac{B_0(\kappa + 1)}{4G} r, \\ u_{-180^\circ} &= -\frac{C_0(\kappa + 1)}{2G} r^{1/2} + \frac{C_1(\kappa + 1)}{6G} r^{3/2} - \frac{B_0(\kappa + 1)}{4G} r. \end{aligned} \quad (10)$$

Therefore, from (9) and (10), the COD (Δv) and CSD (Δu) under mixed mode I/II can be written as

$$\begin{aligned} \Delta v &= v_{180^\circ} - u_{-180^\circ} = \frac{A_0(\kappa + 1)}{G} r^{1/2} - \frac{A_1(\kappa + 1)}{3G} r^{3/2}, \\ \Delta u &= u_{180^\circ} - u_{-180^\circ} = \frac{C_0(\kappa + 1)}{G} r^{1/2} - \frac{C_1(\kappa + 1)}{3G} r^{3/2}. \end{aligned} \quad (11)$$

In the present investigation the unknown coefficients A_0 and C_0 are solved using the FE solutions of Δv and Δu at two different radial locations r_1 (or r_2) and r_3 (or r_4) on the crack flank as shown in Figure 2. Then the mixed mode SIFs K_I and K_{II} can be estimated as

$$K_I = \sqrt{2\pi} A_0 \quad \text{and} \quad K_{II} = \sqrt{2\pi} C_0. \quad (12)$$

It can be noticed from (11) and (12) that actual signs (positive or negative) of the SIFs (which depend on the orientation of the crack with the loading) can also be furnished by the proposed technique.

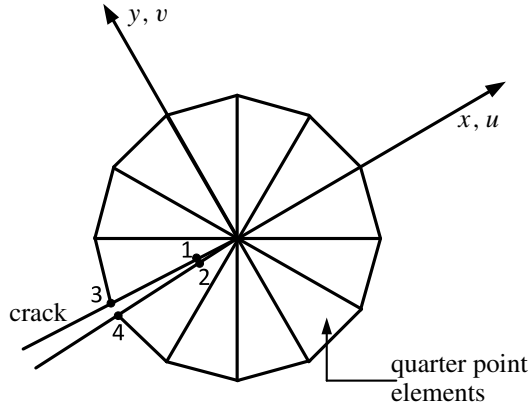


Figure 2. Crack tip coordinate system and associated displacements.

3. Numerical examples

In order to validate the performance of the proposed technique, numerical evaluation is carried out in this section using a number of benchmark problems. Finite element analysis of all the examples is carried out using the commercial software ANSYS. Meshing is done using eight noded isoparametric quadrilateral (Q8) elements and collapsed Q8 QPEs are employed at the crack tip in a spider web pattern. Plane stress condition, Young's modulus $E = 1.0$, Poisson's ratio $\nu = 0.3$, and the applied stress $\sigma = 1.0$ are assumed in all the example problems. Units of all examples are consistent. SIFs are also computed using the DET available in ANSYS, the J-integral and I-integral techniques. In order to study the efficacy of the proposed technique, these values along with the published solutions are compared with those obtained using the present technique. The percentage relative error in the estimated SIF is calculated as

$$\% \text{ relative error} = \left| \frac{\text{computed value} - \text{reference value}}{\text{reference value}} \right| \times 100, \quad (13)$$

where computed value refers to the value of SIF estimated using the proposed technique and the reference value is the available analytical or numerical value.

3.1. Example 1: center-cracked plate subjected to uniform tension. The first example discussed here is a mode I problem of a center-cracked plate (CCP) under uniform tensile loading (Figure 3a) with $h/b = 3$. Three configurations with $a/b = 0.2, 0.4$ and 0.6 have been considered for the study. Due to symmetry, only one quarter of the CCP is simulated (shaded area in Figure 3a). Figure 3a also shows symmetry boundary conditions used in the FE analysis. Figure 4 shows a sequence of finite element meshes employed for convergence study for the configuration with $a/b = 0.4$ and with the QPE length to crack length ratio (L_Q/a) of $0.4, 0.2,$ and $0.1,$ respectively. The number of elements (NE) and number of nodes (NN) are also shown in Figure 4. The mesh pattern around the crack tip is shown in Figure 4d.

Table 1 shows the results of the estimated normalized SIF obtained using the proposed approach and other techniques. The values given in parentheses indicates the percentage relative error based on the reference solutions given by Isida [1971] in (13).

It can be noticed from Table 1 that the results obtained using the proposed technique converges to the reference value with the mesh refinement. This is true for all a/b values considered. It is interesting to

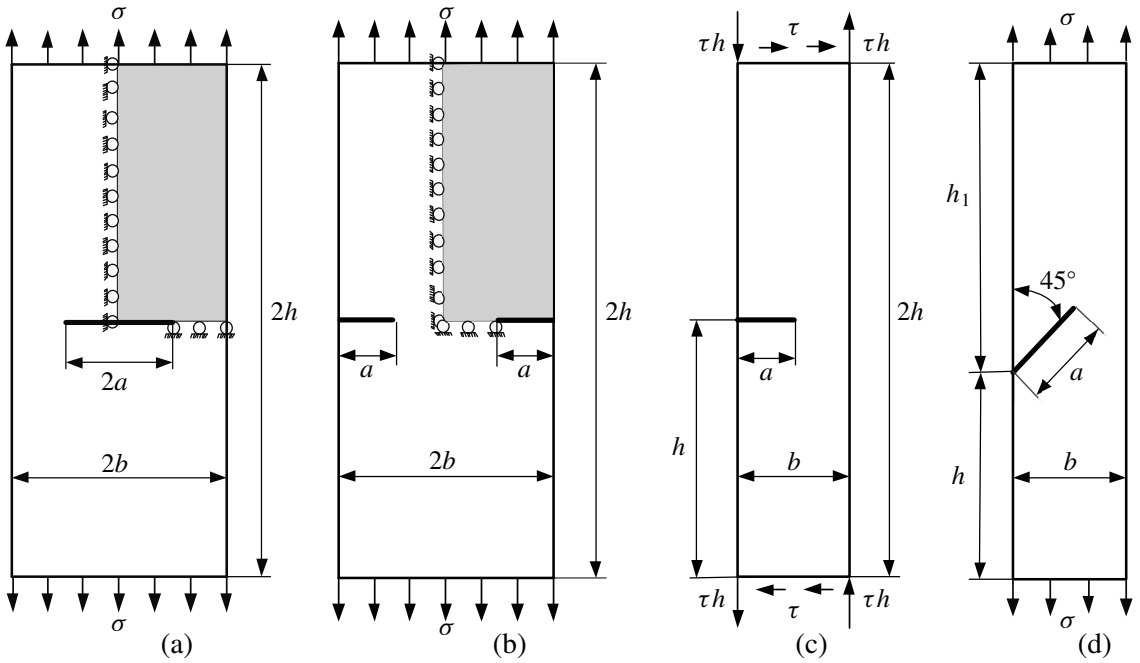


Figure 3. Geometry and boundary conditions for the various crack configurations.

a/b	Mesh	$K_I/\sigma\sqrt{\pi a}$				
		[Isida 1971]	Present	DET	J-int	I-int
0.2	Mesh 1		1.0272 (0.21)	1.0272 (0.22)	1.0246 (0.04)	1.0249 (0.01)
	Mesh 2	1.025	1.0263 (0.13)	1.0264 (0.13)	1.0246 (0.04)	1.0246 (0.04)
	Mesh 3		1.0258 (0.08)	1.0258 (0.07)	1.0246 (0.04)	1.0246 (0.04)
0.4	Mesh 1		1.1120 (0.27)	1.1120 (0.27)	1.1094 (0.03)	1.1097 (0.06)
	Mesh 2	1.109	1.1109 (0.17)	1.1109 (0.17)	1.1094 (0.03)	1.1093 (0.03)
	Mesh 3		1.1105 (0.14)	1.1105 (0.14)	1.1094 (0.03)	1.1093 (0.03)
0.6	Mesh 1		1.3052 (0.17)	1.3052 (0.17)	1.3033 (0.02)	1.3037 (0.05)
	Mesh 2	1.303	1.3047 (0.13)	1.3046 (0.13)	1.3033 (0.02)	1.3033 (0.02)
	Mesh 3		1.3044 (0.11)	1.3045 (0.12)	1.3033 (0.02)	1.3033 (0.02)

Table 1. Comparison of normalized SIFs for CCP ($h/b = 3$, $a/b = 0.2, 0.4, 0.6$). Numbers in parentheses are the percentage relative error.

notice from the results in [Table 1](#) that in all the meshes, the SIFs are determined with an accuracy that is comparable with that obtained using J-integral and I-integral. Very accurate SIFs are estimated using the proposed technique even in the relatively course meshes. The maximum percentage error observed using coarse meshes (Mesh 1) is 0.27% and using fine meshes (Mesh 3) is 0.14%. It can also be noticed that the results obtained in this section are in excellent agreement with the reference value and the proposed technique computes very accurate values of the SIFs.

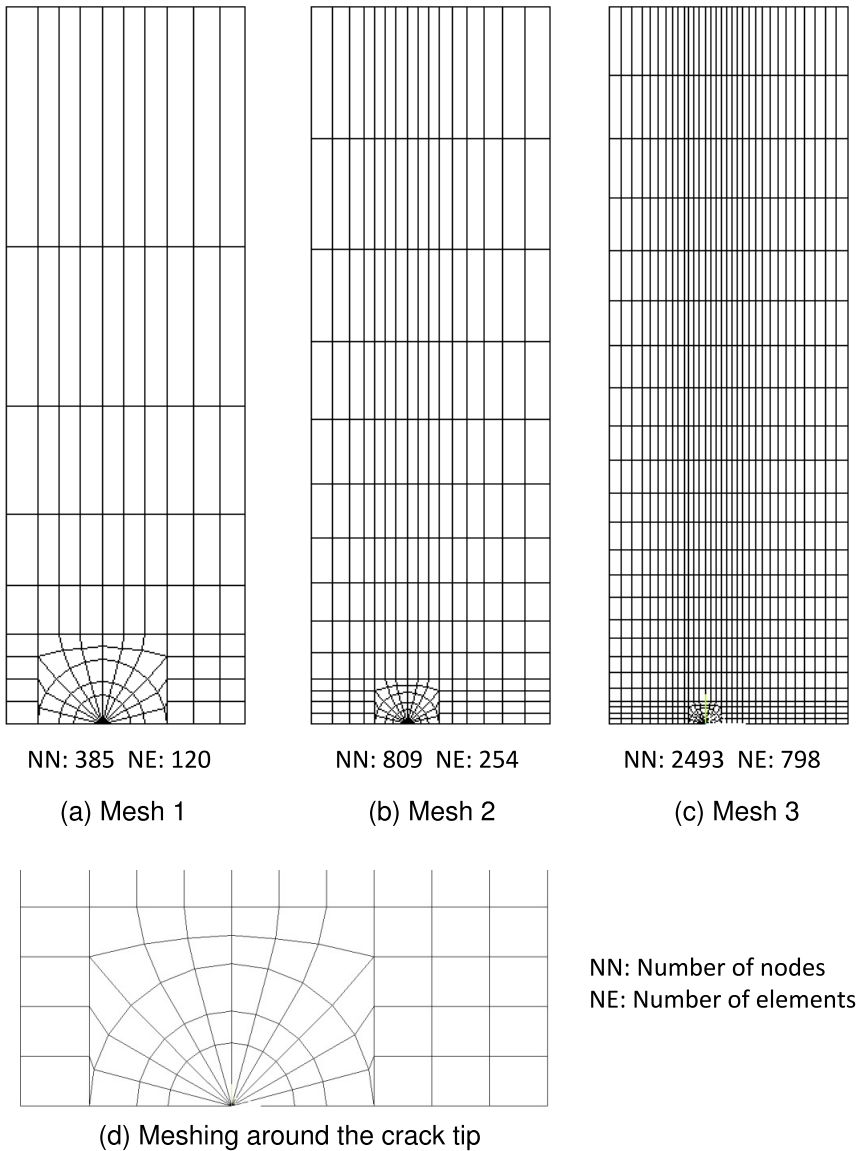


Figure 4. Different finite element meshes used for the analysis of CCP. Top: Mesh 1, Mesh 2, and Mesh 3. Bottom: meshing around the tip.

3.2. Example 2: double edge cracked plate subjected to uniform tension. The second problem considered is also a mode I problem of double edge cracked plate (DECP) subjected to uniform far-field tensile stresses as shown in Figure 3b. The geometry parameters used for the FE analysis are $h/b = 3$, $a/b = 0.2, 0.4$, and 0.6 . Only one quarter of the plate is modeled as shown (with boundary conditions) in Figure 3b due to the symmetry of the problem. Meshes that are similar to Figure 4 are employed for the FE analysis. However, results corresponding to the Mesh 1 and Mesh 3 are presented here. Table 2 shows

a/b	Mesh	$K_{I/\sigma} \sqrt{\pi a}$					
		Reference 1	Reference 2	Present	DET	J-int	I-int
0.2	Mesh 1	1.1180	1.1123	1.1104 (0.68)	1.1105 (0.67)	1.1118 (0.56)	1.1121 (0.53)
	Mesh 3			1.1124 (0.50)	1.1124 (0.50)	1.1118 (0.56)	1.1117 (0.56)
0.4	Mesh 1	1.1361	1.1377	1.1309 (0.46)	1.1309 (0.46)	1.1321 (0.35)	1.1325 (0.32)
	Mesh 3			1.1329 (0.28)	1.1329 (0.28)	1.1321 (0.35)	1.1321 (0.35)
0.6	Mesh 1	1.2333	1.2446	1.2361 (0.23)	1.2362 (0.23)	1.2360 (0.22)	1.2364 (0.25)
	Mesh 3			1.2371 (0.30)	1.2371 (0.30)	1.2360 (0.22)	1.2360 (0.22)

Table 2. Comparison of normalized SIFs for DECP ($h/b = 3$, $a/b = 0.2, 0.4, 0.6$). Reference 1 is [Benthem and Koiter 1973], and reference 2 is [Yan et al. 2010]. Numbers in parentheses are the percentage relative error.

the comparison of computed mode I normalized SIFs using the proposed approach and other techniques. The % relative error is shown in parentheses. Solutions of [Benthem and Koiter 1973] are considered as the reference solution in (13).

It is seen that the results of present displacement based method are in very good agreement with the results using the other three methods and the published results in all the meshes. Like in the previous example, the estimated SIF is converged as the meshes are refined and very accurate solutions are determined even in relatively coarse meshes such as Mesh 1. This is true for all a/b values considered. The solutions of the proposed technique are comparable to that of path independent integral techniques. The maximum error using Mesh 1 is 0.68%, and that in Mesh 3 is 0.56%.

3.3. Example 3: edge-cracked plate subjected to pure antisymmetric loading. In this section, a pure mode II problem of an edge-cracked plate under antisymmetric loading is presented as shown in Figure 3c. For this problem h/b is set to 1.0 and different configurations with $a/b = 0.2, 0.4$, and 0.6 have been analyzed. As no symmetry exists in this problem, the full model is considered in FE analysis. The bottom edge of the plate is restrained from all degrees of freedom and the top face is loaded with the forces as shown in Figure 3c. Like in previous examples, the convergence of computed mode II SIF K_{II} using the proposed technique is observed along three meshes with varying mesh density as shown in Figure 5 and the corresponding results are presented in Table 3. For the % relative error calculations in normalized SIF, results of [Treifi et al. 2008] are considered as the reference solution.

It may be observed from the results of Table 3 that similar to the previous example, extremely accurate values of the mode II SIFs are extracted by the proposed method and are converged as the meshes are refined. This can be seen in all a/b values employed. The results obtained using Mesh 3 are in very good agreement with the published results as well as with the other methods. In this example also the accuracy of the proposed method is similar to the J-integral and I-integral techniques. A maximum error of 0.56% is noticed in Mesh 1 of $a/b = 0.4$. However with the fine meshes (Mesh 3), the maximum error is 0.51%.

3.4. Example 4: slant edge cracked plate subjected to tensile loads. Finally, to demonstrate the efficacy of the proposed method in mixed mode (I/II) loading conditions, a slant edge cracked plate (SECP)

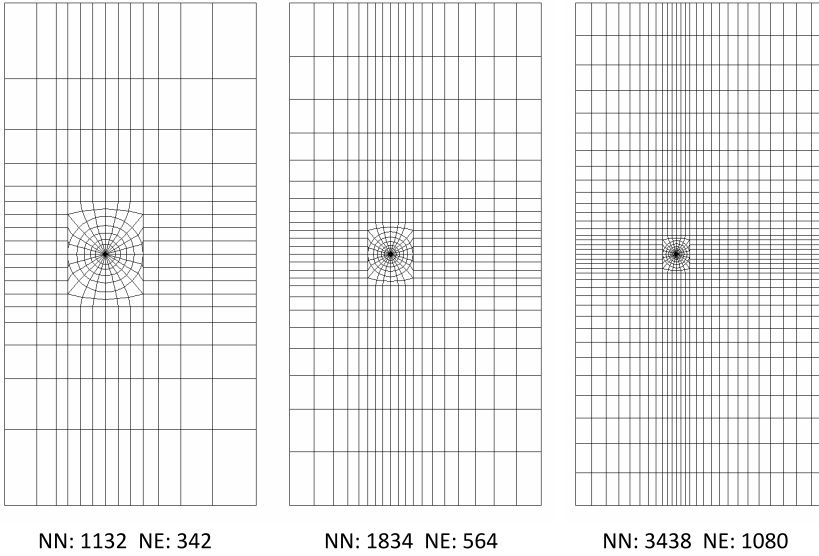


Figure 5. Finite element meshes used for analysis of ECP under mode II loading: Mesh 1 (left), Mesh 2 (middle), and Mesh 3 (right).

a/b	Mesh	$K_{II}/\tau\sqrt{\pi a}$				
		[Treifi et al. 2008]	Present	DET	J-int	I-int
0.2	Mesh 1		0.6906 (0.49)	0.6906 (0.49)	0.7065 (1.79)	0.7039 (1.43)
	Mesh 2	0.694	0.6887 (0.77)	0.6883 (0.82)	0.6960 (0.29)	0.6960 (0.29)
	Mesh 3		0.6905 (0.51)	0.6905 (0.50)	0.6959 (0.27)	0.6959 (0.27)
0.4	Mesh 1		1.1718 (0.56)	1.1718 (0.56)	1.1794 (0.03)	1.1798 (0.06)
	Mesh 2	1.179	1.1739 (0.40)	1.1740 (0.38)	1.1794 (0.03)	1.1794 (0.03)
	Mesh 3		1.1748 (0.33)	1.1752 (0.29)	1.1794 (0.03)	1.1794 (0.03)
0.6	Mesh 1		1.5468 (0.33)	1.5466 (0.34)	1.5503 (0.11)	1.5507 (0.08)
	Mesh 2	1.552	1.5469 (0.32)	1.5471 (0.31)	1.5509 (0.07)	1.5509 (0.07)
	Mesh 3		1.5474 (0.29)	1.5473 (0.30)	1.5510 (0.06)	1.5510 (0.06)

Table 3. Normalized mode II stress intensity factors for ECP ($h/b = 1$, $a/b = 0.2, 0.4, 0.6$). Numbers in parentheses are the percentage relative error.

subjected to tension loads (as shown in Figure 3d) is considered here. The geometric parameters for this problem are $h/b = 1.0$, $h_1/h = 1.5$, and $a/b = 0.3, 0.4, 0.6$. Due to lack of symmetry, the whole domain is modeled using finite elements. The bottom face of the plate is restrained in the x and y directions and the top face is loaded as shown in Figure 3d. The convergence study has also been carried out using the three meshes with varying mesh density as shown in Figure 6. Tables 4 and 5 show the results of the analyses for the normalized K_I and K_{II} , respectively.

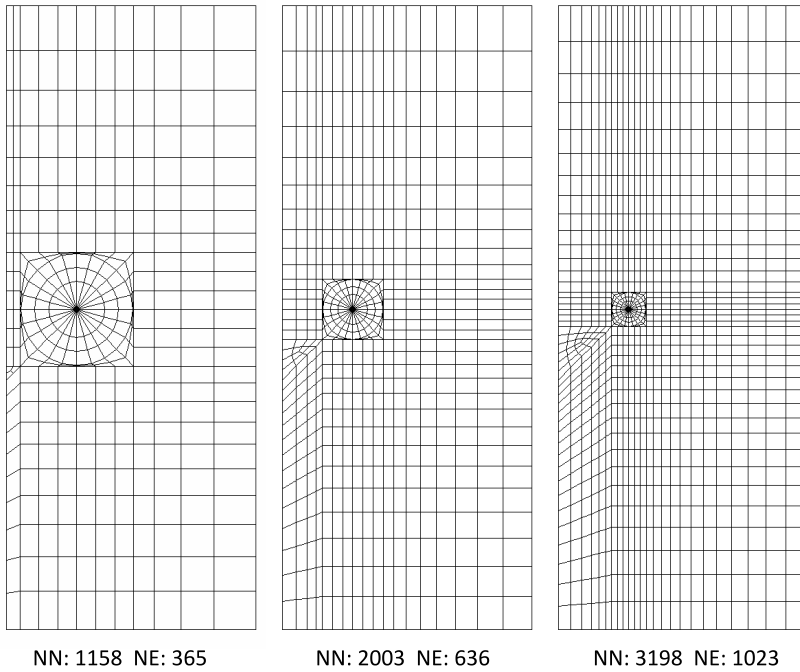


Figure 6. Finite element meshes used for the analysis of SECP under tension: Mesh 1 (left), Mesh 2 (middle), and Mesh 3 (right).

a/b	Mesh	$K_I/\sigma\sqrt{\pi a}$				
		[Chen and Wang 2008]	[Wilson 1969]	Present	DET	I-int
0.3	Mesh 1			0.8811 (0.21)	0.8811 (0.22)	0.8828 (0.02)
	Mesh 2	0.883	0.883	0.8821 (0.10)	0.8826 (0.05)	0.8826 (0.04)
	Mesh 3			0.8830 (0.00)	0.8831 (0.01)	0.8826 (0.04)
0.4	Mesh 1			1.0155 (0.15)	1.0155 (0.15)	1.0177 (0.07)
	Mesh 2	1.017	1.011	1.0175 (0.05)	1.0177 (0.07)	1.0176 (0.06)
	Mesh 3			1.0178 (0.08)	1.0179 (0.09)	1.0177 (0.07)
0.6	Mesh 1			1.4584 (0.04)	1.4584 (0.04)	1.4590 (0.00)
	Mesh 2	1.459	1.437	1.4595 (0.03)	1.4596 (0.04)	1.4590 (0.00)
	Mesh 3			1.4596 (0.04)	1.4598 (0.05)	1.4590 (0.00)

Table 4. Normalized mode I stress intensity factors for SECP under tension ($h/b = 1$, $h_1/h = 1.5$, $a/b = 0.3, 0.4, 0.6$). Numbers in parentheses are the percentage relative error.

It is very interesting to notice from the results of Tables 4 and 5 that like the previous examples, very accurate values of both the SIFs K_I and K_{II} have been estimated by the present technique. The percent relative error in present results are of the similar order as that of path independent integrals specifically in the refined meshes. Furthermore, convergence of the extracted SIFs can be noticed from Tables 4 and 5

a/b	Mesh	$K_{II}/\sigma\sqrt{\pi a}$				
		[Chen and Wang 2008]	[Wilson 1969]	Present	DET	I-int
0.3	Mesh 1			0.4383 (2.17)	0.4381 (2.20)	0.4469 (0.24)
	Mesh 2	0.448	0.450	0.4423 (1.27)	0.4425 (1.24)	0.4466 (0.30)
	Mesh 3			0.4441 (0.88)	0.4443 (0.84)	0.4466 (0.31)
0.4	Mesh 1			0.4955 (2.28)	0.4955 (2.27)	0.5055 (0.30)
	Mesh 2	0.507	0.505	0.5012 (1.15)	0.5010 (1.19)	0.5051 (0.38)
	Mesh 3			0.5021 (0.98)	0.5020 (0.99)	0.5051 (0.38)
0.6	Mesh 1			0.6782 (1.00)	0.6782 (0.99)	0.6833 (0.24)
	Mesh 2	0.685	0.674	0.6806 (0.64)	0.6805 (0.66)	0.6831 (0.27)
	Mesh 3			0.6807 (0.62)	0.6808 (0.61)	0.6831 (0.27)

Table 5. Normalized mode II stress intensity factors for SECP under tension ($h/b = 1$, $h_1/h = 1.5$, $a/b = 0.3, 0.4, 0.6$). Numbers in parentheses are the percentage relative error.

as the meshes are refined. The results in tables clearly show that the proposed technique is capable of providing accurate the mixed mode SIFs even in the relatively coarse meshes similar to that of J- and I-integrals. Solutions of [Chen and Wang 2008] are considered as the reference solutions in (13).

4. Conclusions

A simple and efficient displacement extrapolation technique for estimating mode I, mode II, and mixed mode (I/II) loading conditions is proposed in the present investigation. The technique uses the crack face displacement components from finite element analysis to compute the mode I, mode II, and mixed mode I/II SIFs. The technique is developed based on the Generalized Westergaard approach. The results of the present investigation clearly show that:

- the present technique provides very accurate SIFs even in the relatively coarse meshes,
- the estimated SIFs show convergence as the meshes are refined,
- the estimated SIFs show very good agreement with the published results and those results computed using the J-integral and I-integral, and
- the accuracy of the SIFs estimated using the proposed technique is of similar order as those obtained using path-independent integrals.

Apart from the accuracy of SIFs, another important feature of the proposed technique is that it provides the SIFs with their correct sign, which is vital in fatigue crack growth simulation studies in damage tolerance design philosophy. Thus the present technique is also extremely useful in fatigue crack growth simulations. Owing to the simplicity and ease of implementation, the present method can easily be incorporated into the existing FE codes.

References

- [ANSYS 2007] “Theory reference manual”, software manual, ANSYS, 2007, Available at <http://www.oalib.com/references/7196604>. Release 11.0.
- [Banks-Sills and Sherman 1986] L. Banks-Sills and D. Sherman, “Comparison of methods for calculating stress intensity factors with quarter-point elements”, *Int. J. Fract.* **32** (1986), 127–140.
- [Barsoum 1976] R. S. Barsoum, “On the use of isoparametric finite elements in linear fracture mechanics”, *Int. J. Numer. Methods Eng.* **10** (1976), 25–37.
- [Benthem and Koiter 1973] J. P. Benthem and W. T. Koiter, *Methods of analysis and solutions of crack problems*, vol. 1, edited by G. C. Sih, Springer, Dordrecht, The Netherlands, 1973.
- [Chan et al. 1970] S. K. Chan, I. S. Tuba, and W. K. Wilson, “On the finite element method in linear fracture mechanics”, *Eng. Fract. Mech.* **2** (1970), 1–17.
- [Chen and Wang 2008] C. H. Chen and C. L. Wang, “Stress intensity factors and T-stresses for offset double edge-cracked plates under mixed-mode loadings”, *Int. J. Fract.* **152** (2008), 149–162.
- [Guinea et al. 2000] G. V. Guinea, J. Planas, and M. Elices, “KI evaluation by the displacement extrapolation technique”, *Eng. Fract. Mech.* **66** (2000), 243–255.
- [Hellen 1975] T. K. Hellen, “On the method of virtual crack extensions”, *Int. J. Numer. Methods Eng.* **9** (1975), 187–207.
- [Henshell and Shaw 1975] R. D. Henshell and K. G. Shaw, “Crack tip finite elements are unnecessary”, *Int. J. Numer. Methods Eng.* **9** (1975), 495–507.
- [Irwin 1957] G. Irwin, “Analysis of stresses and strains near the end of a crack transversing a plate”, *J. Appl. Mech. (ASME)* **24** (1957), 361–370.
- [Isida 1971] M. Isida, “Effect of width and length on stress intensity factors of internally cracked plates under various boundary conditions”, *Int. J. Fract. Mech.* **7** (1971), 301–316.
- [Jogdand and Murthy 2010] P. V. Jogdand and K. S. R. K. Murthy, “A finite element based interior collocation method for the computation of stress intensity factors and T-stresses”, *Eng. Fract. Mech.* **77** (2010), 1116–1127.
- [Kaushik et al. 2008] B. Kaushik, K. S. R. K. Murthy, and P. S. Robi, “Determination of strain gage locations for the accurate measurement of opening mode stress intensity factors”, *J. Mech. Mater. Struct.* **3** (2008), 1757–1771.
- [Kirthan et al. 2016] L. J. Kirthan, R. Hegde, V. A. Girisha, and R. G. Kumar, “Evaluation of mode I stress intensity factor for edge crack using displacement extrapolation method”, *Int. J. Mater. Struct. Integrity* **10** (2016), 11–22.
- [Laham 1999] A. Laham, *Stress intensity factor and limit load handbook*, British Energy Generation Ltd., Gloucester, UK, 1999.
- [Lim et al. 1992] I. L. Lim, I. W. Johnston, and S. K. Choi, “Comparison between various displacement-based stress intensity factor computation techniques”, *Int. J. Fract.* **58** (1992), 193–210.
- [Mukhopadhyay et al. 2000] N. K. Mukhopadhyay, S. K. Maiti, and A. Kakodkar, “A review of SIF evaluation and modelling of singularities in BEM”, *Comput. Mech.* **25** (2000), 358–375.
- [Murakami 1987] Y. Murakami, *Stress intensity factors handbook*, Pergamon, 1987.
- [Murthy and Mukhopadhyay 2001] K. S. R. K. Murthy and M. Mukhopadhyay, “Unification of stress intensity factor (SIF) extraction methods with an h-adaptive finite element scheme”, *Comm. Numer. Methods Engrg.* **17** (2001), 509–520.
- [Nakamura 1991] T. Nakamura, “Three-dimensional stress fields of elastic interface cracks”, *J. Appl. Mech. (ASME)* **58** (1991), 939–946.
- [Paris 2014] P. C. Paris, “A brief history of the crack tip stress intensity factor and its application”, *Meccanica (Milano)* **49** (2014), 759–764.
- [Parks 1974] D. M. Parks, “A stiffness derivative finite element technique for determination of crack tip stress intensity factors”, *Int. J. Fract.* **10** (1974), 487–502.
- [Qian et al. 2016] G. Qian, V. F. González-Albuixech, M. Niffenegger, and E. Giner, “Comparison of KI calculation methods”, *Eng. Fract. Mech.* **156** (2016), 52–67.

- [Rahul Kumar et al. 1997] P. Rahul Kumar, S. Saigal, and S. Yunus, “Singular p-version finite elements for stress intensity factor computations”, *Int. J. Numer. Methods Eng.* **40** (1997), 1091–1114.
- [Raju and Newman, Jr. 1977] I. S. Raju and J. C. Newman, Jr., “Three dimensional finite-element analysis of finite-thickness fracture specimens”, Technical Report NASA-TN-D-8414, L-10967, NASA Langley Research Center, 1977.
- [Ramamurthy et al. 1986] T. S. Ramamurthy, T. Krishnamurthy, K. B. Narayana, K. Vijayakumar, and B. Dattaguru, “Modified crack closure integral method with quarter point elements”, *Mech. Res. Commun.* **13** (1986), 179–186.
- [Ravi-Chandar 2008] K. Ravi-Chandar, *Springer handbook of experimental solid mechanics*, edited by W. N. Sharpe, Jr., Springer, New York, 2008.
- [Rice 1968] J. R. Rice, “A path independent integral and the approximate analysis of strain concentration by notches and cracks”, *J. Appl. Mech. (ASME)* **35** (1968), 379–386.
- [Rybicki and Kanninen 1977] E. F. Rybicki and M. F. Kanninen, “A finite element calculation of stress intensity factors by a modified crack closure integral”, *Eng. Fract. Mech.* **9** (1977), 931–938.
- [Sanford 1979] R. J. Sanford, “A critical re-examination of the Westergaard method for solving opening-mode crack problems”, *Mech. Res. Commun.* **6** (1979), 289–294.
- [Sethuraman and Maiti 1988] R. Sethuraman and S. K. Maiti, “Finite element based computation of strain energy release rate by modified crack closure integral”, *Eng. Fract. Mech.* **30** (1988), 227–231.
- [Shih et al. 1976] C. F. Shih, H. G. Delorenzi, and M. D. German, “Crack extension modeling with singular quadratic isoparametric elements”, *Int. J. Fract.* **12** (1976), 647–651.
- [Shih et al. 1986] C. F. Shih, B. Moran, and T. Nakamura, “Energy release rate along a three-dimensional crack front in a thermally stressed body”, *Int. J. Fract.* **30** (1986), 79–102.
- [Shivakumar et al. 1988] K. N. Shivakumar, P. W. Tan, and J. C. Newman, “A virtual crack-closure technique for calculating stress intensity factors for cracked three dimensional bodies”, *Int. J. Fract.* **36** (1988), 43–50.
- [Sih 1973] G. C. Sih, *Methods of analysis and solutions of crack problems*, Springer, Dordrecht, 1973.
- [Swamy et al. 2008] S. Swamy, M. V. Srikanth, K. S. R. K. Murthy, and P. S. Robi, “Determination of mode I stress intensity factors of complex configurations using strain gages”, *J. Mech. Mater. Struct.* **3** (2008), 1239–1255.
- [Tada et al. 2000] H. Tada, P. C. Paris, and G. R. Irwin, *The stress analysis of cracks handbook*, ASME Press, New York, 2000.
- [Tracey 1977] D. M. Tracey, “Discussion of “on the use of isoparametric finite elements in linear fracture mechanics” by R. S. Barsoum”, *Int. J. Numer. Methods Eng.* **11** (1977), 401–402.
- [Treifi et al. 2008] M. Treifi, S. O. Oyadiji, and D. K. L. Tsang, “Computations of modes I and II stress intensity factors of sharp notched plates under in-plane shear and bending loading by the fractal-like finite element method”, *Int. J. Solids Struct.* **45** (2008), 6468–6484.
- [Wilson 1969] W. K. Wilson, *Combined mode fracture mechanics*, University of Pittsburgh, California, 1969.
- [Yan et al. 2010] X. Yan, B. Liu, and Z. Hu, “SIFs of rectangular tensile sheets with symmetric double edge defects”, *J. Mech. Mater. Struct.* **5** (2010), 795–803.
- [Zhu and Smith 1995] W. Zhu and D. Smith, “On the use of displacement extrapolation to obtain crack tip singular stresses and stress intensity factors”, *Engrg. Fracture Mech.* **51**:3 (1995), 391–400.

Received 28 Jul 2017. Accepted 4 Mar 2018.

SOMAN SAJITH: s.sajith@iitg.ac.in

Department of Mechanical Engineering, Indian Institute of Technology Guwahati, Guwahati, India

KONDEPUDI S. R. K. MURTHY: ksrkm@iitg.ac.in

Department of Mechanical Engineering, Indian Institute of Technology Guwahati, Guwahati, India

PUTHUVEETIL S. ROBI: psr@iitg.ac.in

Department of Mechanical Engineering, Indian Institute of Technology Guwahati, Guwahati, India

LONGITUDINAL SHEAR BEHAVIOR OF COMPOSITES WITH UNIDIRECTIONAL PERIODIC NANOFIBERS OF SOME REGULAR POLYGONAL SHAPES

HAI-BING YANG, CHENG HUANG, CHUAN-BIN YU AND CUN-FA GAO

Based on the Gurtin–Murdoch interface model, a complex variable-based approach is presented to study the longitudinal shear behavior of composites containing unidirectional periodic nanofibers. For intuitive demonstration, numerical results of the interfacial stress concentration and the effective (longitudinal) shear moduli are calculated for composites containing circular and (approximately) regular polygonal fibers. Graphic illustrations show that the interaction among periodic nanofibers can be neglected in the prediction of the interfacial stress field when the volume fraction of the fibers is less than 7%. For reasonably given interface parameters, fiber volume fraction and fiber size, the composite containing periodic circular fibers can achieve a lowest sensitivity of effective shear moduli to the interface effect among all the aforementioned fiber shapes. Moreover, we show that if the fibers are much harder than the surrounding matrix (for example, the shear modulus of the fibers exceeds twice that of the matrix), the corresponding interface effect can make only negligible contributions to the effective longitudinal shear moduli of the composites.

1. Introduction

Based on the concept of surface stress associated with the excess free energy of a material surface, Gurtin, Murdoch and coworkers [[Gurtin and Murdoch 1975](#); [1978](#); [Gurtin et al. 1998](#)] developed a general continuum-based mechanical model, known as the Gurtin–Murdoch model, for a material surface/interface with residual tension and elasticity. In the past two decades, the Gurtin–Murdoch model has contributed greatly to the investigations of mechanical behavior of composites containing nanoparticles or nanofibers. For example, in the context of the Gurtin–Murdoch model, the stress state in the vicinity of spherical nanoparticles and circular/elliptical nanofibers embedded in a foreign matrix was studied, respectively, in [[Sharma et al. 2003](#); [Lim et al. 2006](#); [Tian and Rajapakse 2007](#); [Luo and Wang 2009](#); [Mogilevskaya et al. 2008](#); [Dai et al. 2016d](#); [2018](#)], while the effective moduli of composites with spherical nanoparticles and circular nanofibers were examined in [[Duan et al. 2005](#); [Chen et al. 2007](#); [Mogilevskaya et al. 2010](#); [Yvonnet et al. 2008](#); [Dai et al. 2016c](#); [2016b](#); [2017](#)], respectively.

Based on the Gurtin–Murdoch model, present work aims to establish an alternative numerical procedure to determine the longitudinal shear properties of composites containing periodic polygon-shaped nanofibers. The work is motivated by the fact that there are only few available methods besides the finite element method for the prediction of the elastic behavior of composites containing periodic nanofibers, and particularly is inspired by the paper [[Dai et al. 2016c](#)], involving periodic circular nanofibers. Based on the methodology in that paper, however, the extension of circular inclusions to noncircular inclusions

Keywords: Gurtin–Murdoch model, nanofiber, periodic fibers, interface effect, effective modulus.

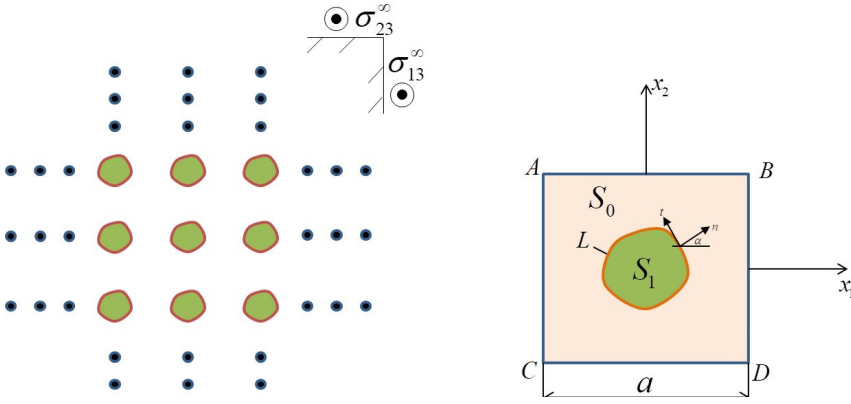


Figure 1. Left: an elastic matrix containing periodic array of nanofibers. Right: a representative square unit cell.

(e.g., polygonal inclusions) is difficult. In fact, as in [Dai et al. 2016c], it is relatively easy to extract the equations with respect to the unknown coefficients since the complex potentials of the circular inclusions are represented by the Taylor series (which is simple in form), but for polygonal inclusions it is usually difficult to do the same thing because the corresponding complex potentials can only be described by general Faber series which has a much more complicated form than the Taylor series. Consequently, it is still nontrivial to design an effective procedure with efficient numerical implementation to calculate the stress field for polygonal inclusions.

This paper is organized as follows. The boundary-value problem for composites with periodic polygon-shaped nanofibers under uniform remote longitudinal shear loadings is formulated in Section 2, and its series solution is established in Section 3. Several numerical examples are presented in Section 4 for validating our solution and illustrating the mechanical behavior of the corresponding composites. Finally, the main remarks constitute Section 5.

2. Problem description

As shown in Figure 1a, an elastic matrix (shear modulus G_0) containing a periodic array of unidirectional (approximately) polygonal nanofibers (shear modulus G_1) under uniform remote antiplane shear loadings σ_{13}^∞ and σ_{23}^∞ is considered. The influences of the nanofibers are described by the interface effect arising from the interface energies based on the Gurtin–Murdoch model [1975]. Here, to make the problem relatively tractable, we simply choose the representative unit cell (RUC), i.e., a square with the side length denoted by a (Figure 1b). For convenience, we denote the regions occupied by the matrix, the fiber and the interface between them, as S_0 , S_1 , and L , respectively. In particular, the indices (superscripts or subscripts) 0 and 1 are used to denote the physical quantities belonging to the matrix and fiber in the RUC, respectively.

According to the Gurtin–Murdoch mode, the elastic fields in the bulk region (S_0 , S_1) still satisfy the classical governing equations except for the stress discontinuity at the interfaces. In detail, the governing

equations for the out-of-plane displacement w and the antiplane shear stresses are given by

$$\frac{\partial^2 w^{(i)}}{\partial x_1^2} + \frac{\partial^2 w^{(i)}}{\partial x_2^2} = 0, \quad i = 0, 1, \quad (1)$$

$$\sigma_{13}^{(i)} = G_i \frac{\partial w^{(i)}}{\partial x_1}, \quad \sigma_{23}^{(i)} = G_i \frac{\partial w^{(i)}}{\partial x_2}, \quad i = 0, 1, \quad (2)$$

while the boundary condition on the interface are described as

$$w^{(1)} - w^{(0)} = 0, \quad \sigma_{n3}^{(1)} - \sigma_{n3}^{(0)} = G_s \frac{d^2 w^{(1)}}{ds^2} \quad \text{on } L, \quad (3)$$

where σ_{n3} is the shear traction on the interface L with n denoting the direction of outward normal to L (see [Figure 1b](#)), G_s is the interface shear modulus, and ds denotes the arc length of an element of the curve L along its tangent.

In addition to the boundary condition (3) on L , the periodic boundary condition on the edge $ABCD$ of the RUC can be expressed as [\[Xia et al. 2003\]](#)

$$\left. \begin{aligned} w^{(0)}\left(\frac{1}{2}a, x_2\right) - w^{(0)}\left(-\frac{1}{2}a, x_2\right) &= \Delta_1 \\ w^{(0)}\left(x_1, \frac{1}{2}a\right) - w^{(0)}\left(x_1, -\frac{1}{2}a\right) &= \Delta_2 \end{aligned} \right\} \quad \forall |x_1|, |x_2| \leq \frac{1}{2}a, \quad (4)$$

$$\left. \begin{aligned} (dw^{(0)}/dx_2)|_{(x_1, a/2)} &= (dw^{(0)}/dx_2)|_{(x_1, -a/2)} \\ (dw^{(0)}/dx_1)|_{(a/2, x_2)} &= (dw^{(0)}/dx_1)|_{(-a/2, x_2)} \end{aligned} \right\} \quad \forall |x_1|, |x_2| \leq \frac{1}{2}a, \quad (5)$$

where Δ_1 and Δ_2 are the constant increments between displacements on the sides DB and CA as well as AB and CD , respectively (see [Figure 1b](#)). Furthermore, these two increments can be determined by equilibrium equation on the sides AB and DB :

$$\int_A^B \sigma_{23}^{(0)}\left(x_1, \frac{1}{2}a\right) \frac{dx_1}{a} = \sigma_{23}^\infty, \quad \int_D^B \sigma_{13}^{(0)}\left(\frac{1}{2}a, x_2\right) \frac{dx_2}{a} = \sigma_{21}^\infty. \quad (6)$$

3. Solution procedure

General solutions to (1) and (2) can be given in terms of two complex potentials $f_i(z)$ ($i = 0, 1$) as [\[Muskhelishvili 1975\]](#)

$$w^{(i)} = \text{Im} f_i(z), \quad i = 0, 1, \quad (7)$$

$$\sigma_{23}^{(i)} + I\sigma_{13}^{(i)} = G_i f_i'(z), \quad i = 0, 1, \quad (8)$$

with

$$z = x_1 + Ix_2, \quad (9)$$

where the symbol I denotes the imaginary unit. In addition, the shear traction σ_{n3} on the interface L can be written as [\[Luo and Wang 2009\]](#)

$$\sigma_{23}^{(i)} = G_i \text{Im}[f_i'(t)e^{I\alpha}], \quad t \in L, \quad i = 0, 1, \quad (10)$$

where α is the angle between the normal direction n and the positive x_1 axis (see Figure 1b). Thus, by (7) and (10), the condition (3) can be rewritten in the form as

$$\begin{aligned} \operatorname{Im} f_0(t) &= \operatorname{Im} f_1(t), \\ \operatorname{Re} f_0(t) - \gamma \operatorname{Re} f_1(t) - \gamma R \operatorname{Re}[f_1'(t)e^{I\alpha}] &= 0, \quad t \in L, \end{aligned} \tag{11}$$

with

$$\gamma = \frac{G_1}{G_0}, \quad \lambda = \frac{G_s}{G_0 R}. \tag{12}$$

In particular, the second equation in (11) comes from the integration of the second equation in (3) with respect to the arc length of L .

Using (7), conditions (4) and (5) can be rewritten as

$$\operatorname{Im} f_0(z^{DB}) - \operatorname{Im} f_0(z^{CA}) = \Delta_1, \quad \operatorname{Im} f_0(z^{AB}) - \operatorname{Im} f_0(z^{CD}) = \Delta_2, \tag{13}$$

$$\operatorname{Re} f_0'(z^{AB}) - \operatorname{Re} f_0'(z^{CD}) = 0, \quad \operatorname{Im} f_0'(z^{DB}) - \operatorname{Im} f_0'(z^{CA}) = 0, \tag{14}$$

where z^{AB} , z^{CD} , z^{DB} , and z^{CA} represent the points of uniform distribution located on the sides AB , CD , DB , and CA , respectively. Furthermore, the following relations should be satisfied:

$$z^{AB} = \overline{z^{CD}}, \quad z^{DB} = -\overline{z^{CA}}. \tag{15}$$

In addition, by using (8), the condition (6) becomes

$$\begin{aligned} \int_A^B \operatorname{Re} f_0'(z) \frac{dz}{a} &= \frac{\sigma_{23}^\infty}{G_0}, \\ \int_D^B \operatorname{Im} f_0'(z) \frac{dz}{a} &= I \frac{\sigma_{13}^\infty}{G_0}. \end{aligned} \tag{16}$$

Here, we introduce a conformal mapping which transforms the boundary L in the physical z -plane into a unit circle in the imaginary ξ -plane, as [Muskhelishvili 1975]

$$z = \omega(\xi) = R \left(\xi + \sum_{n=1}^{+\infty} t_n \xi^{-n} \right), \quad |\xi| \geq 1, \tag{17}$$

where R and t_n denote the constants determined by the overall size and shape of L . Subsequently, the complex function $f_1(z)$ in S_1 can be represented approximately via the following truncated Faber series as

$$f_1(z) = \sum_{j=1}^N a_j P_{1j}(z), \tag{18}$$

where $P_{1j}(z)$ is a Faber polynomial for the region S_1 and satisfies

$$P_{1j}(z) = \xi^j(z) + \sum_{n=1}^{\infty} \beta_{j,n} \xi^{-n}(z), \tag{19}$$

on L , where

$$\beta_{1,n} = t_n, \quad \beta_{j+1,n} = t_{j+n} + \beta_{j,n+1} + \sum_{i=1}^n t_{n-1} \beta_{j,i} - \sum_{i=1}^j t_{j-1} \beta_{i,n}, \quad j, n = 1, 2, \dots \quad (20)$$

In the above formulas (18)–(20), a_j ($j = 1, \dots, N$) are the unknown complex coefficients to be determined and t_n ($n = 1, 2, \dots$) are the constant coefficients of the mapping (17). Similarly, the complex function $f_0(z)$ in S_0 can be expressed in terms of the superposition principle as follows [Dai et al. 2016a]:

$$f_0(z) = \sum_{j=1}^N b_j \xi^{-j} + \sum_{j=1}^M c_j P_j(z), \quad (21)$$

with

$$P_{j+1}(z) = P_1(z)P_j(z) - \sum_{k=1}^{j-1} m_k P_{j-k}(z) - (j+1)m_j, \quad (j = 1, \dots, M-1),$$

$$P_1(z) = \frac{143z}{84a}, \quad m_k = \begin{cases} -\frac{1}{6} & k = 3, \\ \frac{1}{56} & k = 7, \\ 0 & k = \text{others}, \end{cases} \quad (22)$$

where b_j ($j = 1, \dots, N$) and c_j ($j = 1, \dots, M$) are the unknown complex coefficients to be determined, while $P_j(z)$ ($j = 1 \dots M$) is a Faber polynomials of an (approximate) square region.

Substituting the defined complex potentials (18) and (21) into the corresponding boundary conditions (Equations (11), (13), (14) and (16)) leads to the solutions of coefficients a_j ($j = 1, \dots, N$), b_j ($j = 1, \dots, N$), and c_j ($j = 1, \dots, M$) via the Fourier expansion method. In detail, a system of linear equations with respect to the unknown coefficients a_j ($j = 1, \dots, N$), b_j ($j = 1, \dots, N$) and c_j ($j = 1, \dots, M$) can be obtained by equating the corresponding coefficients on the two sides of equations on the internal interface L . On the external boundary $ABCD$, a collocation method is used by choosing K ($K \geq M/2$) collocation points equidistantly on each side to deal with the periodic boundary conditions (13) and (14), then a system of linear equations can be extracted with respect to the unknown coefficients b_j ($j = 1, \dots, N$) and c_j ($j = 1, \dots, M$). Using the method in [Dai et al. 2016c], all the unknown coefficients can be described by the two parameters Δ_1 and Δ_2 . In terms of the two mean stress conditions (see (16)), the two parameters Δ_1 and Δ_2 can be obtained uniquely, and then the coefficients a_j ($j = 1, \dots, N$), b_j ($j = 1, \dots, N$), and c_j ($j = 1, \dots, M$) are all determined. Once the actual complex potentials $f_i(z)$ ($i = 0, 1$) are found, the displacement and stress field in the entire RUC are obtained using (7) and (8).

In addition, referring to the present Cartesian coordinate system, the effective longitudinal shear moduli (denoted by G_{1313} , G_{1323} , G_{2313} , and G_{2323}) of the composite can be defined based on the obtained stress and displacement as

$$\begin{bmatrix} G_{1313} & G_{1323} \\ G_{2313} & G_{2323} \end{bmatrix} \cdot \begin{bmatrix} \Delta_1/a \\ \Delta_2/a \end{bmatrix} = \begin{bmatrix} \sigma_{13}^\infty \\ \sigma_{23}^\infty \end{bmatrix}. \quad (23)$$

It is noteworthy that determination of all the effective shear moduli involve considering two independent kinds of external loadings (for example, $\sigma_{13}^\infty \neq 0$, $\sigma_{23}^\infty = 0$ and $\sigma_{13}^\infty = 0$, $\sigma_{23}^\infty \neq 0$) and calculating the corresponding parameters Δ_1 and Δ_2 , respectively.

4. Numerical examples

In this section, we focus on the examples for circular nanofibers and regular polygonal nanofibers, in which corresponding mappings (17) are given approximately as [Muskhelishvili 1975]

$$\omega(\xi) = R\xi \quad (\text{circle}), \quad (24)$$

$$\omega(\xi) = R\left(\xi + \frac{1}{3}\xi^{-2}\right) \quad (\text{triangle}), \quad (25)$$

$$\omega(\xi) = R\left(\xi - \frac{1}{6}\xi^{-3}\right) \quad (\text{square1}), \quad (26)$$

$$\omega(\xi) = R\left(\xi + \frac{1}{6}\xi^{-3}\right) \quad (\text{square2}), \quad (27)$$

$$\omega(\xi) = R\left(\xi + \frac{1}{10}\xi^{-4}\right) \quad (\text{pentagon}), \quad (28)$$

$$\omega(\xi) = R\left(\xi + \frac{1}{15}\xi^{-5}\right) \quad (\text{hexagon}), \quad (29)$$

where R characterizes the radius or side length of corresponding fibers. It is worth noting that the maximum volume fraction of the fibers varies with the fiber shape. In particular, when R is prescribed within the nanoscale, the normalized interface parameter λ defined in (12) is usually of the order 10^{-2} to 10^{-1} [Ruud et al. 1993; Josell et al. 1999].

4.1. Resultant stress fields around interface. Here, we define the resultant shear stresses $\sigma^{(i)}$ ($i = 0, 1$) and σ^∞ as follows:

$$\sigma^{(i)} = \sqrt{\sigma_{13}^{(i)2} + \sigma_{23}^{(i)2}}, \quad i = 1, 2, \quad (30)$$

$$\sigma^\infty = \sqrt{\sigma_{13}^{\infty 2} + \sigma_{23}^{\infty 2}}. \quad (31)$$

Figures 2 and 3 show the resultant shear stresses around the variously shaped interface between fiber volume fraction (VF) for $\sigma_{13}^\infty = \sigma_{23}^\infty$, $\lambda = 0.12$. It can be seen from Figures 2 and 3 that the results for periodic fibers converge to those for a single fiber in an infinite plane (see the corresponding results in [Wang and Schiavone 2014]) as the volume fraction of the fibers decreases, roughly speaking, to 7%. This suggests that one can use the simpler model of a single fiber in an infinite plane to predict approximately the stress concentration around periodic fibers when the fiber volume fraction falls below 7%.

4.2. Effective shear moduli. From an extensive collection of our numerical examples for fibers of various shapes (including those defined in (24)–(29)), it is found from Figures 4 and 5 that the increment Δ_1 is always zero when $\sigma_{23}^\infty = 0$ while the increment Δ_2 is always zero when $\sigma_{13}^\infty = 0$. This suggests that the shear stress σ_{13}^∞ does not induce the shear strain in the x_2 - x_3 plane while the shear stress σ_{23}^∞ does not induce the shear strain in the x_1 - x_3 plane (here x_3 denotes the coordinate axis perpendicular to the x_1 - x_2 plane). That is to say, the minor effective shear moduli G_{1323} and G_{2313} are always zero, which implies that the effective longitudinal shear properties of the composite with periodic circular or regular polygonal fibers are almost orthotropic in terms of our present reference coordinate system. All

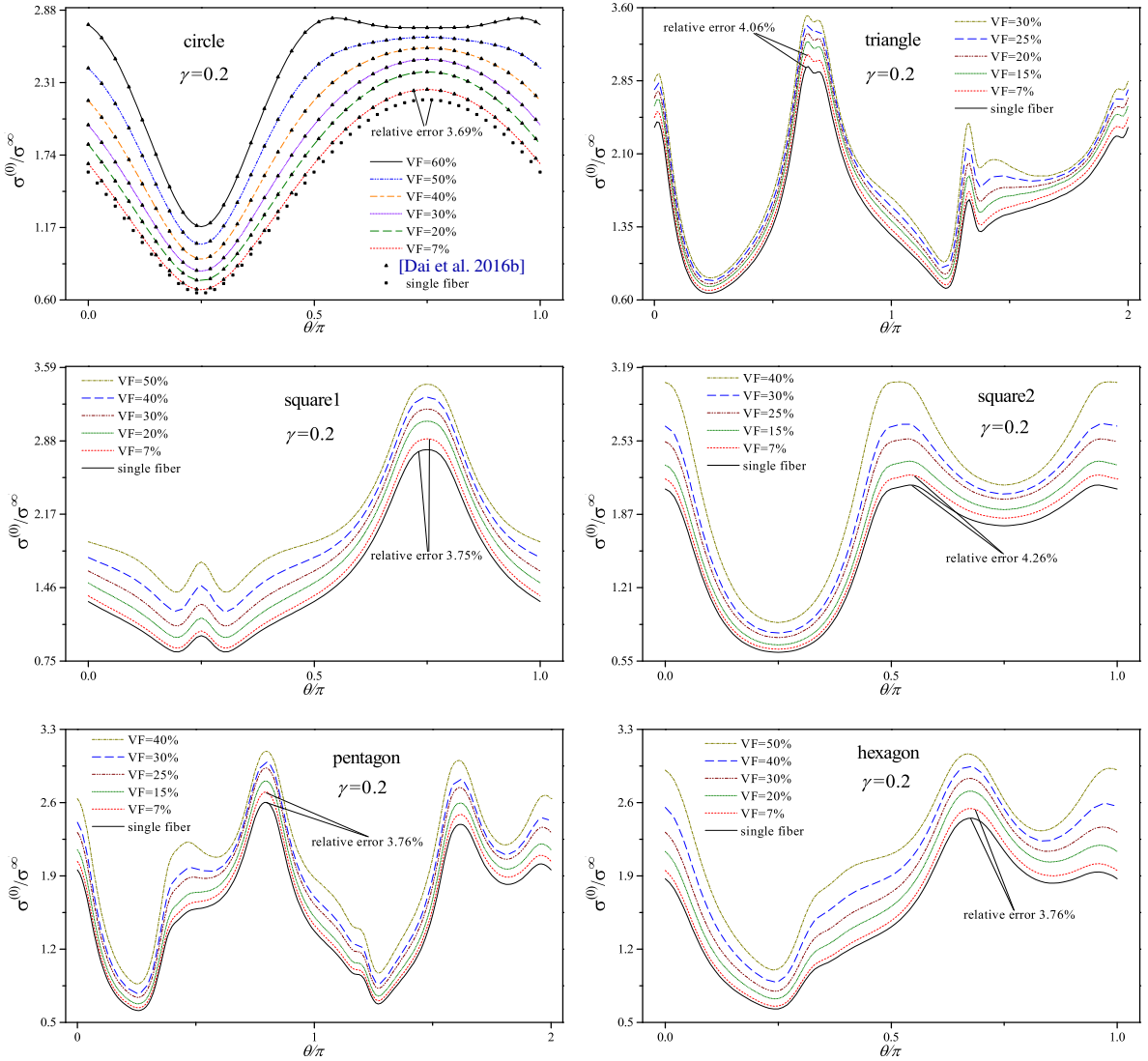


Figure 2. Resultant shear stresses around matrix on the interface between soft fiber and matrix. In each panel, the lowermost curve or dotted line shows single-fiber data from [Wang and Schiavone 2014]; remaining curves are reference data from [Dai et al. 2016c].

things considered, the zero values of these coupled shear moduli may be due to the perpendicularity in the direction of period.

In the remaining examples, one of the purposes is to study the influence of the shear modulus of the nanofibers on the effective longitudinal shear properties of the composite. To do this, however, requires that the interface shear modulus G_s not be treated as a fixed parameter when the shear modulus of the nanofibers changes since the interface shear modulus depends on not only the bulk properties of the matrix but also those of the nanofibers. Here, we treat the interface as the assembly of the surfaces of the matrix and nanofibers so that the interface shear modulus G_s is defined as the sum of the surface shear

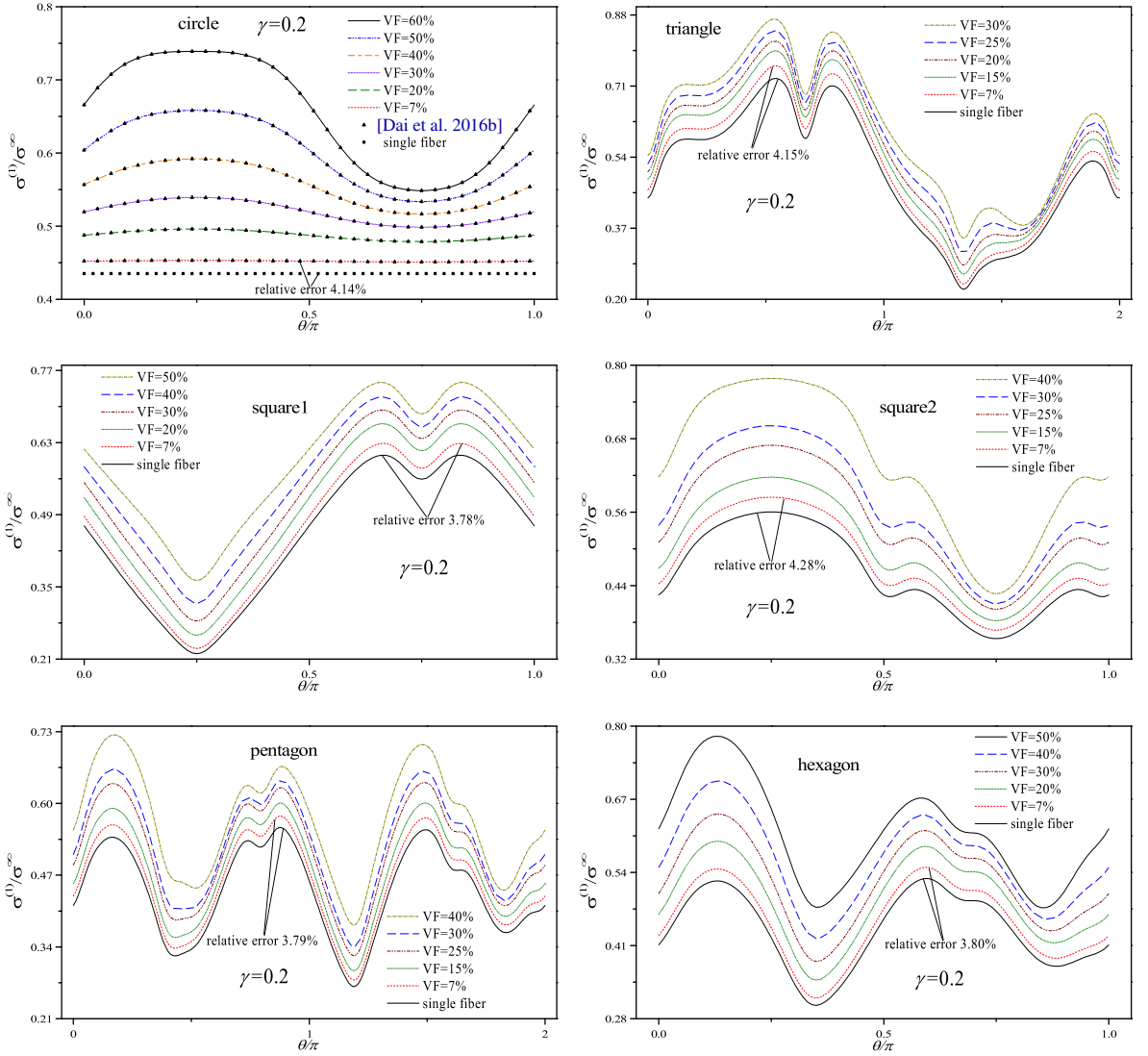


Figure 3. Resultant shear stresses around fiber on the interface between soft fiber and matrix. See caption on previous page for key.

moduli of the matrix and nanofibers [Tiersten 1969; Zhang et al. 2012]:

$$G_s = G_{s0} + G_{s1}, \quad (32)$$

where G_{s0} and G_{s1} are the surface moduli of the matrix and fibers, respectively. In particular, we simply assume $G_{s1}/G_{s0} = G_1/G_0$ since larger bulk moduli often indicate larger surface moduli. Consequently, the normalized interface parameter λ introduced from (12) is rewritten as

$$\lambda = \frac{G_{s0}(1 + \gamma)}{G_0 R} = \lambda_0(1 + \gamma), \quad \lambda_0 = \frac{G_{s0}}{G_0 R}, \quad (33)$$

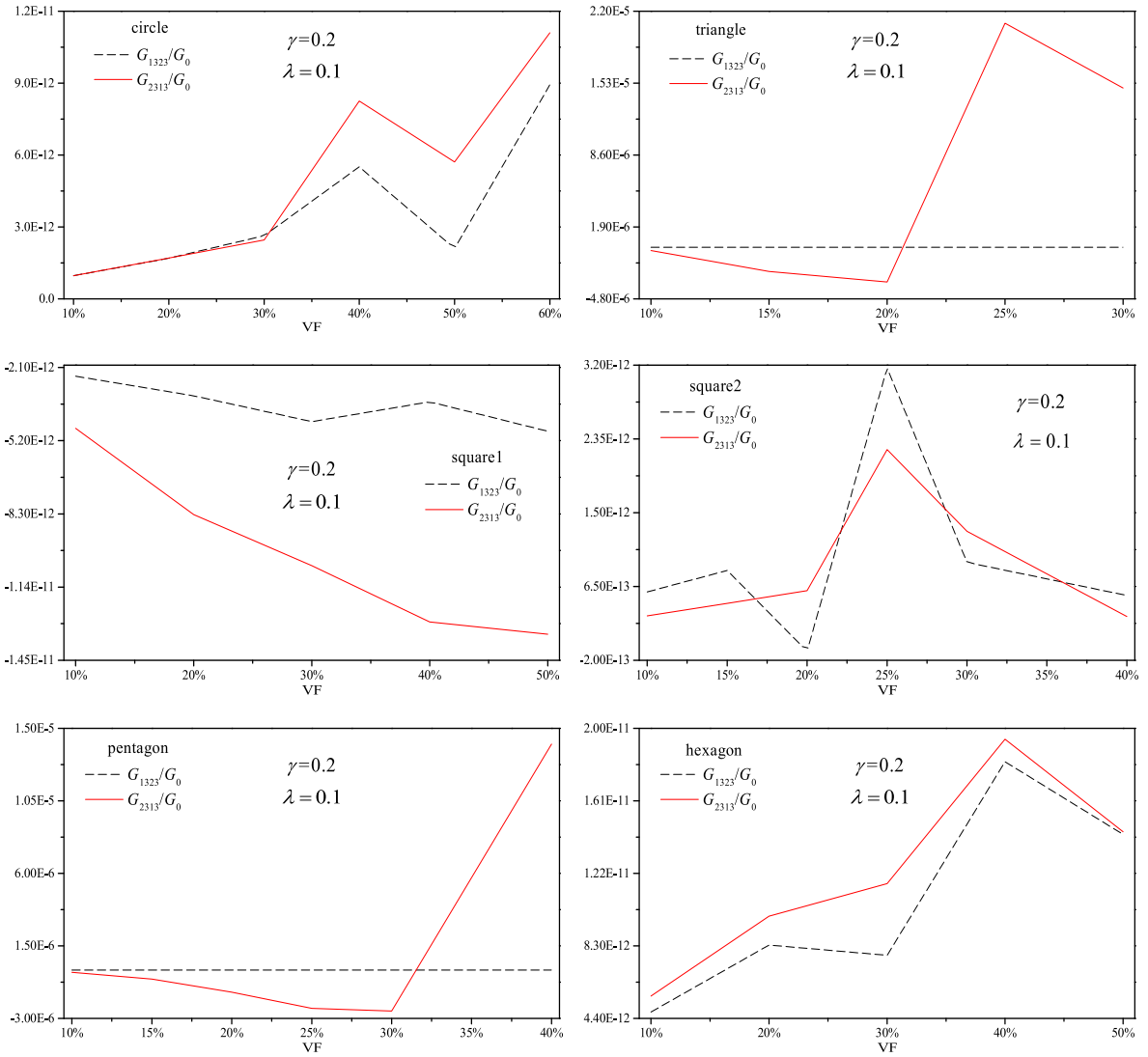


Figure 4. Minor effective longitudinal shear moduli of the composite with periodic soft fibers.

where λ_0 characterizes the normalized surface shear modulus of the matrix and it is taken as 0.1 in all of the following examples.

Figures 6–13 show the influence of the shape and volume fraction (VF) of the periodic fibers on the major effective (longitudinal) shear moduli G_{1313} and G_{2323} of the corresponding composite for several different interface parameters λ . In particular, G_{1313}^* and G_{2323}^* denote the specific major effective shear moduli of the composite when the interface effect is absent (or equivalently the interface parameter $\lambda = 0$). In Figures 7, 9, 11, and 13, we rearrange the results given respectively in Figures 6, 8, 10, and 12, and use the ratios G_{1313}/G_{1313}^* and G_{2323}/G_{2323}^* to demonstrate directly the contribution of interface effect to the major effective shear moduli of the composite with varying volume fraction of fibers.

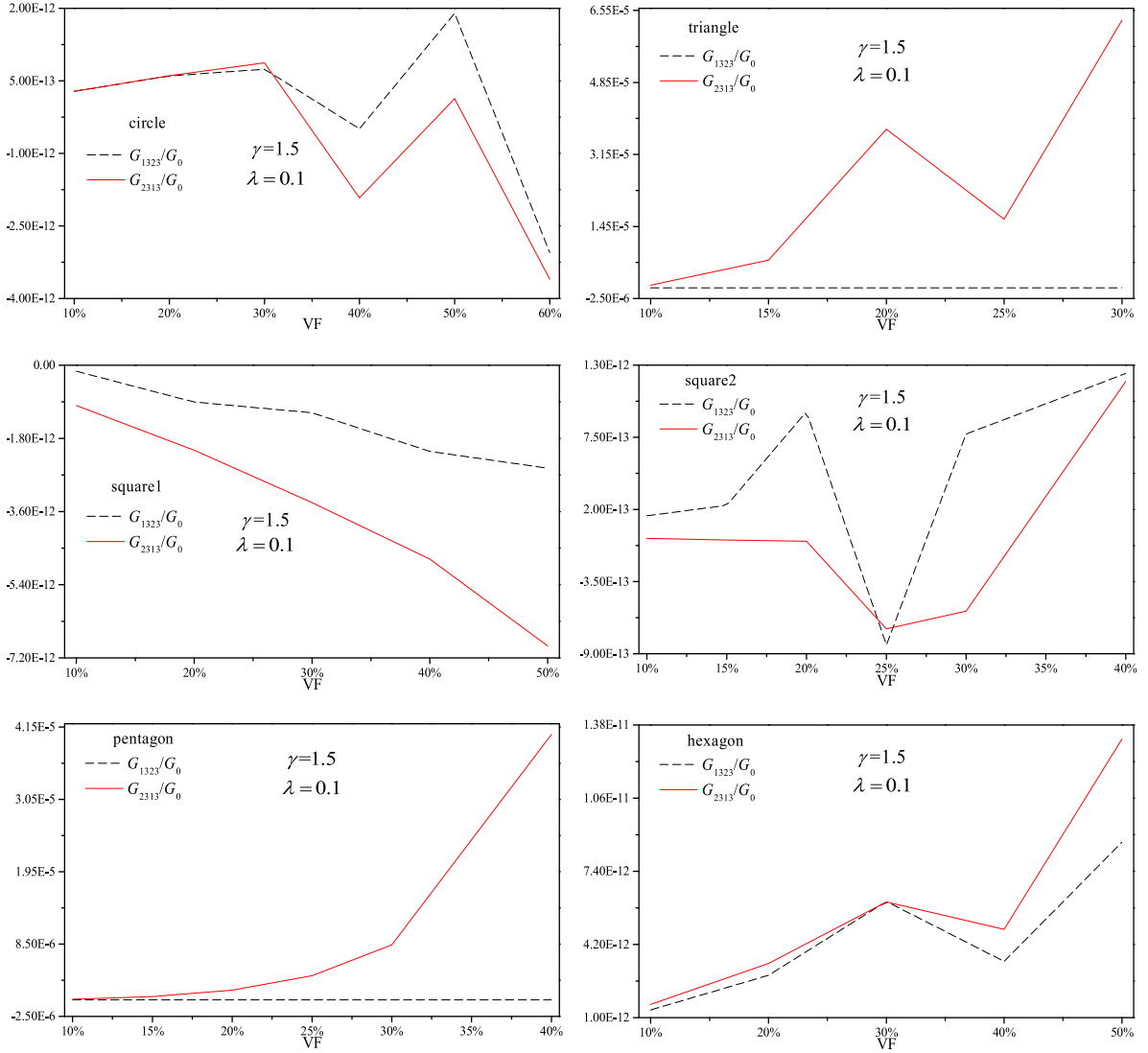


Figure 5. Minor effective longitudinal shear moduli of the composite with periodic hard fibers.

It is easily seen from Figures 6–13 that for a given fiber volume fraction, the major effective shear moduli of the composite containing periodic regular n -sided polygonal fibers decrease from the original increase with increasing n for the nonnegative value of λ when the fibers get harder. For the negative value of λ , the major effective shear moduli of the composite increase with increasing n . On the other hand, the contribution of the interface effect to the major effective shear moduli of this kind of composite decreases always with increasing n . These imply that for a given fiber volume fraction and interface parameter λ , the major effective shear moduli of the composite containing periodic circular fibers are larger but less sensitive to the interface effect as compared with those of the composites containing periodic regular polygonal fibers when the fibers are very soft. When the fibers get harder, the major effective shear moduli of the

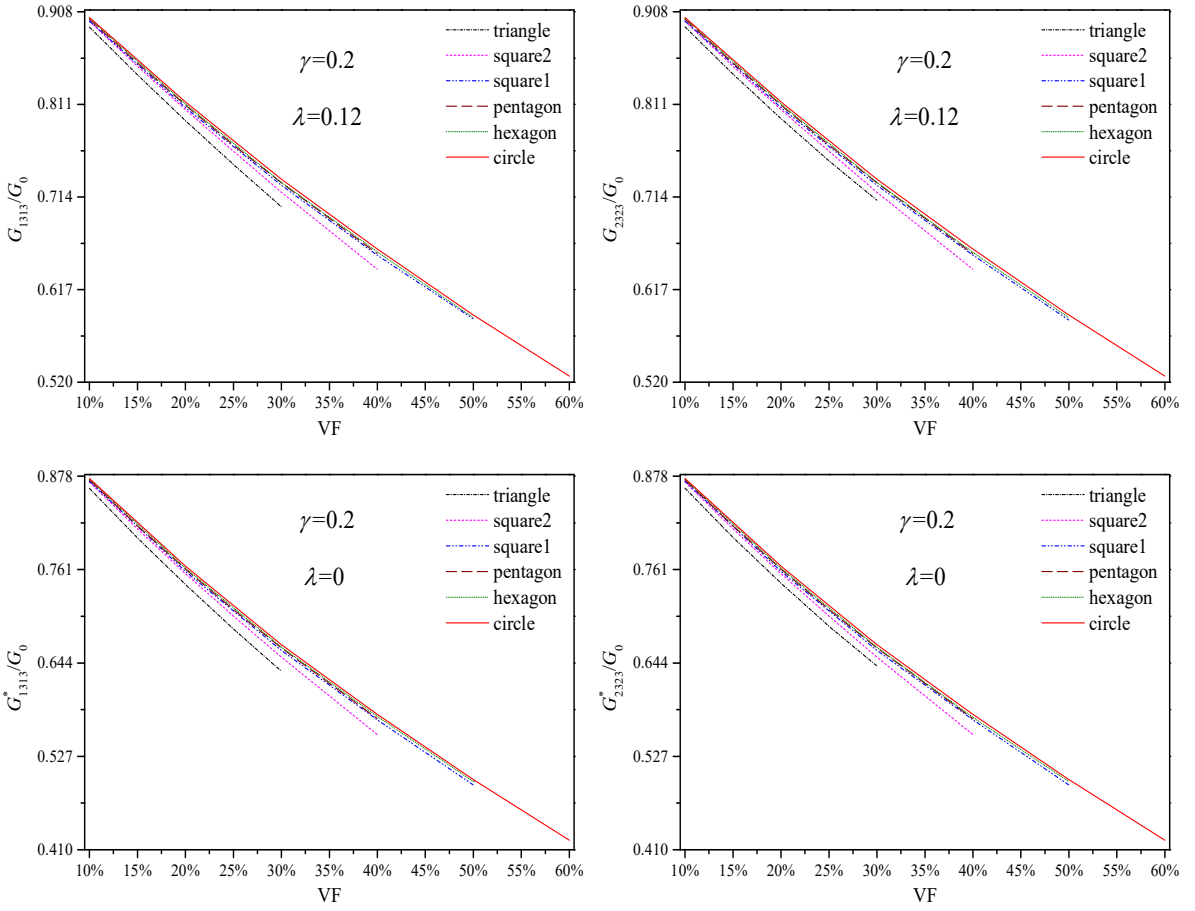


Figure 6. Major effective longitudinal shear moduli of the composite containing periodic soft fibers.

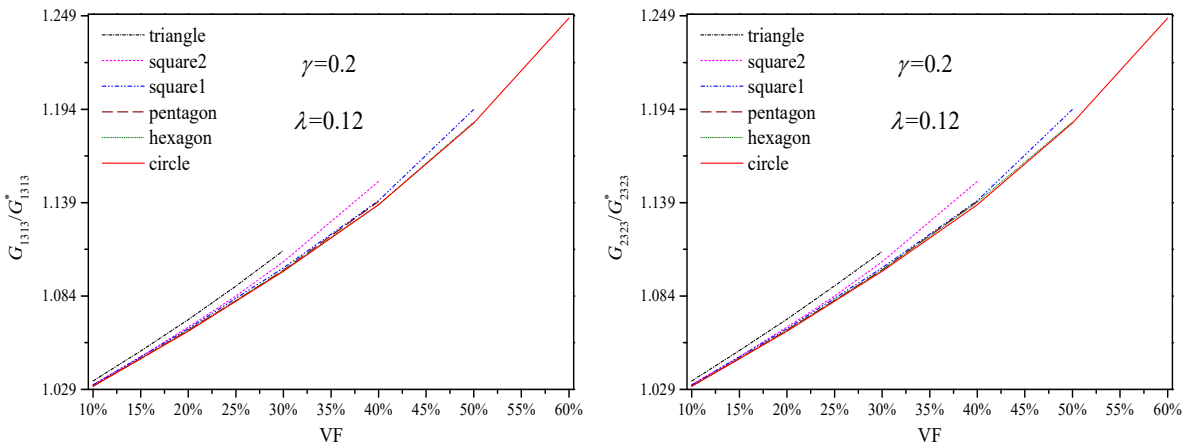


Figure 7. Contribution of interface effect to the major effective longitudinal shear moduli.

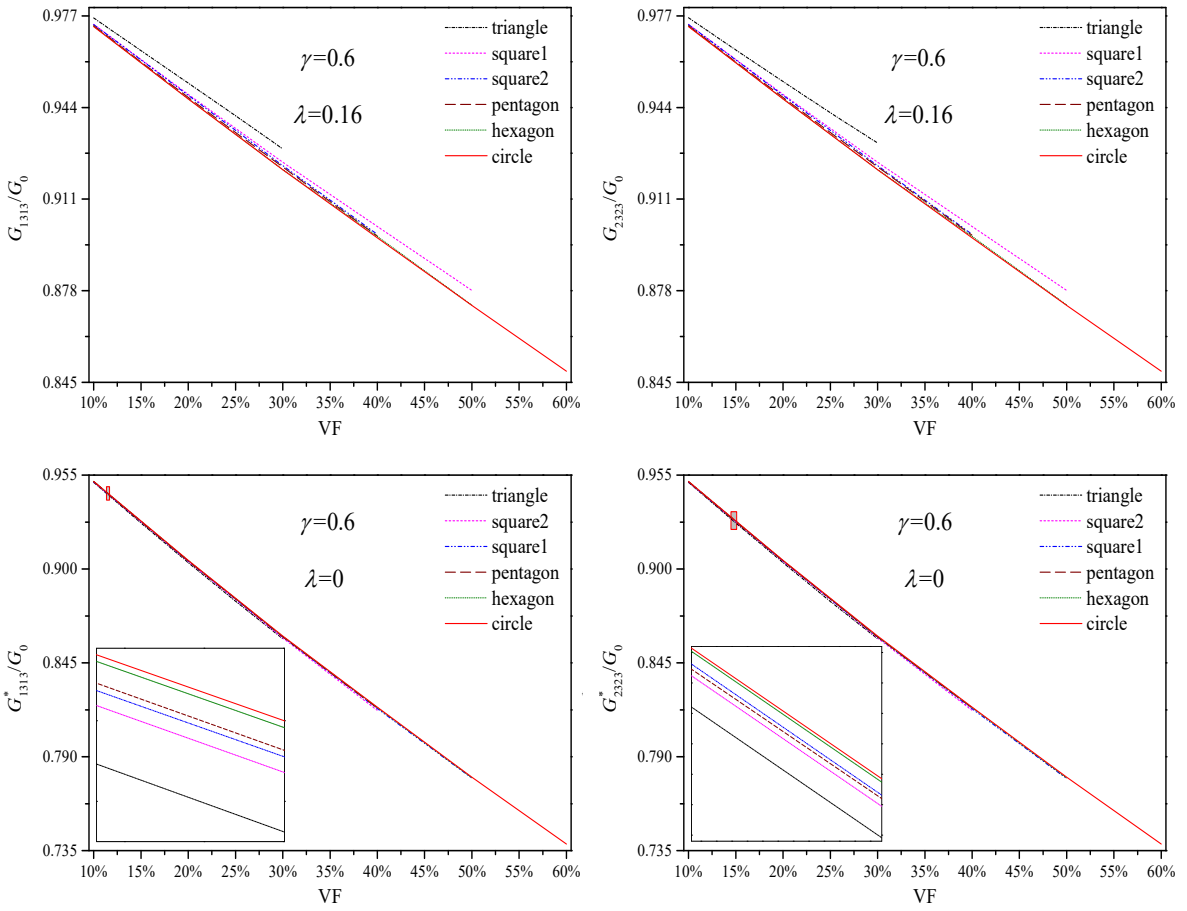


Figure 8. Major effective longitudinal shear moduli of the composite containing periodic soft fibers.

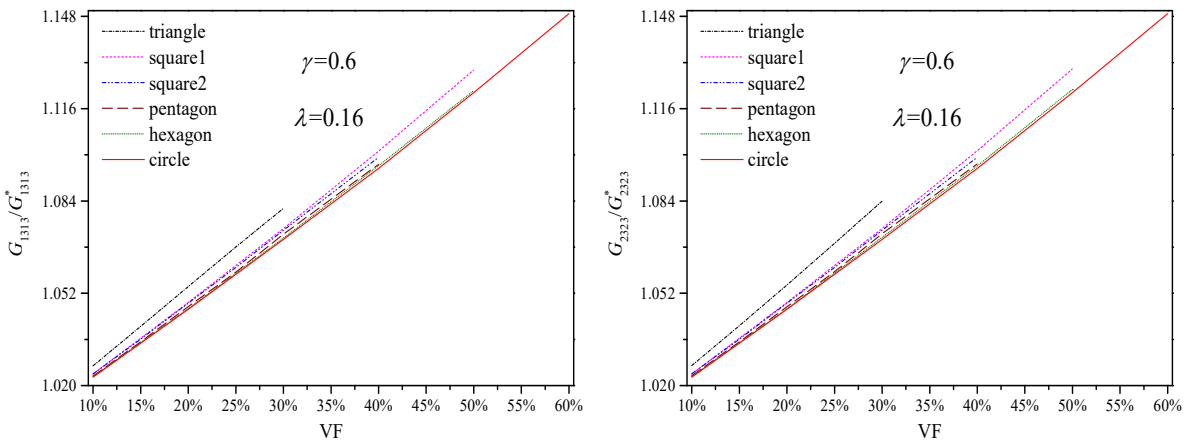


Figure 9. Contribution of interface effect to the major effective longitudinal shear moduli.

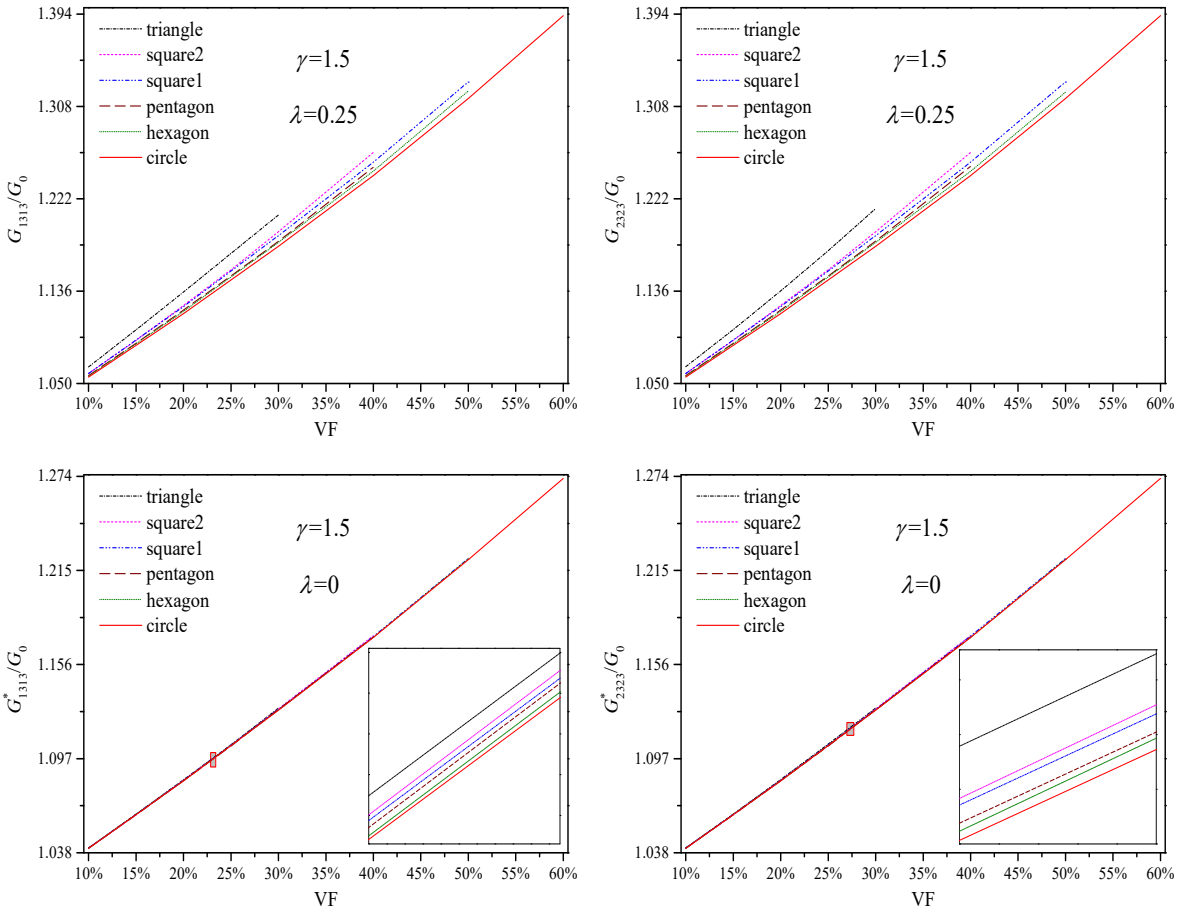


Figure 10. Major effective longitudinal shear moduli of the composite containing periodic hard fibers.

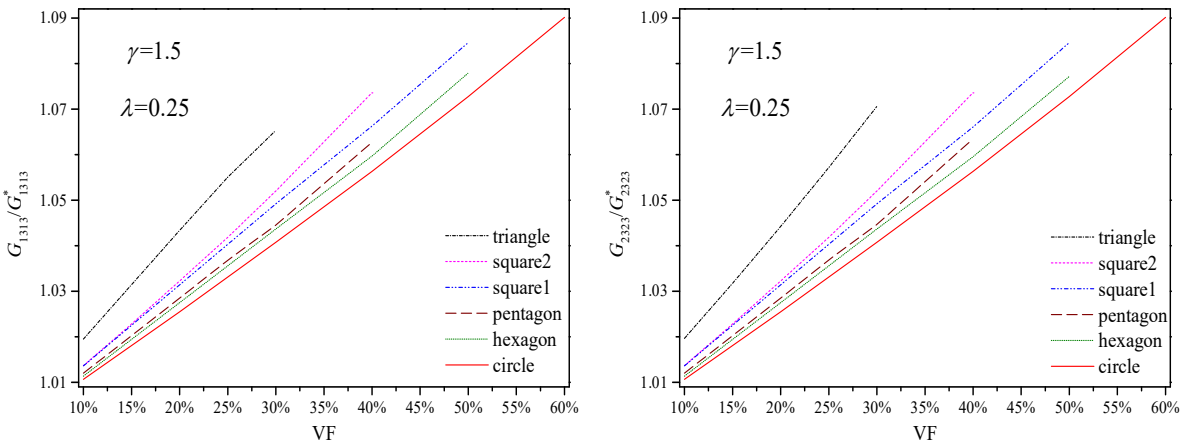


Figure 11. Contribution of interface effect to the major effective longitudinal shear moduli.

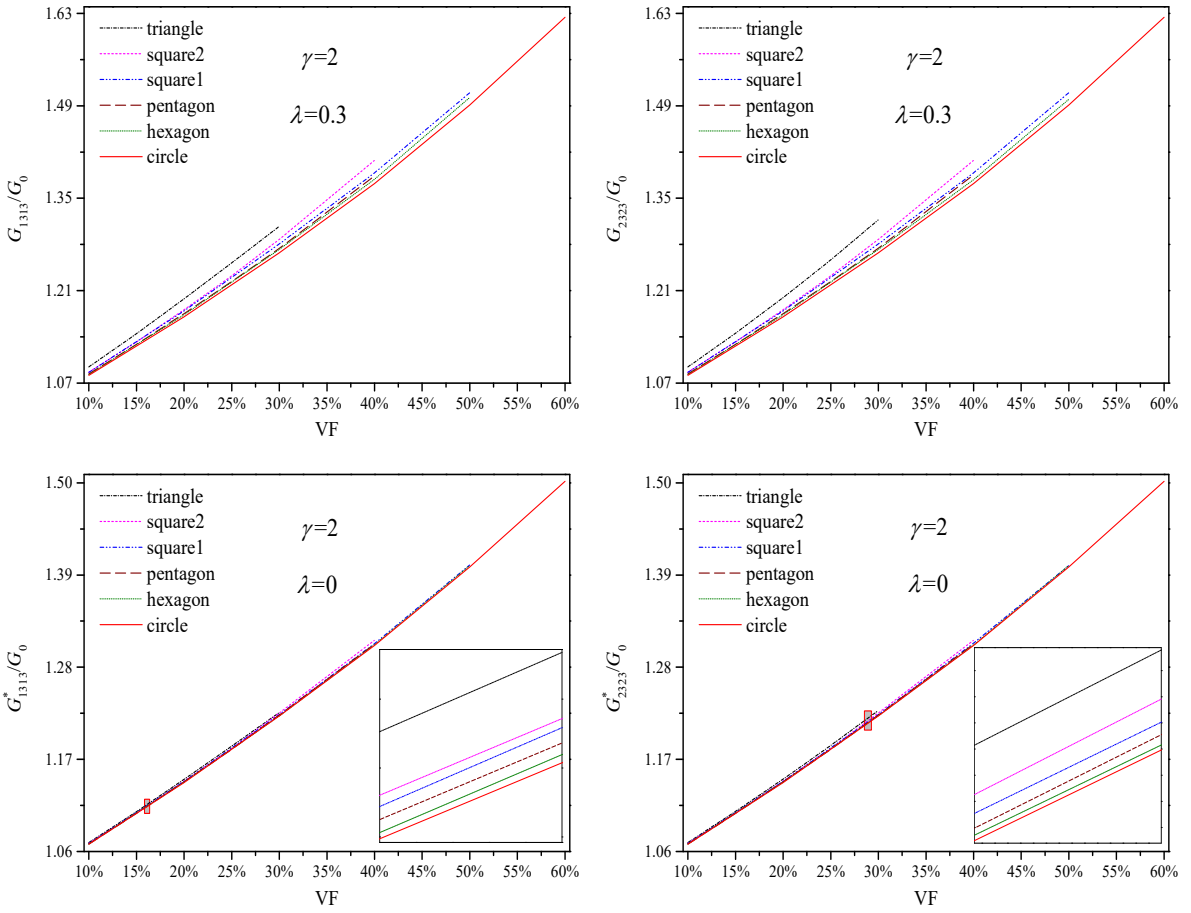


Figure 12. Major effective longitudinal shear moduli of the composite containing periodic hard fibers.

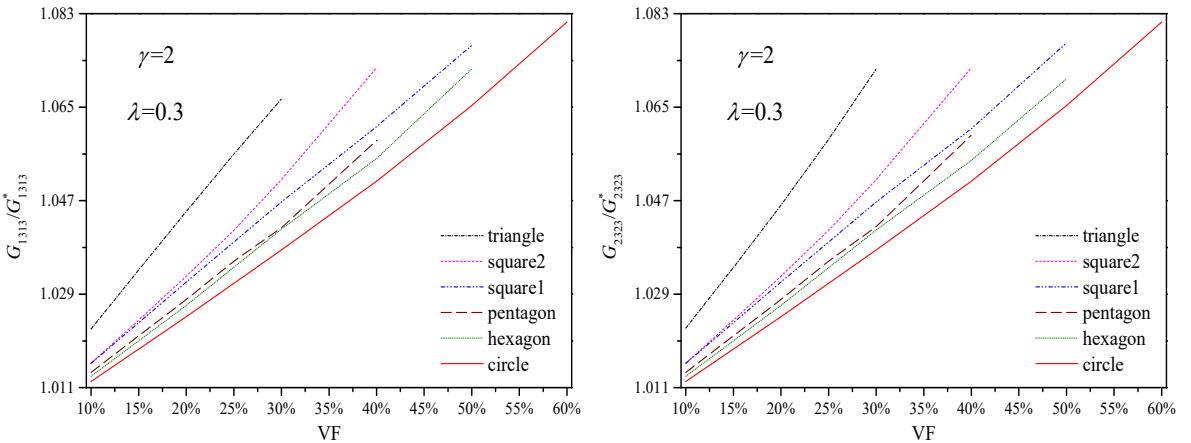


Figure 13. Contribution of interface effect to the major effective longitudinal shear moduli.

composite containing periodic circular fibers are still less sensitive to the interface effect but are smaller as compared with those of the composites containing periodic regular polygonal fibers. In addition, our results indicate that one can neglect the interface effect (i.e., treat the interfaces as being perfectly bonded to the matrix) when the shear modulus of the fibers reaches two (or more) times that of the matrix.

5. Conclusion

Based on the Gurtin–Murdoch model, the longitudinal shear behavior of composites with unidirectional periodic nanofibers of approximately regular polygonal shapes is investigated using a complex variable-based numerical procedure. Numerical results are presented for the stress concentration on the interfaces and the effective (longitudinal) shear moduli of the composite relative to the interface parameter, the volume fraction of the fibers, and the hardness of the fibers. The main findings are as follows:

- (1) The stress field around periodic fibers can be treated as that around a single fiber (of identical shape, size, and interface parameters) without inducing significant errors when the volume fraction of the periodic fibers is less than 7%.
- (2) For (reasonably) given interface parameters, fiber volume fraction and fiber size, the composite containing periodic circular fibers has the lowest sensitivity of effective shear moduli to the interface effect among all the composites containing periodic regular polygonal fibers.
- (3) The interface effect is negligible in the determination of the effective shear moduli of the composite when the shear modulus of the fibers reaches two (or more) times that of the matrix.

Acknowledgements

This project is supported by the National Natural Science Foundation of China (11472130 and 11232007) and a Project Funded by the Priority Academic Program Development of Jiangsu Higher Education Institutions (PAPD).

References

- [Chen et al. 2007] T. Chen, G. J. Dvorak, and C. C. Yu, “Size-dependent elastic properties of unidirectional nano-composites with interface stresses”, *Acta Mech.* **188** (2007), 39–54.
- [Dai et al. 2016a] M. Dai, L. C. Meng, C. Huang, and C. F. Gao, “Electro-elastic fields around two arbitrarily-shaped holes in a finite electrostrictive solid”, *Appl. Math. Model.* **40**:7-8 (2016), 4625–4639.
- [Dai et al. 2016b] M. Dai, P. Schiavone, and C. F. Gao, “Determination of effective thermal expansion coefficients of unidirectional fibrous nanocomposites”, *Zeitschrift für angewandte Mathematik und Physik* **67**:5 (2016), 110.
- [Dai et al. 2016c] M. Dai, P. Schiavone, and C. F. Gao, “Prediction of the stress field and effective shear modulus of composites containing periodic inclusions incorporating interface effects in anti-plane shear”, *J. Elasticity* **125**:2 (2016), 217–230.
- [Dai et al. 2016d] M. Dai, P. Schiavone, and C. F. Gao, “Uniqueness of neutral elastic circular nano-inhomogeneities in antiplane shear and plane deformations”, *J. Appl. Mech. (ASME)* **83**:10 (2016), 101001.
- [Dai et al. 2017] M. Dai, P. Schiavone, and C. F. Gao, “A new method for the evaluation of the effective properties of composites containing unidirectional periodic nanofibers”, *Arch. Appl. Mech.* **87**:4 (2017), 647–665.
- [Dai et al. 2018] M. Dai, A. Gharahi, and P. Schiavone, “Analytic solution for a circular nano-inhomogeneity with interface stretching and bending resistance in plane strain deformations”, *Appl. Math. Model.* **55** (2018), 160–170.
- [Duan et al. 2005] H. L. Duan, J. Wang, Z. P. Huang, and B. L. Karihaloo, “Size-dependent effective elastic constants of solids containing nano-inhomogeneities with interface stress”, *J. Mech. Phys. Solids* **53** (2005), 1574–1596.

- [Gurtin and Murdoch 1975] M. E. Gurtin and A. I. Murdoch, “A continuum theory of elastic material surfaces”, *Arch. Ration. Mech. Anal.* **57**:4 (1975), 291–323.
- [Gurtin and Murdoch 1978] M. E. Gurtin and A. I. Murdoch, “Surface stress in solids”, *Int. J. Solids Struct.* **14**:6 (1978), 431–440.
- [Gurtin et al. 1998] M. E. Gurtin, J. Weissmüller, and F. Larche, “A general theory of curved deformable interfaces in solids at equilibrium”, *Philos. Mag. A* **78**:5 (1998), 1093–1109.
- [Josell et al. 1999] D. Josell, J. E. Bonevich, I. Shao, and R. C. Cammarata, “Measuring the interface stress: silver/nickel interfaces”, *J. Mater. Res.* **14**:11 (1999), 4358–4365.
- [Lim et al. 2006] C. W. Lim, Z. R. Li, and L. H. He, “Size dependent, non-uniform elastic field inside a nano-scale spherical inclusion due to interface stress”, *Int. J. Solids Struct.* **43**:17 (2006), 5055–5065.
- [Luo and Wang 2009] J. Luo and X. Wang, “On the anti-plane shear of an elliptic nano inhomogeneity”, *Eur. J. Mech. A Solids* **28**:5 (2009), 926–934.
- [Mogilevskaya et al. 2008] S. G. Mogilevskaya, S. L. Crouch, and H. K. Stolarski, “Multiple interacting circular nano-inhomogeneities with surface/interface effects”, *J. Mech. Phys. Solids* **56** (2008), 2298–2327.
- [Mogilevskaya et al. 2010] S. G. Mogilevskaya, S. L. Crouch, H. K. Stolarski, and A. Benusioglio, “Equivalent inhomogeneity method for evaluating the effective elastic properties of unidirectional multi-phase composites with surface/interface effects”, *Int. J. Solids Struct.* **47**:3-4 (2010), 407–418.
- [Muskhelishvili 1975] N. I. Muskhelishvili, *Some basic problems of the mathematical theory of elasticity*, Noordhoff, Groningen, The Netherlands, 1975.
- [Ruud et al. 1993] J. A. Ruud, A. Witvrouw, and F. Spaepen, “Bulk and interface stresses in silver-nickel multilayered thin films”, *J. Appl. Phys.* **74**:4 (1993), 2517–2523.
- [Sharma et al. 2003] P. Sharma, S. Ganti, and N. Bhate, “Effect of surfaces on the size-dependent elastic state of nano-inhomogeneities”, *Appl. Phys. Lett.* **82**:4 (2003), 535–537.
- [Tian and Rajapakse 2007] L. Tian and R. Rajapakse, “Elastic field of an isotropic matrix with a nanoscale elliptical inhomogeneity”, *Int. J. Solids Struct.* **44**:24 (2007), 7988–8005.
- [Tiersten 1969] H. F. Tiersten, “Elastic surface waves guided by thin films”, *J. Appl. Phys.* **40** (1969), 770–789.
- [Wang and Schiavone 2014] X. Wang and P. Schiavone, “Interaction of a screw dislocation with a nano-sized, arbitrarily shaped inhomogeneity with interface stresses under anti-plane deformations”, *Proc. Royal Soc. A* **470**:2170 (2014), art. id. 20140313.
- [Xia et al. 2003] Z. H. Xia, Y. F. Zhang, and F. Ellyin, “A unified periodical boundary conditions for representative volume elements of composites and applications”, *Int. J. Solids Struct.* **40**:8 (2003), 1907–1921.
- [Yvonnet et al. 2008] J. Yvonnet, H. L. Quang, and Q. C. He, “An XFEM/level set approach to modelling surface/interface effects and to computing the size-dependent effective properties of nanocomposites”, *Comput. Mech.* **42** (2008), 119–131.
- [Zhang et al. 2012] C. Zhang, W. Chen, and C. Zhang, “On propagation of anti-plane shear waves in piezoelectric plates with surface effect”, *Phys. Lett. A* **376** (2012), 3281–3286.

Received 11 Sep 2017. Revised 23 Jan 2018. Accepted 14 Feb 2018.

HAI-BING YANG: yanghb@scut.edu.cn

Department of Mechanics Engineering, School of Civil Engineering and Transportation, South China University of Technology, Guangzhou, China

CHENG HUANG: hc_12345@nuaa.edu.cn

State Key Laboratory of Mechanics and Control of Mechanical Structures, Nanjing University of Aeronautics and Astronautics, Nanjing, China

CHUAN-BIN YU: cbyu@nuaa.edu.cn

State Key Laboratory of Mechanics and Control of Mechanical Structures, Nanjing University of Aeronautics and Astronautics, Nanjing, China

CUN-FA GAO: cfgao@nuaa.edu.cn

State Key Laboratory of Mechanics and Control of Mechanical Structures, Nanjing University of Aeronautics and Astronautics, Nanjing, China

FRACTURE INITIATION IN A TRANSVERSELY ISOTROPIC SOLID: TRANSIENT THREE DIMENSIONAL ANALYSIS

LOUIS M. BROCK

A transversely isotropic solid is at rest, and contains a semi-infinite, plane crack. The axis of rotational material symmetry lies in the crack plane. Application of normal point forces to each face of the crack causes transient 3D growth. The related problem of discontinuities in displacement and traction that exist on regions that exhibit dynamic similarity is first considered. Analytic results are obtained in integral transform space. These lead to equations of the Wiener–Hopf type for the fracture problem. Analytic solutions are again obtained and, upon inversion, subjected to a dynamic energy release rate criterion that includes kinetic energy. A particular form of rapid growth in time of the forces is found to cause crack growth rates that indeed vary with position, but not with time. The influence of anisotropy upon wave speeds and crack edge contour are examined.

1. Introduction

Fracture initiation caused by mixed-mode, point-force loading at the edge of a semi-infinite plane crack is considered in [Brock 2017a; 2017b]. Analysis in each case is 3D and transient. The crack exists in an unbounded, isotropic, and isothermal solid in [Brock 2017b], while the solid is thermoelastic and initially at uniform (absolute) temperature in [Brock 2017a]. The dynamic energy release rate criterion [Freund 1972; 1990] is imposed, but with kinetic energy taken into account [Gdoutos 2005]. In [Brock 2017b] it is found that a particular time history for the loading can generate a crack edge contour that is dynamically similar; i.e., its shape is time-invariant. The same result is found in [Brock 2017a] for the fracture initiation phase. In both studies, inclusion of kinetic energy enhances the (constant) rate at which the crack expands into the material. In both studies the expanding contour is semicircular only when shearing forces are absent.

This study concerns the effect of anisotropy on the fracture process. The solid is isothermal, so that the time history considered in [Brock 2017a; 2017b] again predicts a dynamically similar crack contour. However, the solution results will be considered in the context of a (perhaps brief) fracture initiation phase. Moreover, to emphasize the effects of transverse isotropy, only normal point force loading is considered. In this regard, when the axis of material rotational symmetry is perpendicular to a plane:

- (1) Plane strain problems are governed by the two elastic constants associated with the plane, i.e., are effectively isotropic [Scott and Miklowitz 1967].
- (2) Some results for 3D problems are independent of direction in the plane [Brock 2013].

Keywords: transverse isotropy, transient, fracture initiation, kinetic energy, crack contour.

Here therefore the material rotational symmetry axis lies in the crack plane. Moreover, the initial crack edge is not aligned with a principal axis in the plane. The solution process follows closely that employed for [Brock 2017a; 2017b]. Process steps are clearly identified, but resulting formulas are generally confined to those unique to the problem considered here.

2. Problem statement

Consider an unbounded, transversely isotropic solid with principal axes defined by fixed Cartesian basis $\mathbf{x}_0 = \mathbf{x}_0(x_k^0)$, $k = (1, 2, 3)$. A closed crack $A_C(x_3^0, \xi_1^0 < 0)$ with boundary $C(\xi_1^0, x_3^0) = 0$ is at rest for time $t \leq 0$, where

$$\begin{bmatrix} \xi_1^0 \\ \xi_2^0 \end{bmatrix} = \begin{bmatrix} \cos \theta & \sin \theta \\ -\sin \theta & \cos \theta \end{bmatrix} \begin{bmatrix} x_1^0 \\ x_2^0 \end{bmatrix} \quad (|\theta| < \pi/2). \quad (1)$$

It is noted that the axis of material rotational symmetry is parallel to the x_2^0 -axis. For $t > 0$ compressive point forces appear on both crack faces at $(x_1^0 = 0-, x_2^0 = 0, x_3^0 = 0\pm)$. Brittle fracture is instantaneous, and the crack extends outward from $\mathbf{x}_0 = 0$ in the positive ξ_1^0 -direction. The crack now occupies region $A_C + \delta A$ and boundary C includes a concave bulge:

$$\sqrt{(x_1^0)^2 + (x_2^0)^2} = l(\theta, \psi, t), \quad l(\theta, \psi, t) = V(\theta, \psi)t, \quad (2a)$$

$$0 < V < V_R, \quad \psi = \tan^{-1} \frac{\xi_2^0}{\xi_1^0} \quad (|\psi| < \pi/2). \quad (2b)$$

Introduction of an orientation angle ψ with respect to coordinates (ξ_1^0, ξ_2^0) proves useful in the derivation of solutions. Equation (2) implies a dynamically similar process, and requires that (speed parameter) V is subsonic and below the Rayleigh value V_R . Displacement $\mathbf{u}(u_k)$ and traction $\mathbf{T}(\sigma_{ik})$ are field variables. If body forces are neglected [Payton 1983; Jones 1999],

$$\nabla \cdot \mathbf{T} - \rho D^2 \mathbf{u} = 0, \quad (3a)$$

$$\begin{bmatrix} \sigma_{11} \\ \sigma_{22} \\ \sigma_{33} \end{bmatrix} = \begin{bmatrix} C_{11} & C_{12} & C_{13} \\ C_{12} & C_{22} & C_{12} \\ C_{13} & C_{12} & C_{33} \end{bmatrix} \begin{bmatrix} \partial_1 u_1 \\ \partial_2 u_2 \\ \partial_3 u_3 \end{bmatrix}, \quad (3b)$$

$$\sigma_{2k} = C_{44}(\partial_2 u_k + \partial_k u_2), \quad k = (1, 3), \quad \sigma_{31} = C_{55}(\partial_3 u_1 + \partial_1 u_3). \quad (3c)$$

Components (u_k, σ_{ik}) are functions of (\mathbf{x}_0, t) , $\partial_k f = \partial f / \partial x_k$ and $(\nabla, \nabla^2, \mathbf{1})$ respectively are gradient and Laplacian operators and identity tensor. Here (Df, \dot{f}) signify time differentiation in basis \mathbf{x}_0 and (C_{ik}, ρ) are the elastic constants and mass density, and $C_{13} = C_{11} - 2C_{55}$. Here reference quantities are shear modulus and shear wave speed:

$$\mu = C_{44}, \quad V_4 = \sqrt{C_{44}/\rho}. \quad (4a)$$

These quantities give dimensionless parameters

$$c = \frac{V}{V_4}, \quad d_1 = \frac{C_{11}}{C_{44}}, \quad d_2 = \frac{C_{22}}{C_{44}}, \quad d_5 = \frac{C_{55}}{C_{44}}, \quad d_{12} = \frac{C_{12}}{C_{44}}, \quad d_{13} = \frac{C_{13}}{C_{44}} = d_1 - 2d_5. \quad (4b)$$

For $x_3^0 = 0\pm$, $(x_1^0, x_2^0) \in A_C + \delta A$ ($t > 0$),

$$\sigma_{31} = \sigma_{32} = 0, \quad \sigma_{33} = -P\delta(x_1^0)\delta(x_2^0). \quad (5a)$$

For $x_3^0 = 0$, $(x_1^0, x_2^0) \notin A_C + \delta A$ ($t > 0$),

$$[u_k] = 0. \quad (5b)$$

In (5) force P is a positive constant, $\delta(f)$ denotes Dirac function, and $[f] = f^{(+)} - f^{(-)}$, where $f^{(\pm)} = f(\xi_1^0, \xi_2^0, 0\pm, t)$. In addition $[u_k]$ must vanish continuously on C , but σ_{3k} may exhibit (integrable) singular behavior on C . For $t \leq 0$, $(\mathbf{u}, \mathbf{T}) \equiv 0$, and for finite $t > 0$, (\mathbf{u}, \mathbf{T}) must be bounded as $|\mathbf{x}_0| \rightarrow \infty$.

3. Discontinuity problem

A common practice for solving crack problems is to represent the relative motion of crack faces as unknown discontinuities in displacement; see, e.g., [Barber 1992]. To implement that procedure, the related problem of discontinuities in (u_k, σ_{3k}) is now considered: The unbounded solid is again at rest when for time $t > 0$ the discontinuities are imposed in the same region $A_C + \delta A$ of the $x_1^0 x_2^0$ -plane. In place of (5) we have for $x_3^0 = 0$, $(x_1^0, x_2^0) \in A_C + \delta A$ ($t > 0$)

$$[u_k] = \Delta_k, \quad [\sigma_{3k}] = \Sigma_k. \quad (6a)$$

For $x_3^0 = 0$, $(x_1^0, x_2^0) \notin A_C + \delta A$ ($t > 0$),

$$[u_k] = [\sigma_{3k}] = 0. \quad (6b)$$

Here (Δ_k, Σ_k) are continuous functions of (x_1^0, x_2^0, t) . They vanish on C and for $t \leq 0$ are bounded in $A_C + \delta A$ for $\sqrt{(x_1^0)^2 + (x_2^0)^2} \rightarrow 0$. Therefore, as in the crack problem, $(\mathbf{u}, \mathbf{T}) \equiv 0$ for $t \leq 0$, and are bounded as $|\mathbf{x}| \rightarrow \infty$ for finite $t > 0$.

4. Transform solution

An effective procedure (see, e.g., [Brock and Achenbach 1973]) for 2D transient study of semi-infinite crack extension at constant speed employs:

- (1) Coordinates that translate with the crack edge.
- (2) Unilateral temporal and bilateral spatial integral transform [Sneddon 1972].

In view of (1) a translating basis \mathbf{x} is defined for $|\psi| < \pi/2$ as

$$\xi_1 = \xi_1^0 - [c(\theta, \psi) \cos \psi]s, \quad \xi_2 = \xi_2^0 - [c(\theta, \psi) \sin \psi]s, \quad x_3 = x_3^0, \quad (7a)$$

$$s = V_4 t, \quad c(\theta, \psi) = \frac{V(\theta, \psi)}{V_4}, \quad (7b)$$

$$Df = \dot{f} = V_4[\partial - c(\psi)(\partial_1 f \cos \psi + \partial_2 f \sin \psi)], \quad (7c)$$

$$\partial = \frac{\partial f}{\partial s}, \quad \partial_k f = \frac{\partial f}{\partial x_k^0}, \quad k = (1, 2). \quad (7d)$$

The temporal Laplace transform operation is

$$L(f) = \hat{f} = \int f(s) \exp(-ps) ds. \quad (8)$$

Integration is over positive real s and $\text{Re}(p) > 0$. A double spatial integral transform and inversion, respectively, can be defined [Sneddon 1972] by

$$\tilde{f}(p, q_1, q_2) = \iint \hat{f}(p, x_1, x_2) \exp[-p(q_1x_1 + q_2x_2)] dx_1 dx_2, \quad (9a)$$

$$\hat{f}(p, x_1, x_2) = \left(\frac{p}{2\pi i}\right)^2 \iint \tilde{f}(p, q_1, q_2) \exp[p(q_1x_1 + q_2x_2)] dq_1 dq_2. \quad (9b)$$

In light of (1) and (7a),

$$x_1 = x_1^0 - [c(\theta, \psi) \cos \chi]s, \quad x_2 = x_2^0 - [c(\theta, \psi) \cos \chi]s, \quad \chi = \theta + \psi. \quad (9c)$$

Integration in (9a) is over (x_1, x_2) ; integration in (9b) is along the imaginary (q_1, q_2) -axes. It is noted that (\mathbf{x}, s) have dimensions of length, p has dimensions of inverse length, and (q_1, q_2) are dimensionless. Because (1) involves a speed that varies with direction, application of (8) and (9a) to (3), (4), and (6) is complicated. Despite use of (θ, ψ) the discontinuity problem is not axially symmetric. However, 3D studies of sliding and rolling contact [Brock 2012] and crack growth [Brock 2017a; 2017b] suggest transformations

$$\text{Im}(q_1) = \text{Im}(q) \cos \chi, \quad \text{Im}(q_2) = \text{Im}(q) \cos \chi, \quad (10a)$$

$$x_1 = \xi \cos \chi, \quad x_2 = \xi \sin \chi, \quad \xi = \sqrt{x_1^2 + x_2^2} = \sqrt{\xi_1^2 + \xi_2^2}. \quad (10b)$$

Here $\text{Re}(q) = 0+$, $|\text{Im}(q)|, |\xi| < \infty$, $|\psi| < \pi/2$, and parameters (ξ, χ) and (q, χ) resemble quasipolar coordinates, i.e.,

$$dx_1 dx_2 = |\xi| d\xi d\chi, \quad dq_1 dq_2 = |q| dq d\chi. \quad (10c)$$

In particular the portion of crack contour C that bounds newly created crack surface δA can be defined as $(\xi = 0, |\psi| < \pi/2)$. The uncoupling effect of (10) leads to the combination

$$\tilde{f}(p, q_1, q_2) \rightarrow \bar{f}(p, q, \chi), \quad (11a)$$

$$\hat{f}(p, \xi, \chi) = -\frac{p^2}{2\pi} \int \frac{|q|}{q} \bar{f}(p, q, \chi) \exp(pq\xi) dq. \quad (11b)$$

Integration is along the positive ($\text{Re}(q) = 0+$) side of the $\text{Im}(q)$ -axis.

In view of (8)–(11) and (11a), Equations (3), (4), and (6) give a corresponding set in transform space by making formal substitutions

$$\nabla \rightarrow (pq \cos \chi, pq \sin \chi, \partial_3), \quad D \rightarrow \frac{p}{V_4} \beta, \quad \nabla^2 \rightarrow \partial_3^2 + p^2 q^2, \quad (12a)$$

$$\beta = 1 - cq. \quad (12b)$$

Set elements that correspond to (3a) are homogeneous, ordinary differential equations in x_3 , with characteristic functions $pA_5(q)$ and $pA_{\pm}(q)$:

$$A_5(q) = \frac{1}{\sqrt{d_5}} \sqrt{\beta^2 - q^2 c_5^2}, \quad c_5 = \sqrt{d_5 \cos^2 \chi + \sin^2 \chi}, \quad (13)$$

$$A_{\pm}(q) = \sqrt{-1/(4d_1) (\Omega_{\pm} \pm \Omega_{\mp})^2 - q^2 \cos^2 \chi}, \quad (14a)$$

$$\Omega_{\pm} = \sqrt{(\sqrt{d_1 C_2} \pm \sqrt{C_0})^2 - m^2 q^2 \sin^2 \chi}, \quad (14b)$$

$$C_0 = q^2 \sin^2 \chi - \beta^2, \quad C_2 = d_2 q^2 \sin^2 \chi - \beta^2, \quad m = 1 + d_{12}. \quad (14c)$$

It is noted that (14a) and (14b) yield the convenient result

$$d_1 (A_-^2 - A_+^2) = \Omega_+ \Omega_-. \quad (14d)$$

The branch point parameter c_5 for A_5 is a dimensionless shear wave speed. Similarly A_{\pm} respectively are associated with dimensionless wave speeds c_{\pm} :

$$c_{\pm} = \frac{1}{2} (C_{\pm} \pm C_{\mp}), \quad (15a)$$

$$C_{\pm} = \sqrt{1 + d_1 \cos^2 \chi + d_2 \sin^2 \chi \pm 2\sqrt{d_1 \cos^4 \chi + d_2 \sin^4 \chi + \Gamma \sin^2 \chi \cos^2 \chi}}, \quad (15b)$$

$$\Gamma = 1 + d_1 d_2 - m^2. \quad (15c)$$

It is noted that

$$A_+ A_- = \frac{1}{\sqrt{d_1}} \sqrt{\beta^2 - q^2 c_+^2} \sqrt{\beta^2 - q^2 c_-^2}. \quad (15d)$$

In [Payton 1983] parameter combinations (m, Γ) are used to characterize transversely isotropic materials; the characterization scheme is summarized in Appendix A. Results in what follows are often general. However, some key expressions and associated calculations will be illustrated in terms of the Category 1 material. In light of (13)–(15), the corresponding equations give displacement transform $\bar{\mathbf{u}} = \bar{\mathbf{u}}_5 + \bar{\mathbf{u}}_+ + \bar{\mathbf{u}}_-$ where components are

$$\begin{bmatrix} (\bar{\mathbf{u}}_5)_1 \\ (\bar{\mathbf{u}}_5)_2 \\ (\bar{\mathbf{u}}_5)_3 \end{bmatrix} = \begin{bmatrix} (\pm)A_5 \\ 0 \\ q \cos \chi \end{bmatrix} U_5^{(\pm)} \exp(-pA_5|x_3|), \quad (16a)$$

$$\begin{bmatrix} (\bar{\mathbf{u}}_{\pm})_1 \\ (\bar{\mathbf{u}}_{\pm})_2 \\ (\bar{\mathbf{u}}_{\pm})_3 \end{bmatrix} = \begin{bmatrix} (\mp)m^2 q \sin \chi \cos \chi \\ (\pm)Q_{\pm} \\ m q A_{\pm} \sin \chi \end{bmatrix} U_{\pm}^{(\pm)} \exp(-pA_{\pm}|x_3|), \quad (16b)$$

$$Q_{\pm} = C_0 - \frac{1}{4} (\Omega_+ \pm \Omega_-)^2, \quad Q_+ Q_- = C_0 m^2 q^2 \sin^2 \chi. \quad (16c)$$

Function ($U_{\pm}^{(\pm)}, U_5^{(\pm)}$) depends on (p, q, χ), and (\pm) signifies $x_3 > 0$ (+), $x_3 < 0$ (-). In view of (13) and (15) solution behavior is governed by the body wave speeds ($V_4, V_5 = c_5 V_4, V_{\pm} = c_{\pm} V_4$), where $V_- < V_+$. Bounded behavior for \hat{u}_k as $|x_3| \rightarrow \infty$ requires, in light of (16), that $\text{Re}(A_{\pm}) > 0$ and $\text{Re}(A_5) > 0$ in the

q -plane with, respectively, branch cuts

$$\text{Im}(q) = 0, \quad \frac{-1}{c_{\pm} - c} < \text{Re}(q) < \frac{1}{c_{\pm} + c}, \tag{17a}$$

$$\text{Im}(q) = 0, \quad \frac{-1}{c_5 - c} < \text{Re}(q) < \frac{1}{c_5 + c}. \tag{17b}$$

It is noted that (17) is valid only so long as $c < (1, c_5)$, i.e., $V(\theta, \psi) < (V_4, V_5)$.

Expressions for $(U_{\pm}^{(\pm)}, U_5^{(\pm)})$ in terms of $(\bar{\Delta}_k, \bar{\Sigma}_k)$ are obtained by combining (16) with the transforms of (3b), (3c), and (6a). Details are found in Appendix B.

5. Application to fracture problem: equations for solution

Equation (16) represents the transform solution for the fracture problem if transforms of (5) are satisfied. Equation (5) does not involve Σ_k so $\bar{\Sigma}_k$ can be dropped. Use of (7)–(12) and (B.3)–(B.5) and the transform of (3b), (3c), and (5) give three equations:

$$\bar{\sigma}_{31}^C = \frac{\mu p}{2A_5} (S_1 \bar{\Delta}_1 + S_{12} \bar{\Delta}_2), \quad \bar{\sigma}_{32}^C = \frac{\mu p}{2A_5} (s_{12} \bar{\Delta}_1 + S_2 \bar{\Delta}_2), \tag{18a}$$

$$\bar{\sigma}_{33}^C - \frac{P}{p\beta} = \frac{\mu p}{2} A_5 S_3 \bar{\Delta}_3. \tag{18b}$$

Expressions for $(\bar{\sigma}_{31}^C, \bar{\sigma}_{32}^C)$ in (18a) can be combined to give, in addition,

$$q^2 \sin \psi \cos \psi \bar{\sigma}_{31}^C - Q_5 \bar{\sigma}_{32}^C = \mu p (T_1 \bar{\Delta}_1 + T_2 \bar{\Delta}_2). \tag{18c}$$

Here, σ_{3k}^C is the traction generated ahead of crack ($\xi > 0, c_+s - \xi - cs > 0$). Therefore, $\bar{\sigma}_{3k}^C$ exists for $\text{Re}(q) > -1/(c_+ - c)$. The second term in (18b) is transform of the Dirac function term in (5a), and therefore exists for $\text{Re}(q) < 1/c$. Function Δ_k occurs for $\xi < 0$ in a region generated behind wave front $c_+s + \xi + cs > 0$, so that $\bar{\Delta}_k$ exists for $\text{Re}(q) < 1/(c_+ + c)$. Coefficients Q_5 and $(S_1, S_{12}, S_2, S_3, T_1, T_2)$ are defined in (B.1d) and Appendix C respectively.

6. Wiener–Hopf equation

The two equations in (18a) involve four unknowns $(\bar{\sigma}_{31}^C, \bar{\sigma}_{32}^C, \bar{\Delta}_1, \bar{\Delta}_2)$. In light of Appendix C and remarks above, it is noted that pairs $(\bar{\sigma}_{31}^C, \bar{\sigma}_{32}^C)$ and $(\bar{\Delta}_1, \bar{\Delta}_2)$ have overlapping regions of analyticity in the complex q -plane, but coefficients (S_1, S_{12}, S_2) do not. Nevertheless the two equations are homogeneous, which implies that

$$\sigma_{3k}^C = \Delta_k = 0, \quad k = (1, 2). \tag{19}$$

Nonhomogeneous (18b) involves only two unknowns $(\bar{\sigma}_{33}^C, \bar{\Delta}_3)$ with overlapping regions of analyticity. We therefore examine coefficients (A_5, S_3) defined by (13) and (C.2) respectively. It is noted that

$$S_3 \approx q^2 R(c) \quad (|q| \rightarrow \infty), \tag{20a}$$

$$S_3(q_R^{\pm}) = 0, \quad q_R^{\pm} = \frac{\pm 1}{c_R \pm c}. \tag{20b}$$

For a Category 1 material such that $c_R < c_5 < c_-$, $R(c)$ is defined by

$$R(c) = \frac{1}{\sin^2 \chi - c^2} \left[4d_5^2 \cos^2 \chi + \frac{q_5^2}{\omega_+ \omega_- a_5} \left(\frac{q_-}{a_+} - \frac{q_+}{a_-} \right) \right] + \frac{\sin^2 \chi}{\omega_+ \omega_- a_5} \left[\frac{1}{a_+} (q_+ - 2mq_5) - \frac{1}{a_-} (q_+ - 2mq_5) \right], \quad (21a)$$

$$a_5(c) = \frac{1}{\sqrt{d_5}} \sqrt{c_5^2 - c^2}, \quad a_{\pm}(c) = \sqrt{\cos^2 \chi - D_{\mp}^2/d_1}, \quad D_{\pm} = \frac{1}{2}(\omega_+ \pm \omega_-), \quad (21b)$$

$$q_5(c) = d_5 \cos^2 \chi + c_5^2 - c^2, \quad q_{\pm}(c) = \sin^2 \chi - c^2 + D_{\mp}^2, \quad (21c)$$

$$\omega_{\pm}(c) = \sqrt{(1 + d_1)c^2 - \Gamma \sin^2 \chi \pm 2\sqrt{d_1}(d_2 \sin^2 \chi - c^2)(\sin^2 \chi - c^2)}. \quad (21d)$$

In (18b), $c_R = c_R(\theta, \psi)$ is the positive-real root of $R(c)$, where $0 < c_R < c_5$, $|\psi| < \pi/2$, i.e., $V_R = V_R(\theta, \psi) = c_R(\theta, \psi)V_4$ is the Rayleigh speed, and (S_3, R) are Rayleigh functions for transverse isotropy. Subcritical crack extension therefore requires that $0 < V < V^* = c^*V_4$ ($0 < c < c^*$), where $c^* = \min(1, c_5, c_R)$. It is also noted that $R \leq 0$ ($0 < c < c_R$), and in view of (20) and (21), one can define function

$$G_3 = \frac{-S_3(c_R^2 - c^2)}{R(c)[1 + q(c_R - c)][1 - q(c_R + c)]}, \quad G_3 \rightarrow 1(|q| \rightarrow \infty). \quad (22)$$

It has no roots and is analytic in the q -plane with branch cuts

$$\text{Im}(q) = 0, \quad \frac{-1}{c_5 - c} < \text{Re}(q) < \frac{-1}{c_+ - c},$$

$$\text{Im}(q) = 0, \quad \frac{1}{c_+ + c} < \text{Re}(q) < \frac{1}{c_5 + c}.$$

Function G_3 can therefore be written as product $G_3^+ G_3^-$, where G_3^{\pm} respectively are analytic in overlapping half-planes $\text{Re}(q) > -1/(c_+ - c)$ and $\text{Re}(q) < 1/(c_+ + c)$. These functions are given in Appendix D. In (16b) one can write $A_5 = A_5^+ A_5^-$, where

$$A_5^+ = \frac{1}{d_5^{1/4}} \sqrt{1 + q(c_5 - c)}, \quad A_5^- = \frac{1}{d_5^{1/4}} \sqrt{1 - q(c_5 + c)}. \quad (23)$$

Equation (23) indicates that A_5^{\pm} respectively are analytic in overlapping half-planes $\text{Re}(q) > -1/(c_5 - c)$ and $\text{Re}(q) < 1/(c_5 + c)$. In view of Appendix D, Equation (23) and the region of analyticity noted for $(\bar{\sigma}_{33}^C, \bar{\Delta}_3)$ and the second term in (18b), Equation (18b) itself can be put in the form of a Wiener-Hopf equation [Morse and Feshbach 1953]:

$$\frac{\bar{\sigma}_{33}^C}{\mu p} \frac{1}{A_5^+ G_3^+} \frac{c_R - c}{1 + q(c_R - c)} - \frac{P}{\mu p^2 \beta} \left[\frac{1}{A_5^+ G_3^+} \frac{c_R - c}{1 + q(c_R - c)} - \frac{d_5^{1/4} \sqrt{c}}{g_3^+ \sqrt{c_5}} \left(1 - \frac{c}{c_R} \right) \right] = -\frac{\bar{\Delta}_3}{2} \frac{R(c) A_5^- G_3^-}{c_R + c} [1 - q(c_R + c)] + \frac{P}{\mu p^2 \beta} \frac{d_5^{1/4} \sqrt{c}}{g_3^+ \sqrt{c_5}} \left(1 - \frac{c}{c_R} \right), \quad (24a)$$

$$g_3^+ = G_3^+ \left(\frac{1}{c} \right). \quad (24b)$$

The left-hand and right-hand sides of (24a) are analytic in respectively the overlapping half-planes $\text{Re}(q) > -1/(c_+ - c)$ and $\text{Re}(q) < 1/(c_+ + c)$ so that each side is an analytic continuation of the same entire function. In connection with (6) Δ_3 must vanish continuously on C for $x \rightarrow 0$. Equation (11a) therefore requires that $p q \bar{\Delta}_k$, and also the right-hand side of (24a), vanish for $|q| \rightarrow \infty$. The entire function itself must then in light of Liouville's theorem [Morse and Feshbach 1953] vanish, and (24a) leads to

$$\bar{\Delta}_3 = \frac{2d_5^{1/4}}{\mu p^2 \beta g_3^+ R(c)} \sqrt{\frac{c}{c_5}} \left(1 - \frac{c}{c_R}\right) \frac{1}{A_5^- G_3^-} \frac{c_R + c}{1 - q(c_R + c)}, \quad (25a)$$

$$\bar{\sigma}_{33}^C = \frac{P}{p\beta} - \frac{P}{p\beta} \frac{d_5^{1/4}}{g_3^+ c_R} \sqrt{\frac{c}{c_5}} G_3^+ A_5^+ [1 + q(c_R - c)]. \quad (25b)$$

Examination of the fracture problem solution requires knowledge of $(\bar{\sigma}_{33}^C, \bar{\Delta}_3)$ for $x \rightarrow 0^-$ and $x \rightarrow 0^+$, respectively. In view of (7)–(9),

$$\dot{f} = V_4 \left(\partial - c \frac{\partial}{\partial \xi} \right) f. \quad (26)$$

Expressions for transforms $(\bar{\sigma}_{33}^C, p\beta \bar{\Delta}_3)$ that are valid for $|q| \rightarrow \infty$ suffice in this regard:

$$p\beta \bar{\Delta}_3 \approx \frac{2P}{\mu p} \frac{\sqrt{d_5 c}}{g_3^+ R(c) \sqrt{c_5} \sqrt{c_5 + c}} \left(1 - \frac{c}{c_R}\right) \frac{1}{\sqrt{-q}}, \quad (27a)$$

$$\bar{\sigma}_{33}^C \approx \frac{P}{p} \frac{1}{g_3^+ \sqrt{c}} \sqrt{1 - \frac{c}{c_5}} \left(1 - \frac{c}{c_5}\right) \frac{1}{\sqrt{q}}. \quad (27b)$$

7. Transform inversions valid on crack plane near C

For $1/\sqrt{-q}$ and $1/\sqrt{q}$, respectively, inverse operation (10b) yields

$$-\frac{p^2}{\pi \sqrt{-\xi}} \int_+ \frac{du}{\sqrt{u}} \exp(-pu) \quad (\xi < 0), \quad (28a)$$

$$-\frac{p^2}{\pi \sqrt{\xi}} \int_+ \frac{du}{\sqrt{u}} \exp(-pu) \quad (\xi > 0). \quad (28b)$$

The “+” signifies integration over the entire positive real u -axis. In view of (28), Equation (27) involves $p \exp(-pu)$, and its inverse is recognized as $\partial \delta(s - u)$ [Abramowitz and Stegun 1972]. The point force represents a step-function in time, so for generality we now consider the more general case

$$P = P(V_4 t), \quad P(0) = 0. \quad (29)$$

Clarity of solution is enhanced if points in the crack plane are located with respect to fixed point x_0 . Therefore the inverses of (27) are, by convolution, written as functions of (ξ_0, χ, s) , where $\xi_0 = \xi + cs$, and for $(s > 0, \xi_0 \rightarrow cs +, |\psi| < \pi/2)$:

$$\bar{\Delta}_3 \approx \frac{-2V_4}{\mu \pi \sqrt{cs - \xi_0}} \frac{\sqrt{d_5 c}}{g_3^+ R(c) \sqrt{c_5} \sqrt{c_5 + c}} \left(1 - \frac{c}{c_R}\right) \partial \int_0^s \frac{du}{\sqrt{s - u}} \frac{dP}{du}, \quad (30a)$$

$$\sigma_{33}^C \approx \frac{1}{\pi \sqrt{c} \sqrt{\xi_0 - cS}} \frac{1}{g_3^+} \sqrt{1 - \frac{c}{c_5}} \left(1 - \frac{c}{c_R}\right) \partial \int_0^s \frac{du}{\sqrt{s-u}} \frac{dP}{du}. \quad (30b)$$

8. Transform inversions valid near C

Expressions for \dot{u}_k near C for $(x_3^0, x_3) \neq 0$ are also required. In view of (7c) and (26), $L(\dot{u}_k) = \beta p \bar{u}_k$ and \bar{u}_k can be generated from (15) and Appendix B by setting $(\bar{\Sigma}_k, \bar{\Delta}_1, \bar{\Delta}_2) = 0$ and using (25a). For $x_3 \neq 0$ a more explicit version of inversion formula (10) is useful:

$$\tilde{f}(p, q_1, q_2, x_3) \rightarrow f_\Psi(p, q, \chi) \exp(-pA|x_3|), \quad A = (A_\pm, A_5), \quad (31a)$$

$$\hat{f}(p, \xi, \chi, x_3) = -\frac{p^2}{2\pi} \int \frac{|q|}{q} f_\Psi(p, q, \chi) \exp[p(q\xi - A|x_3|)] dq. \quad (31b)$$

Result (28) follows from use of Cauchy theory to change the integration path in (10b) to the $\text{Re}(q)$ -axis. For (31b) the path is changed to a contour $q(A)$ in the complex q -plane along which the exponential term assumes the form $\exp(-pu)$, where u is real and positive. Because inversions valid near C are sufficient, local coordinates (r, ψ, ϕ) , centered on the portion of C that borders δA , are introduced, where

$$r = \sqrt{\xi^2 + x_3^2}, \quad \phi = \tan^{-1} \frac{x_3}{\xi} \quad (|\phi| < \pi). \quad (32)$$

In (31b) $q(A_\pm)$ and $q(A_5)$ for $r \approx 0$ have, respectively, asymptotic forms

$$-\frac{u}{rS_\pm}, \quad S_\pm = \cos \phi \mp ia_\pm \sin \phi, \quad (33a)$$

$$-\frac{u}{rS_5}, \quad S_5 = \cos \phi \mp ia_5 \sin \phi. \quad (33b)$$

It is noted that (25a), which depends on $1/\sqrt{-q}$, is associated in Appendix B with operator (\pm) . In the case of contour $q(A_5)$ therefore, (28a) and (28b), respectively, are replaced by

$$(\mp) \frac{p A_5^{(-)}}{\pi \sqrt{2r}} \int_+ \frac{du}{\sqrt{u}} \exp(-pu), \quad -\frac{p A_5^{(+)}}{\pi \sqrt{2r}} \int_+ \frac{du}{\sqrt{u}} \exp(-pu). \quad (34a)$$

In the case of contour $q(A_\pm)$, replacements are

$$(\mp) \frac{p A_\pm^{(-)}}{\pi \sqrt{2r}} \int_+ \frac{du}{\sqrt{u}} \exp(-pu), \quad -\frac{p A_\pm^{(+)}}{\pi \sqrt{2r}} \int_+ \frac{du}{\sqrt{u}} \exp(-pu). \quad (34b)$$

In (34), $(A_5^{(\pm)}, A_\pm^{(\pm)})$ are factors of the real (+) and imaginary (-) parts of $(\sqrt{S_5}, \sqrt{S_\pm})$:

$$A_5^{(\pm)} = \sqrt{1(\pm) \cos \phi / B_5}, \quad B_5 = \sqrt{1 - m_5 \sin^2 \phi}, \quad (35a)$$

$$A_\pm^{(\pm)} = \sqrt{1(\pm) \cos \phi / B_\pm}, \quad B_\pm = \sqrt{1 - m_\pm \sin^2 \phi}, \quad (35b)$$

$$m_5 = \sin^2 \chi - \frac{1}{d_5} (\sin^2 \chi - c^2), \quad m_\pm = \sin^2 \chi + \frac{D_\mp^2}{d_1}. \quad (35c)$$

Use of (32)–(35) gives for ($r \rightarrow 0$, $|\psi| < \pi/2$, $|\phi| < \pi$)

$$\dot{u}_1 \approx -\frac{K_3 M_1}{\mu \sqrt{2r}} \cos \chi, \quad \dot{u}_2 \approx \frac{K_3}{\mu \sqrt{2r}} \frac{M_2}{\sin \chi}, \quad \dot{u}_3 \approx (\pm) \frac{K_3 M_3}{\mu \sqrt{2r}}. \quad (36)$$

In (36) coefficient M_k is

$$M_1 = \frac{d_5 a_5 A_5^{(+)}}{\sin^2 \chi - c^2} + \frac{1}{2\omega_+ \omega_-} \left(N_- \frac{A_+^{(+)}}{a_+} - N_+ \frac{A_-^{(+)}}{a_-} \right), \quad (37a)$$

$$M_2 = \frac{1}{2m\omega_+ \omega_-} \left(\frac{q_+ N_-}{\sin \chi} \frac{A_+^{(+)}}{a_+} - \frac{q_- N_+}{\sin \chi} \frac{A_-^{(+)}}{a_-} \right), \quad (37b)$$

$$M_3 = \frac{d_5 A_5^{(-)} \cos^2 \chi}{\sin^2 \chi - c^2} + \frac{1}{2\omega_+ \omega_-} (N_- A_+^{(-)} - N_+ A_-^{(-)}). \quad (37c)$$

In (37) (K_3 , N_{\pm}) are defined by

$$K_3 = \frac{2V_4}{\pi g_3^+ R(c) \sqrt{c_5 + c}} \sqrt{d_5/c_5} \left(1 - \frac{c}{c_R}\right) \partial \int_0^s \frac{du}{\sqrt{s-u}} \frac{dP}{du}, \quad (38a)$$

$$N_{\pm} = m \sin^2 \chi - \frac{q_5 q_{\pm}}{\sin^2 \chi - c^2}. \quad (38b)$$

9. Criterion: dynamic energy release rate

A standard criterion for brittle fracture (see, e.g., [Freund 1972]) equates the rate at which surface energy is released to the rate of work associated with traction and relative displacements in the fracture zone F . If kinetic energy is included [Gdoutos 2005] the equation for this problem takes the form

$$D \iint_{\delta A} e_F dx_1^0 dx_2^0 = \iint_F \sigma_{33}^C \dot{\Delta}_3 dx_1^0 dx_2^0 + D \iiint_{123} \frac{1}{2} \rho \dot{u}_k \dot{u}_k dx_1^0 dx_2^0 dx_3^0. \quad (39)$$

Here e_F is the surface energy per unit area, and is generally assumed to be constant [de Boer et al. 1988; Skriver and Rosengard 1992]. Fracture zone F is a strip of infinitesimal thickness in the $x_1^0 x_2^0$ -plane that straddles the portion of C that borders δA . Subscript 123 signifies integration over the solid. Use of transport theory [Malvern 1969] and translating basis \mathbf{x} expressed in terms of $(\xi, \psi, x_3 = 0)$ gives for the first term in (39)

$$V_4 e_{FS} \int_{\Psi} c \sqrt{c^2 + (c')^2}, \quad f' = \frac{df}{d\psi}. \quad (40)$$

Here Ψ signifies integration over $|\psi| < \pi/2$. Use of \mathbf{x} for the integration over F gives

$$\int_{\Psi} d\Psi \int_{cs^-}^{cs^+} |x_0| \sigma_{33}^C \dot{\Delta}_3 dx_0. \quad (41a)$$

In light of (30) it can be shown [Freund 1972] that the integrand of (41a) features Dirac function $\delta(\xi_0 - cs)$. Moreover, linear behavior in s displayed in (40) places a restriction on $\partial_s P$; see, e.g., [Achenbach and Brock 1973]. That is, V must in general vary with time. One case, however, for which time-invariance is valid is

$$\partial P = p_C \sqrt{s} \quad (p_C > 0). \quad (41b)$$

Equation (30) and (41a) then give

$$-\pi p_C^2 \frac{s}{\pi} \int_{\Psi} V d\psi \sqrt{\frac{c_5 - c}{c_5 + c}} K_C^2 R(c), \quad K_C = \frac{-\sqrt{d_5}}{c_5 g_3^+ R(c)} \left(1 - \frac{c}{c_R}\right). \quad (41c)$$

Equation (36) is singular near C . The last integration in (39) can then be, *via* transport theory [Malvern 1969], taken over the surface of a tube of radius $r_C \rightarrow 0$ that encloses the portion of C that borders δA . Integration can be performed in terms of coordinates (29) and expressions (32), (37), (38), and (41b). The last term in (39) becomes

$$-s \frac{P_C^2}{\mu} \int_{\Psi} V d\psi \sqrt{c^2 + (c')^2} \frac{c_5 K_C^2}{c_5 + c} \int_{\Phi} E_{\Phi} \cos \phi d\phi, \quad (42a)$$

$$E_{\Phi} = M_1^2 \cos^2 \chi + \frac{M_2^2}{\sin^2 \chi} + M_3^2. \quad (42b)$$

Here Φ signifies integration over range $|\phi| < \pi$. Equation (40), (41c), and (42) all involve integration with respect to ψ , so that (39) gives for $|\psi| < \pi/2$

$$\sqrt{c^2 + (c')^2} + \pi \frac{p_C^2 K_C^2}{\mu e_F} \sqrt{\frac{c_5 - c}{c_5 + c}} R(c) - \frac{p_C^2 K_C^2}{4\mu e_F c_5} \frac{d_5 c}{c_5 + c} \sqrt{c^2 + (c')^2} \int_{\Phi} E_{\Phi} \cos \phi d\phi = 0. \quad (43)$$

10. Differential equation: observations

Here (43) is a nonlinear differential equation for c . As viewed in coordinates aligned with the initial rectilinear crack edge $c = c(\theta, \psi) = c(\chi)$. Equation (37) and (42b) show that the integrand of (43) involves quadratics in $(A_{\pm}^{(+)}, A_5^{(+)})$ and quadratics in $(A_{\pm}^{(-)}, A_5^{(-)})$. Use of (35) and (37) shows that

$$\int_{\Phi} [(A_{\pm}^{(+)})^2 + (A_{\pm}^{(-)})^2] \cos \phi d\phi = 0, \quad \int_{\Phi} [(A_5^{(+)})^2 + (A_5^{(-)})^2] \cos \phi d\phi = 0, \quad (44a)$$

$$\int_{\Phi} [A_{+}^{(+)} A_{-}^{(+)} + A_{+}^{(-)} A_{-}^{(-)}] \cos \phi d\phi = 0, \quad \int_{\Phi} [A_{\pm}^{(+)} A_5^{(+)} + A_{\pm}^{(-)} A_5^{(-)}] \cos \phi d\phi = 0. \quad (44b)$$

Use of (42b) and (44) in (43) gives

$$\int_{\Phi} E_{\Phi} \cos \phi d\phi = \frac{\pi}{4} E(c), \quad (45a)$$

$$\begin{aligned} E(c) = & T_+ \left(\frac{N_-}{a_+ \omega_+ \omega_-} \right)^2 \left[\frac{1}{m^2 \sin^2 \chi} (\sin^2 \chi - c^2 + D_-^2)^2 + \frac{D_-^2}{d_1} \right] \\ & + T_- \left(\frac{N_+}{a_- \omega_+ \omega_-} \right)^2 \left[\frac{1}{m^2 \sin^2 \chi} (\sin^2 \chi - c^2 + D_+^2)^2 + \frac{D_+^2}{d_1} \right] \\ & - 2T_+ \frac{N_+ N_-}{\omega_+^2 \omega_-^2} \left[\frac{\sqrt{d_1} (1 - c^2)}{\sqrt{c_+^2 - c^2} \sqrt{c_-^2 - c^2}} - 1 \right] + 4T_5 \frac{d_5 \cos^4 \chi}{\sin^2 \chi - c^2} \\ & + \frac{2d_5 \cos^2 \chi}{\omega_+ \omega_- (\sin^2 \chi - c^2)} \left[T_5^+ N_- \left(\frac{a_5}{a_+} - 1 \right) - T_5^- N_+ \left(\frac{a_5}{a_-} - 1 \right) \right]. \end{aligned} \quad (45b)$$

Equation (45b) involves terms

$$T_{\pm} = \frac{1}{\pi} \int_{\Phi} d\phi \frac{\cos^2 \phi}{\sqrt{1 - m_{\pm} \sin^2 \phi}}, \quad T_5 = \frac{1}{\pi} \int_{\Phi} d\phi \frac{\cos^2 \phi}{\sqrt{1 - m_5 \sin^2 \phi}}, \quad (46a)$$

$$T_{+}^{-} = \frac{1}{\pi} \int_{\Phi} d\phi \cos \phi \sqrt{1 + \frac{\cos \phi}{\sqrt{1 - m_{+} \sin^2 \phi}}} \sqrt{1 + \frac{\cos \phi}{\sqrt{1 - m_{-} \sin^2 \phi}}}, \quad (46b)$$

$$T_5^{\pm} = \frac{1}{\pi} \int_{\Phi} d\phi \cos \phi \sqrt{1 + \frac{\cos \phi}{\sqrt{1 - m_{\pm} \sin^2 \phi}}} \sqrt{1 + \frac{\cos \phi}{\sqrt{1 - m_5 \sin^2 \phi}}}. \quad (46c)$$

Equation (46a) gives complete elliptic integrals of the first (F) and second (E) kind when $0 < (m_{\pm}, m_5) < 1$, for example,

$$T_5 = 4 \left[F(\sqrt{m_5}) + \frac{1}{m_5} (E(\sqrt{m_5}) - F(\sqrt{m_5})) \right].$$

Equation (43) is somewhat complicated and opaque. Insight concerning $c(\theta, \psi)$, based partly on analytical expressions, is possible by considering values of parameter $V(\theta, \psi)$ that are not negligible, but well below critical, i.e., $c/c^* \leq 0.3$. Thus (43) is replaced with

$$\sqrt{c^2 + (c')^2} \left(1 + \frac{\pi p_C^2 d_5 c E(0)}{4\mu e_F c_5 4R^2(0)} \right) + \frac{\pi p_C^2 \sqrt{d_5}}{\mu e_F R(0) c_5} \approx 0. \quad (47)$$

Parameter c in (R, E) has been dropped and, in particular,

$$N_{\pm} = m \sin^2 \chi - (1 - d_{\mp}^2)(c_5^2 + d_5 \cos^2 \chi), \quad (48a)$$

$$a_{\pm} = \sqrt{\cos^2 \chi + d_{\mp}^2/d_1 \sin^2 \chi}, \quad a_5 = \frac{c_5}{\sqrt{d_5}}, \quad q_5 = c_5^2 + d_5 \cos^2 \chi, \quad (48b)$$

$$d_{\pm} = \frac{1}{2}(\sqrt{\Gamma + 2\sqrt{d_1 d_2}} \pm \sqrt{\Gamma - 2\sqrt{d_1 d_2}}), \quad d = \sqrt{\Gamma^2 - 4d_1 d_2}, \quad (48c)$$

$$m_{\pm} = (1 - d_{\mp}^2/d_1) \sin^2 \chi, \quad m_5 = (1 - 1/d_5) \sin^2 \chi. \quad (48d)$$

Equation (48c) indicates that attention henceforth focuses on Category 1 materials. However, the additional restriction that was placed on (21a) can be dropped.

11. Study of differential equation approximation

Equation (47) is also a nonlinear differential equation, but explicit in (c, c') . Terms $R(0)$, $E(0)$, and (48) are explicit functions of $(\cos^2 \chi, \sin^2 \chi)$, so that an analytic solution may be difficult, but after [Brock 2017a; 2017b] an approximate solution is feasible:

$$c(\theta, \psi) = c(\chi) \approx \sum_0^N b_k \cos^{2k} \chi \quad (0 < |\psi| < \pi/2). \quad (49)$$

Only the case $\theta = 0$ is treated in [Brock 2017a; 2017b] and expressions for coefficients which correspond to b_k are obtained by direct substitution into the nonlinear differential equation, with coefficients expanded in powers of $\cos^2 \psi$. The first three terms (b_0, b_1, b_2) are found to give results that are generally accurate to within three significant figures. Here dependence of $R(0)$, $E(0)$, and (48) on parameter

$\chi = \theta + \psi$ is more complicated. Therefore $N + 1$ equations for b_k are obtained by substitution of (49) into (47) for $N + 1$ values of χ . We here choose for illustration $N = 2$, $0 < \theta < \pi/2$ and values $\chi(0, \pi/2, \pi/4)$. The corresponding values for $(R(0), E(0))$ are obtained from (21a) and (45b) as (R_0, E_0) , (R_2, E_2) , and (R_4, E_4) , respectively, and are found in Appendix E. If kinetic energy is neglected by dropping the E-terms the three simultaneous equations give

$$b_0 = q_2, \quad (50a)$$

$$b_1 = -3q_2 - q_0 + 2\sqrt{q_4^2 - (q_0 - q_2)^2}, \quad (50b)$$

$$b_2 = 2[q_0 + q_2 - 2\sqrt{q_4^2 - (q_0 - q_2)^2}], \quad (50c)$$

$$q_0 = \frac{\pi p_C^2}{\mu e_F |R_0|}, \quad q_2 = \frac{\pi p_C^2 \sqrt{d_5}}{\mu e_F |R_2|}, \quad q_4 = \frac{\pi p_C^2 \sqrt{2d_5}}{\mu e_F |R_4| \sqrt{1 + d_5}}. \quad (50d)$$

Inclusion of kinetic energy gives for b_0

$$b_0 = \frac{1}{2Q_2}(1 - \sqrt{1 - 4q_2Q_2}). \quad (51a)$$

Expressions for (b_1, b_2) are obtained in light of (51a) from the simultaneous solution of a linear and a fourth-order algebraic equation:

$$b_1 + b_2 = q_{12} = \frac{1}{2Q_0}(1 - \sqrt{1 - 4q_0Q_0}) - b_0, \quad (51b)$$

$$[(q_{12}^0)^2 + q_{12}^2] \left(\frac{1}{Q_4} - q_{12}^0 \right)^2 = \left(\frac{q_4}{Q_4} \right)^2, \quad q_{12}^0 = b_0 + \frac{1}{4}(b_1 + q_{12}). \quad (51c)$$

In (51a)–(51c), Equation (50d) holds and

$$Q_0 = \frac{\pi p_C^2 \sqrt{d_5} |E_0|}{\mu e_F 4R_0^2}, \quad Q_2 = \frac{\pi p_C^2 d_5 |E_2|}{\mu e_F 4R_2^2}, \quad Q_4 = \frac{\pi p_C^2 \sqrt{2d_5} |E_4|}{\mu e_F \sqrt{1 + d_5} 4R_4^2}. \quad (51d)$$

12. Sample calculations: wave speeds

Consider a Category 1 material, similar to beryl, with properties [Payton 1983; de Boer et al. 1988; Skriver and Rosengard 1992]:

$$C_{44} = \mu = 6.894 \text{ GPa}, \quad e_F = 2.0 \text{ J/m}^2, \quad V_4 = 1569 \text{ m/s}, \\ d_1 = 4.11, \quad d_2 = 3.62, \quad d_5 = 2.0, \quad m = 2.017, \quad \Gamma = 11.81.$$

Equation (13) and (15a), respectively, define dimensionless body wave speeds (c_5, c_{\pm}) , and dimensionless Rayleigh speed c_R is a root of $R(c)$, defined in (21). They, and dimensionless crack speed parameter c , arise in the solution as viewed from the frame aligned with the original rectilinear crack edge. That is, they are functions of χ . For the Category 1 material chosen here, values of these dimensionless speeds are listed in Table 1 for various χ , (given for clarity in degrees °). Experience, e.g., [Brock 2013], indicates that factorizations of $R(c)$ may or may not arise for transverse isotropy. Thus the actual root-exhibiting

functions for given ψ are distinct in form. When $\chi = 0$ and $\chi = \pi/2$ respectively, for example,

$$4d_5\sqrt{d_5 - c^2}\sqrt{d_1 - c^2} - \sqrt{d_1/d_5}(2d_5 - c^2)^2 = 0, \quad c = c_R = 1.245,$$

$$[d_1(d_2 - c^2) - (m - 1)^2]\sqrt{1 - c^2} - \sqrt{d_1}c^2\sqrt{d_2 - c^2} = 0, \quad c = c_R = 0.954.$$

In addition to anisotropic behavior exhibited in [Table 1](#), location of speed parameter c^* shows that critical speed is not necessarily the Rayleigh wave value. In contrast to isotropic materials [[Achenbach 1973](#)], transonic crack extension rates may define the onset of critical behavior. This feature is noted in 3D analyses of other problems in transversely isotropic materials, e.g., sliding contact in the dynamic steady state [[Brock 2013](#)].

13. Sample calculations: crack extension rate parameters

For illustration in terms of the Category 1 material properties listed above, we consider a loading parameter $p_C = 3(10^4) \text{ N/m}^{3/2}$ that is consistent with small values of speed parameter V . For this value and the Category 1 material featured in [Table 1](#), (49) and (50) give the approximation valid when kinetic energy is neglected:

$$c \approx 0.12454 - 0.03404 \cos^2(\theta + \psi) + 0.00937 \cos^4(\theta + \psi). \tag{52a}$$

Here ($0 < \theta < \pi/2, \psi < \pi/2$). For the kinetic energy case, (49) and (51) give

$$c \approx 0.1249 - 0.0217 \cos^2(\theta + \psi) - 0.0032 \cos^4(\theta + \psi). \tag{52b}$$

In (52), $0 < \theta < \pi/2, \psi < \pi/2$ and it is noted that successive term coefficients decrease by orders of magnitude. Calculations based on (52a) and (52b) are displayed in [Table 2](#) and [Table 3](#), respectively.

As in [Table 1](#) anisotropic behavior is prominent. In particular the newly created crack surface δA is a semioval that is symmetric only when the original rectilinear crack edge coincides with the (principal) x_2^0 -direction. In the isotropic limit [[Brock 2017b](#)] δA is semicircular. [Table 2](#) and [Table 3](#) data also show that neglect of kinetic energy leads to an under-prediction of crack extension rate. The effect is however not large. Indeed, a more pronounced kinetic energy effect arises for crack extension in an isotropic, thermoelastic material [[Brock 2017a](#)].

$\chi = \theta + \psi$	c_5	c_+	c_-	c_R
0°	$\sqrt{2}$	2.027	1.0*	1.245
15°	1.39	1.998	1.042	1.226
30°	1.323	1.925	1.133	1.172
45°	1.225	1.857	1.19	1.099
60°	1.118	1.851	1.147	1.027
75°	1.034	1.886	1.048	0.974*
90°	1.0	1.903	1.0	0.954*

Table 1. Body (c_5, c_{\pm}) and Rayleigh (c_R) wave speed parameters (* signifies critical value c^*).

ψ	$c : (\theta = 0^\circ)$	$c : (\theta = 30^\circ)$	$c : (\theta = 45^\circ)$	$c : (\theta = 60^\circ)$
-90°	0.1245	0.1166	0.1099	0.1043
-75°	0.1223	0.1099	0.1043	0.1009
-60°	0.1166	0.1043	0.1009	0.0999
-45°	0.1099	0.1009	0.0999	0.1009
-30°	0.1043	0.0999	0.1009	0.1043
-15°	0.1009	0.1009	0.1043	0.1099
0°	0.0999	0.1043	0.1099	0.1166
15°	0.1009	0.1099	0.1166	0.1223
30°	0.1043	0.1166	0.1223	0.1245
45°	0.1099	0.1223	0.1245	0.1223
60°	0.1166	0.1245	0.1223	0.1166
75°	0.1223	0.1223	0.1166	0.1099
90°	0.1245	0.1166	0.1099	0.1043

Table 2. Dimensionless speed c for $p_C = 3(10^4) \text{ N/m}^{3/2}$ (kinetic energy neglected).

ψ	$c : (\theta = 0^\circ)$	$c : (\theta = 30^\circ)$	$c : (\theta = 45^\circ)$	$c : (\theta = 60^\circ)$
-90°	0.1249	0.1193	0.1132	0.1068
-75°	0.1233	0.1132	0.1068	0.1018
-60°	0.1193	0.1068	0.1018	0.0999
-45°	0.1132	0.1018	0.0999	0.1018
-30°	0.1068	0.0999	0.1018	0.1068
-15°	0.1018	0.1018	0.1068	0.1132
0°	0.0999	0.1068	0.1132	0.1193
15°	0.1018	0.1132	0.1193	0.1233
30°	0.1068	0.1193	0.1233	0.1249
45°	0.1132	0.1233	0.1249	0.1233
60°	0.1193	0.1249	0.1233	0.1193
75°	0.1233	0.1233	0.1193	0.1132
90°	0.12488	0.1193	0.1132	0.1068

Table 3. Dimensionless speed c for $p_C = 3(10^4) \text{ N/m}^{3/2}$ (kinetic energy included).

14. Some observations

This paper complements [Brock 2017a; 2017b] by considering 3D transient fracture at the edge of an initially undisturbed, closed semi-infinite slit in a transversely isotropic solid. Loading, however, is by point-force compression at the slit edges, whereas mixed-mode point-force loading at the edges and isotropic solids are treated in [Brock 2017a; 2017b]. Pure compression generates a semicircular crack edge in the isotropic solids, and shear loading distorts the profile. One goal of this paper is to illustrate the effects of anisotropy itself on crack profile. To this end, therefore, the case of the material rotational

symmetry axis is parallel to the crack plane, and the initially rectilinear crack edge does not align with a principal axis in that plane.

As in [Brock 2017a; 2017b] kinetic energy is included in imposition of the dynamic energy release rate criterion, and effects of inclusion on solution response is examined. Moreover, the same type of point-force time dependence is treated that guarantees dynamic similarity, i.e., the crack edge profile *might* not be circular, but *is* not time-dependent. The effect of anisotropy is seen to indeed be clear: pure compression loading creates a semioval crack profile. The under-prediction of crack edge extension rates caused by neglect of kinetic energy is also seen, although it is not as pronounced as that noted in [Brock 2017a; 2017b].

The rapid growth in time of the dynamic similarity-inducing point force may not be realistic. For example the selection for p_C and the Category 1 material used here produce in light of (41b) point-force function

$$P = 1.243(10^9)(t/s)^{3/2} \text{ N.}$$

Here t is time after initiation given in seconds (s), indicating that P rapidly achieves large values. Nevertheless, if P represents the short-time behavior of the point forces, the present analysis and those in [Brock 2017a; 2017a] can be valid for the study of transient fracture initiation. The short-time limitation is in fact imposed during the development of results in [Brock 2017a].

This paper is not a definitive study of the canonical problem of the semi-infinite slit in an unbounded, transversely isotropic material with point-force loading. In particular, absence of shear loading restricted the fracture process to the crack-opening mode. Moreover, some key expressions and associated calculations are based on a particular type of transversely isotropic material [Payton 1983]. Nevertheless, the paper is offered as a starting point and check for more ambitious efforts.

Appendix A

$$\text{Category 1: } 2\sqrt{d_1 d_2} \leq \Gamma \leq 1 + d_1 d_2 \quad (1 < d_1 < d_2),$$

$$d_1 + d_2 \leq \Gamma \leq 1 + d_1 d_2 \quad (1 < d_2 < d_1),$$

$$2d_1 \leq \Gamma \leq 1 + d_1^2 \quad (1 < d_2 = d_1),$$

$$\text{Category 2: } 1 + d_1 < \Gamma < d_1 + d_2 \quad (\Gamma^2 - 4d_1 d_2 < 0),$$

$$\text{Category 3: } \Gamma < 1 + d_1 \quad (\Gamma^2 - 4d_1 d_2 < 0).$$

Appendix B

Transform of (6a) gives six equations that uncouple into two sets. In Set 1,

$$P_5 - m q^2 \sin \chi \cos \chi (P_+ + P_-) = \bar{\Delta}_1, \quad (\text{B.1a})$$

$$Q_+ P_+ + Q_- P_- = \bar{\Delta}_2, \quad (\text{B.1b})$$

$$-2d_5 q \cos \chi P_5 + q \sin \chi [(m Q_5 - Q_+) P_+ + (m Q_5 - Q_-) P_-] = \bar{\Sigma}_3 / (\mu p), \quad (\text{B.1c})$$

$$P_5 = A_5 (U_5^{(+)} + U_5^{(-)}), \quad P_{\pm} = U_{\pm}^{(+)} + U_{\pm}^{(-)}, \quad Q_5 = C_0 + 2d_5 q^2 \cos^2 \psi. \quad (\text{B.1d})$$

Set 2 is defined by

$$q \cos \chi M_5 + mq \sin \chi (M_+ + M_-) = \bar{\Delta}_3, \quad (\text{B.2a})$$

$$Q_5 M_5 + 2d_5 m q^2 \sin \chi \cos \chi (M_+ + M_-) = \bar{\Sigma}_1 / (\mu p), \quad (\text{B.2b})$$

$$q^2 \sin \chi \cos \chi M_5 + (mq^2 \sin^2 \chi - Q_+) M_+ + (mq^2 \sin^2 \chi - Q_-) M_- = \bar{\Sigma}_2 / (\mu p), \quad (\text{B.2c})$$

$$M_5 = U_5^{(+)} - U_5^{(-)}, \quad M_{\pm} = A_{\pm} (U_{\pm}^{(+)} - U_{\pm}^{(-)}). \quad (\text{B.2d})$$

Solution of (B.1a)–(B.1c) gives

$$P_5 = \frac{1}{C_0} \left(q \cos \chi \frac{\bar{\Sigma}_3}{\mu p} + Q_5 \bar{\Delta}_1 + q^2 \sin \chi \cos \chi \bar{\Delta}_2 \right), \quad (\text{B.3a})$$

$$P_+ = \frac{Q_-}{m C_0 \Omega_+ \Omega_- q \sin \chi} \left(\frac{\bar{\Sigma}_3}{\mu p} + 2d_5 q \cos \chi \bar{\Delta}_1 + q \sin \chi \bar{\Delta}_2 \right) - \frac{\bar{\Delta}_2}{\Omega_+ \Omega_-}, \quad (\text{B.3b})$$

$$P_- = \frac{-Q_+}{m C_0 \Omega_- \Omega_+ q \sin \chi} \left(\frac{\bar{\Sigma}_3}{\mu p} + 2d_5 q \cos \chi \bar{\Delta}_1 + q \sin \chi \bar{\Delta}_2 \right) + \frac{\bar{\Delta}_2}{\Omega_- \Omega_+}. \quad (\text{B.3c})$$

The results for (B.2a)–(B.2c) are

$$M_5 = \frac{1}{C_0} \left(\frac{\bar{\Sigma}_1}{\mu p} - 2d_5 q \cos \chi \bar{\Delta}_3 \right), \quad (\text{B.4a})$$

$$M_+ = \frac{Q_-}{m C_0 \Omega_+ \Omega_- q \sin \chi} \left(Q_5 \bar{\Delta}_3 - q \cos \chi \frac{\bar{\Sigma}_1}{\mu p} \right) + \frac{1}{\Omega_+ \Omega_-} \left(\frac{\bar{\Sigma}_2}{\mu p} - q \cos \chi \bar{\Delta}_3 \right), \quad (\text{B.4b})$$

$$M_- = \frac{-Q_+}{m C_0 \Omega_- \Omega_+ q \sin \chi} \left(Q_5 \bar{\Delta}_3 - q \cos \chi \frac{\bar{\Sigma}_1}{\mu p} \right) + \frac{1}{\Omega_- \Omega_+} \left(\frac{\bar{\Sigma}_2}{\mu p} - q \cos \chi \bar{\Delta}_3 \right). \quad (\text{B.4c})$$

In light of (B.1d) and (B.2d),

$$U_5^{(\pm)} = \frac{1}{2} \left(\frac{P_5}{A_5} (\pm) M_5 \right), \quad U_{\pm}^{(\pm)} = \frac{1}{2} \left(P_{\pm} (\pm) \frac{M_{\pm}}{A_{\pm}} \right). \quad (\text{B.5})$$

Appendix C

$$S_1 = \frac{Q_5^2}{C_0} + \frac{4d_5^2 A_5}{C_0 \Omega_+ \Omega_-} (Q_- A_+ - Q_+ A_-) q^2 \sin \chi \cos \chi, \quad (\text{C.1a})$$

$$S_{12} = \frac{1}{C_0} \left[Q_5 + \frac{2d_5 A_5}{\Omega_+ \Omega_-} q^2 \sin \chi \cos \chi (Q_- A_+ - Q_+ A_-) \right] + \frac{2md_5}{\Omega_+ \Omega_-} (A_- - A_+) q^2 \sin \psi \cos \chi, \quad (\text{C.1b})$$

$$S_2 = \frac{1}{C_0} \left[\cos^2 \chi + \frac{2A_5}{\Omega_+ \Omega_-} (Q_- A_+ - Q_+ A_-) \right] q^2 \sin^2 \chi \\ + \frac{2A_5}{\Omega_+ \Omega_-} [A_- (2mq^2 \sin^2 \chi - Q_-) - A_+ (2mq^2 \sin^2 \chi - Q_+)], \quad (\text{C.1c})$$

$$S_3 = \frac{1}{C_0} \left[4d_5^2 q^2 \cos^2 \chi + \frac{Q_5^2}{\Omega_+ \Omega_- A_5} \left(\frac{Q_-}{A_+} - \frac{Q_+}{A_-} \right) \right] \\ + \frac{q^2 \sin^2 \chi}{\Omega_+ \Omega_- A_5} \left[\frac{1}{A_-} (2mQ_5 - Q_-) - \frac{1}{A_+} (2mQ_5 - Q_+) \right], \quad (\text{C.2})$$

$$T_1 = \frac{d_5}{\Omega_+ \Omega_-} [A_- (Q_+ - mQ_5) - A_+ (Q_- - mQ_5)] q^2 \sin \chi \cos \chi, \quad (\text{C.3a})$$

$$T_2 = \frac{Q_5}{\Omega_+ \Omega_-} [A_- (Q_- - mq^2 \sin^2 \chi) - A_+ (Q_+ - mq^2 \sin^2 \chi)] \\ + \frac{1}{\Omega_+ \Omega_-} [A_- (Q_+ - mC) - A_+ (Q_- - mC)] q^2 \sin^2 \chi. \quad (\text{C.3b})$$

Appendix D

For a Category 1 material with $c_R < c_5 < c_-$,

$$G_3^+ = \exp \left[-\frac{1}{\pi} \int \frac{du}{u-c} \frac{\Phi_3}{1+q(u-c)} \right], \quad (\text{D.1a})$$

$$G_3^- = \exp \left[\frac{1}{\pi} \int \frac{du}{u+c} \frac{\Phi_3}{1-q(u+c)} \right]. \quad (\text{D.1b})$$

Integration is over the range $c_5 < u < c_+$, where

$$c_5 < u < c_- : \Phi_3 = \tan^{-1} \frac{a_- p_+ - a_+ p_-}{4d_5^2 \omega_+ \omega_- a_+ a_- \alpha_5 \cos^2 \chi}, \quad (\text{D.2a})$$

$$c_- < u < c_+ : \Phi_3 = \tan^{-1} \frac{p_+}{a_+ p_- - 4d_5^2 \omega_+ \omega_- \alpha_5 \cos^2 \chi}, \quad (\text{D.2b})$$

$$p_{\pm} = q_5^2 q_{\mp} + (q_{\pm} - 2mq_5) \sin^2 \chi (\sin^2 \chi - u^2), \quad (\text{D.3a})$$

$$\alpha_- = \sqrt{-\cos^2 \chi - D_+^2/d_1}, \quad \alpha_5 = \frac{1}{\sqrt{d_5}} \sqrt{u^2 c_5^2}. \quad (\text{D.3b})$$

Here $(a_5, q_5, a_{\pm}, q_{\pm}, D_+, \omega_{\pm})$ are functions of u (see (21)).

Appendix E

$$\chi = 0 : m_{\pm} = m_5 = 0, \quad (\text{E.1a})$$

$$R_0 = -2d_5 \left(1 - \frac{d_5}{d_1} \right), \quad E_0 = -2 \left(1 + \frac{d_5}{d_1} \right) \left(1 - \frac{d_5}{8d_1} \right), \quad (\text{E.1b})$$

$$\chi = \pi/2 : m_{\pm} = 1 - \frac{d_{\mp}}{d_1}, \quad m_5 = 1 - \frac{1}{d_5}, \quad N_{\pm} = m - 1 + d_{\mp}^2, \quad (\text{E.2a})$$

$$R_2 = -\sqrt{\frac{d_5}{d_2}} \frac{2m - 2 + \Gamma}{\sqrt{\Gamma + 2\sqrt{d_1 d_2}}}, \quad (\text{E.2b})$$

$$E_2 = \frac{T_+ N_-^2}{\pi d^2 d_-^2} (1 - d_-^2) \left[1 + \frac{d_1}{m^2} (1 - d_-^2) \right] + \frac{T_- N_+^2}{\pi d^2 d_+^2} (1 - d_+^2) \left[1 + \frac{d_1}{m^2} (1 - d_+^2) \right] - \frac{2T_+^-}{\pi d^2} N_+ N_- (\sqrt{d_1/d_2} - 1), \quad (E.2c)$$

$$\chi = \pi/4 : m_{\pm} = \frac{1}{2} \left(1 - \frac{d_{\mp}^2}{d_1} \right), \quad m_5 = \frac{1}{2} \left(1 - \frac{1}{d_5} \right), \quad (E.3a)$$

$$N_{\pm} = \frac{1}{2} [m - (1 + 2d_5)(1 - d_{\mp}^2)], \quad a_{\pm}^0 = \frac{1}{\sqrt{2}} \sqrt{1 + d_{\mp}^2/d_1}, \quad (E.3b)$$

$$R_4 = 4d_5^2 - \frac{\sqrt{d_5}}{a_-^0 d \sqrt{2} \sqrt{1 + d_5}} [(1 - d_-^2)(1 + 2d_5)^2 + 1 - d_+^2 - 2m(1 + 2d_5)] + \frac{\sqrt{d_5}}{a_+^0 d \sqrt{2} \sqrt{1 + d_5}} [(1 - d_+^2)(1 + 2d_5)^2 + 1 - d_-^2 - 2m(1 + 2d_5)], \quad (E.3c)$$

$$E_4 = \frac{2T_+ N_-^2}{\pi (a_+^0 d)^2 d_1} (1 - d_-^2) \left[1 + \frac{d_1}{m^2} (1 - d_-^2) \right] + \frac{2T_- N_+^2}{\pi (a_-^0 d)^2 d_1} (1 - d_+^2) \left[1 + \frac{d_1}{m^2} (1 - d_+^2) \right] - \frac{4T_+^-}{\pi d^2} N_+ N_- \left(\frac{\sqrt{d_1}}{c_+ c_-} - 1 \right) + \frac{2T_5}{\pi} d_5 + \frac{4\sqrt{d_5}}{\pi d} \left[T_5^- N_+ \left(\frac{c_5}{a_-^0} - \sqrt{d_5} \right) - T_5^+ N_- \left(\frac{c_5}{a_+^0} - \sqrt{d_5} \right) \right]. \quad (E.3d)$$

References

- [Abramowitz and Stegun 1972] M. Abramowitz and I. A. Stegun (editors), *Handbook of mathematical functions*, Dover, New York, 1972.
- [Achenbach 1973] J. D. Achenbach, *Wave propagation in elastic solids*, North-Holland, Amsterdam, 1973.
- [Achenbach and Brock 1973] J. D. Achenbach and L. M. Brock, "On quasistatic and dynamic fracture", pp. 529–541 in *Proceedings of an international conference on Dynamic Crack Propagation*, 1973.
- [Barber 1992] J. R. Barber, *Elasticity: solid mechanics and its applications*, Kluwer, Dordrecht, 1992.
- [Brock 2012] L. M. Brock, "Two cases of rapid contact on an elastic half-plane: the sliding ellipsoid, rolling sphere", *J. Mech. Mater. Struct.* **7**:5 (2012), 469–483.
- [Brock 2013] L. M. Brock, "Rapid sliding contact in three dimensions by dissimilar elastic bodies: effects of sliding speed and transverse isotropy", *J. Mech. Mater. Struct.* **8**:8 (2013), 461–477.
- [Brock 2017a] L. M. Brock, "Transient analysis of fracture initiation in a coupled thermoelastic solid", *J. Mech. Mater. Struct.* **12**:5 (2017), 667–688.
- [Brock 2017b] L. M. Brock, "Transient growth of a planar crack in three dimensions: mixed mode", *J. Mech. Mater. Struct.* **12**:3 (2017), 313–328.
- [Brock and Achenbach 1973] L. M. Brock and J. D. Achenbach, "Extension of an interface flaw under the influence of transient waves", *Int. J. Solids Struct.* **9**:1 (1973), 53–68.
- [de Boer et al. 1988] F. R. de Boer, R. Boom, W. C. M. Mattens, A. R. Miedema, and A. K. Niessen, *Cohesion in metals*, North-Holland, Amsterdam, 1988.
- [Freund 1972] L. B. Freund, "Energy flux into the tip of an extending crack in an elastic solid", *J. Elasticity* **2**:4 (1972), 341–349.
- [Freund 1990] L. B. Freund, *Dynamic fracture mechanics*, Cambridge University Press, 1990.
- [Gdoutos 2005] E. E. Gdoutos, *Fracture mechanics: an introduction*, Solid mechanics and its applications **123**, Springer, New York, 2005.

- [Jones 1999] R. M. Jones, *Mechanics of composite materials*, 2nd ed., Taylor and Francis, New York, 1999.
- [Malvern 1969] L. S. Malvern, *Introduction to the mechanics of continuous media*, Prentice-Hall, Englewood Cliffs, NJ, 1969.
- [Morse and Feshbach 1953] P. F. Morse and H. Feshbach, *Methods of theoretical physics*, McGraw-Hill, New York, 1953.
- [Payton 1983] R. G. Payton, *Elastic wave propagation in transversely isotropic solids*, Martinus Nijhoff, The Hague, 1983.
- [Scott and Miklowitz 1967] R. A. Scott and J. Miklowitz, “[Transient elastic waves in anisotropic plates](#)”, *J. Appl. Mech. (ASME)* **34**:1 (1967), 104–110.
- [Skriver and Rosengaard 1992] H. L. Skriver and N. M. Rosengaard, “[Surface energy and work functions of elemental metals](#)”, *Phys. Rev. B* **46**:11 (1992), 7157–7168.
- [Sneddon 1972] I. N. Sneddon, *The use of integral transforms*, McGraw-Hill, New York, 1972.

Received 6 Oct 2017. Accepted 13 Feb 2018.

LOUIS M. BROCK: louis.brock@uky.edu

Department of Mechanical Engineering, University of Kentucky, Lexington, KY, United States

ESHELBY INCLUSION OF ARBITRARY SHAPE IN ISOTROPIC ELASTIC MATERIALS WITH A PARABOLIC BOUNDARY

XU WANG, LIANG CHEN AND PETER SCHIAVONE

We employ analytic continuation and conformal mapping techniques to derive analytic solutions for Eshelby's problem of an elastic inclusion of arbitrary shape in an isotropic elastic plane with parabolic boundary. The region of the physical (z -) plane lying below the parabola is mapped (conformally) onto the lower half of the image (ξ -) plane. The corresponding boundary value problem is then analyzed in the ξ -plane. A second conformal mapping, which maps the exterior of the region occupied by the (simply-connected) inclusion in the ξ -plane onto the exterior of the unit circle, is then used to construct an auxiliary function of ξ which, when used together with analytic continuation, allows us to extend our analysis to an inclusion of arbitrary shape.

1. Introduction

Eshelby's classic problem concerning a subdomain (inclusion) undergoing uniform stress-free eigenstrains continues to inspire researchers working in several areas of materials science (see, for example, [Zhou et al. 2013] for a recent review). The two-dimensional Eshelby's problem of an inclusion of arbitrary shape located in the vicinity of a straight boundary has been well-studied and is now considered to be solved [Ru 1999; Ru 2000; Ru 2003; Wang 2004; Wang and Schiavone 2015; Wang and Zhou 2014]. In contrast, there are relatively few studies pertaining to the corresponding problem of an Eshelby inclusion of arbitrary shape lying near an open *curvilinear* boundary. The importance of this class of problem can be illustrated, for example, by considering the case when the inclusion lies in an elastic plane with parabolic boundary. In this case, the parabola represents the blunt crack tip of a crack present in some fractured material and the inclusion perhaps a transformation strain spot of arbitrary shape. In this way, the corresponding model can be used to study the shielding or anti-shielding effect of the transformation strain spot on a nearby crack.

In this paper, we do, in fact, consider the Eshelby's problem of an inclusion of arbitrary shape in an isotropic elastic plane with parabolic boundary. Our approach differs from that used by [Ru 1999] for the analogous problem involving a straight boundary (as mentioned above) in that instead of analyzing the corresponding boundary value problem in the physical plane, our analysis is confined to the image plane. Specifically, the region below the parabola is first mapped onto the lower half-plane in the image (ξ -) plane in which the boundary value problem is then analyzed. A conformal mapping function which maps the exterior of the region occupied by the (simply-connected) inclusion in the ξ -plane onto the exterior of the unit circle [Savin 1961; England 1971] is then used to construct an auxiliary function $D(\xi)$ with which the problem can be solved using analytic continuation.

Keywords: Eshelby inclusion, parabolic boundary, conformal mapping, analytic continuation, auxiliary function.

The paper is structured as follows. Muskhelishvili's complex variable formulations for two-dimensional isotropic elasticity are given in [Section 2](#). Analytic solutions to the corresponding problems involving in-plane and anti-plane shear eigenstrains are derived in [Section 3](#). Several specific examples are presented in [Section 4](#) to illustrate the method. Finally, conclusions are drawn in [Section 5](#).

2. Complex variable formulations

For plane deformations of an isotropic elastic material, the stresses $(\sigma_{11}, \sigma_{22}, \sigma_{12})$, displacements (u_1, u_2) and stress functions (ϕ_1, ϕ_2) can be expressed in terms of two analytic functions $\varphi(z)$ and $\psi(z)$ of the complex variable $z = x_1 + ix_2$ as follows [[Muskhelishvili 1953](#); [Ting 1996](#)]:

$$\sigma_{11} + \sigma_{22} = 2(\varphi'(z) + \overline{\varphi'(z)}), \quad \sigma_{22} - \sigma_{11} + 2i\sigma_{12} = 2(\bar{z}\varphi''(z) + \psi'(z)), \quad (1)$$

$$2\mu(u_1 + iu_2) = \kappa\varphi(z) - z\overline{\varphi'(z)} - \overline{\psi(z)}, \quad \phi_1 + i\phi_2 = i(\varphi(z) + z\overline{\varphi'(z)} + \overline{\psi(z)}), \quad (2)$$

where $\kappa = 3 - 4\nu$ for plane strain, $\kappa = (3 - \nu)/(1 + \nu)$ for plane stress and $\mu, \nu (0 \leq \nu \leq 1/2)$ are the shear modulus and Poisson's ratio, respectively. In addition, the stresses are related to the stress functions through

$$\begin{aligned} \sigma_{11} &= -\phi_{1,2}, & \sigma_{12} &= \phi_{1,1}, \\ \sigma_{21} &= -\phi_{2,2}, & \sigma_{22} &= \phi_{2,1}. \end{aligned} \quad (3)$$

Under the assumption of anti-plane shear deformations of an isotropic elastic material, the two shear stress components $(\sigma_{31}, \sigma_{32})$, the out-of-plane displacement u_3 and the stress function ϕ_3 can be expressed in terms of a single analytic function $f(z)$ of the complex variable $z = x_1 + ix_2$ as

$$\sigma_{32} + i\sigma_{31} = \mu f'(z), \quad \phi_3 + i\mu u_3 = \mu f(z), \quad (4)$$

where the two stress components can be expressed in terms of the stress function ϕ_3 as

$$\sigma_{32} = \phi_{3,1}, \quad \sigma_{31} = -\phi_{3,2}. \quad (5)$$

3. An inclusion in a region with parabolic boundary

As shown in [Figure 1](#), we consider an isotropic elastic material that occupies the region:

$$x_2 \leq ax_1^2, \quad a \geq 0, \quad (6)$$

the traction-free boundary of which is a parabola described by

$$x_2 = ax_1^2. \quad (7)$$

The parabola reduces to a semi-infinite crack when $a \rightarrow \infty$ and a straight boundary when $a = 0$. The isotropic plane with parabolic boundary contains an internal subdomain undergoing uniform in-plane and anti-plane stress-free eigenstrains $(\varepsilon_{11}^*, \varepsilon_{22}^*, \varepsilon_{12}^*)$ and $(\varepsilon_{31}^*, \varepsilon_{32}^*)$. Let S_2 and S_1 denote, respectively, the subdomain (the Eshelby inclusion) and its exterior while Γ denotes the perfectly bonded interface separating S_2 and S_1 . In what follows, the subscripts 1 and 2 refer to S_1 and S_2 , respectively.

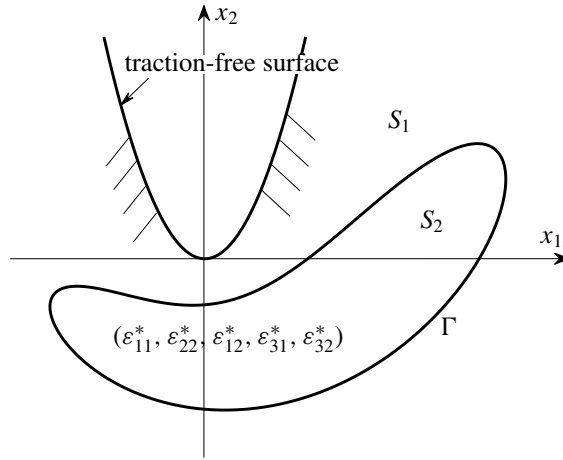


Figure 1. An Eshelby inclusion of arbitrary shape in an isotropic elastic plane with a parabolic boundary.

We introduce the following conformal mapping function [Ting et al. 2001]:

$$z = \omega(\xi) = \xi + ia\xi^2, \quad \xi = \omega^{-1}(z) = \frac{\sqrt{1 + 4iaz} - 1}{2ia}, \quad \text{Im } \xi \leq 0. \tag{8}$$

With reference to Figure 2, the parabola itself is mapped onto the real axis in the ξ -plane and the region below the parabola onto the lower half ξ -plane. The inclusion $z \in S_2$ is mapped onto $\xi \in \Omega_2$, the matrix $z \in S_1$ onto $\xi \in \Omega_1$ and the interface $z \in \Gamma$ is mapped onto $\xi \in L$. The elliptical shape of L in Figure 2 is chosen simply for illustrative purposes; in fact L may be of arbitrary shape. For convenience and without loss of generality, we write

$$\varphi_j(\xi) = \varphi_j(\omega(\xi)), \quad \psi_j(\xi) = \psi_j(\omega(\xi)), \quad f_j(\xi) = f_j(\omega(\xi)), \quad j = 1, 2.$$

In what follows, we derive analytic solutions in the case of both in-plane and anti-plane eigenstrains.

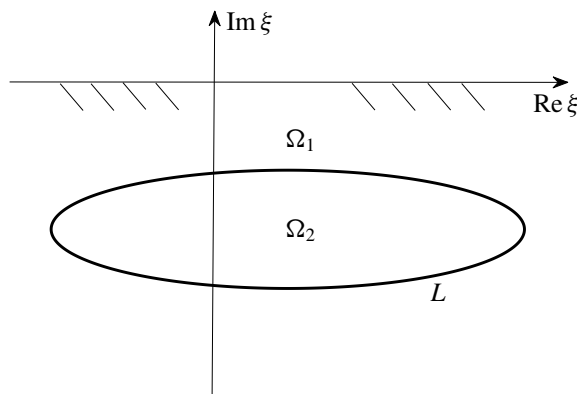


Figure 2. The problem in the ξ -plane.

3.1. In-plane eigenstrains (ε_{11}^* , ε_{22}^* , ε_{12}^*). In this case, the boundary value problem in the ξ -plane takes the following form:

$$\begin{aligned} \kappa \varphi_1(\xi) - \frac{\omega(\xi)}{\omega'(\xi)} \overline{\varphi_1'(\xi)} - \overline{\psi_1(\xi)} &= \kappa \varphi_2(\xi) - \frac{\omega(\xi)}{\omega'(\xi)} \overline{\varphi_2'(\xi)} - \overline{\psi_2(\xi)} + 2\mu[\delta_1 \omega(\xi) + (\delta_2 + i\delta_3) \overline{\omega(\xi)}], \\ \varphi_1(\xi) + \frac{\omega(\xi)}{\omega'(\xi)} \overline{\varphi_1'(\xi)} + \overline{\psi_1(\xi)} &= \varphi_2(\xi) + \frac{\omega(\xi)}{\omega'(\xi)} \overline{\varphi_2'(\xi)} + \overline{\psi_2(\xi)}, \quad \xi \in L; \end{aligned} \quad (9a)$$

$$\varphi_1(\xi) + \frac{\omega(\xi)}{\omega'(\xi)} \overline{\varphi_1'(\xi)} + \overline{\psi_1(\xi)} = 0, \quad \text{Im } \xi = 0^-; \quad (9b)$$

$$\varphi_1(\xi) \cong O(1), \quad \psi_1(\xi) \cong O(1), \quad |\xi| \rightarrow \infty, \quad (9c)$$

where the real numbers δ_1 , δ_2 and δ_3 are related to the in-plane eigenstrains through

$$\delta_1 = \frac{\varepsilon_{11}^* + \varepsilon_{22}^*}{2}, \quad \delta_2 = \frac{\varepsilon_{11}^* - \varepsilon_{22}^*}{2}, \quad \delta_3 = \varepsilon_{12}^*. \quad (10)$$

After straightforward algebraic manipulations, the two interface conditions in (9a) can be expressed equivalently as

$$\begin{aligned} \varphi_1(\xi) &= \varphi_2(\xi) + \frac{2\mu}{\kappa + 1} [\delta_1 \omega(\xi) + (\delta_2 + i\delta_3) \overline{\omega(\xi)}], \\ \psi_1(\xi) + \frac{\overline{\omega(\xi)}}{\omega'(\xi)} [\varphi_1'(\xi) - \varphi_2'(\xi)] &= \psi_2(\xi) - \frac{2\mu}{\kappa + 1} [\delta_1 \overline{\omega(\xi)} + (\delta_2 - i\delta_3) \omega(\xi)], \quad \xi \in L. \end{aligned} \quad (11)$$

If $z \in S_2$ is simply connected, $\xi \in \Omega_2$ is also simply connected. Thus, there exists a conformal mapping $\xi = w(\eta)$ that maps the exterior of Ω_2 in the ξ -plane onto the exterior of the unit circle in the η -plane [Savin 1961; England 1971]. As a result, an auxiliary function $D(\xi)$ can be constructed as follows:

$$\overline{\omega(\xi)} = \bar{\xi} - ia\bar{\xi}^2 = \bar{w} \left(\frac{1}{w^{-1}(\xi)} \right) - ia \left[\bar{w} \left(\frac{1}{w^{-1}(\xi)} \right) \right]^2 = D(\xi), \quad \xi \in L. \quad (12)$$

In addition, the auxiliary function $D(\xi)$ is analytic in the exterior of Ω_2 except at the point at infinity, where it has a pole of finite degree, namely

$$D(\xi) = P(\xi) + O(\xi^{-1}), \quad |\xi| \rightarrow \infty, \quad (13)$$

where $P(\xi)$ is a polynomial of order $2N$ in ξ if $\xi = w(\eta)$ is a polynomial of order N in $1/\eta$.

Using (12), Equation (11) can be rewritten as

$$\begin{aligned} \varphi_1(\xi) - \frac{2\mu}{\kappa + 1} (\delta_1 \omega(\xi) + (\delta_2 + i\delta_3) D(\xi)) &= \varphi_2(\xi), \\ \psi_1(\xi) + \frac{2\mu}{\kappa + 1} \left[2\delta_1 D(\xi) + (\delta_2 + i\delta_3) \frac{D(\xi)D'(\xi)}{\omega'(\xi)} + (\delta_2 - i\delta_3) \omega(\xi) \right] &= \psi_2(\xi), \quad \xi \in L. \end{aligned} \quad (14)$$

The asymptotic behavior of $D(\xi)D'(\xi)/\omega'(\xi)$ at infinity is given by

$$\frac{D(\xi)D'(\xi)}{\omega'(\xi)} = Q(\xi) + O(\xi^{-1}), \quad |\xi| \rightarrow \infty, \quad (15)$$

where $Q(\xi)$ is a polynomial of order $2N(2N - 1)$ in ξ if $\xi = w(\eta)$ is a polynomial of order N in $1/\eta$. In view of (13) and (15), Equation (14) can be recast into the form

$$\begin{aligned} \varphi_1(\xi) - \frac{2\mu}{\kappa + 1}(\delta_2 + i\delta_3)(D(\xi) - P(\xi)) &= \varphi_2(\xi) + \frac{2\mu}{\kappa + 1}(\delta_1\omega(\xi) + (\delta_2 + i\delta_3)P(\xi)), \\ \psi_1(\xi) + \frac{2\mu}{\kappa + 1} \left[2\delta_1(D(\xi) - P(\xi)) + (\delta_2 + i\delta_3) \left(\frac{D(\xi)D'(\xi)}{\omega'(\xi)} - Q(\xi) \right) \right] \\ &= \psi_2(\xi) - \frac{2\mu}{\kappa + 1}((\delta_2 - i\delta_3)\omega(\xi) + 2\delta_1P(\xi) + (\delta_2 + i\delta_3)Q(\xi)), \quad \xi \in L. \end{aligned} \quad (16)$$

We now define two auxiliary functions $\Phi(\xi)$ and $\Psi(\xi)$ by

$$\begin{aligned} \Phi(\xi) &= \begin{cases} \varphi_1(\xi) - \frac{2\mu}{\kappa + 1}(\delta_2 + i\delta_3)(D(\xi) - P(\xi)), & \xi \in \Omega_1, \\ \varphi_2(\xi) + \frac{2\mu}{\kappa + 1}(\delta_1\omega(\xi) + (\delta_2 + i\delta_3)P(\xi)), & \xi \in \Omega_2, \end{cases} \\ \Psi(\xi) &= \begin{cases} \psi_1(\xi) + \frac{2\mu}{\kappa + 1} \left[2\delta_1(D(\xi) - P(\xi)) + (\delta_2 + i\delta_3) \left(\frac{D(\xi)D'(\xi)}{\omega'(\xi)} - Q(\xi) \right) \right], & \xi \in \Omega_1, \\ \psi_2(\xi) - \frac{2\mu}{\kappa + 1}((\delta_2 - i\delta_3)\omega(\xi) + 2\delta_1P(\xi) + (\delta_2 + i\delta_3)Q(\xi)), & \xi \in \Omega_2. \end{cases} \end{aligned} \quad (17)$$

It is seen from the above definition and (16) that $\Phi(\xi)$ and $\Psi(\xi)$ are continuous across L and then analytic in the lower half ξ -plane including the point at infinity. Now the traction-free condition in (9b) can be given in terms of $\Phi(\xi)$ and $\Psi(\xi)$ as follows:

$$\begin{aligned} \Phi^-(\xi) + \frac{2\mu}{\kappa + 1}(\delta_2 - i\delta_3) \frac{\omega(\xi)}{\bar{\omega}'(\xi)} (\bar{D}'(\xi) - \bar{P}'(\xi)) - \frac{2\mu}{\kappa + 1} \left[2\delta_1(\bar{D}(\xi) - \bar{P}(\xi)) + (\delta_2 - i\delta_3) \left(\frac{\bar{D}(\xi)\bar{D}'(\xi)}{\bar{\omega}'(\xi)} - \bar{Q}(\xi) \right) \right] \\ + \frac{3\mu}{\kappa + 1} \frac{(\delta_3 + i\delta_2)(\overline{D'[i(2a)^{-1}] - P'[i(2a)^{-1}]})}{2a(1 - 2ia\xi)} + \frac{2\mu}{\kappa + 1} \frac{(\delta_2 - i\delta_3)\overline{D[i(2a)^{-1}]D'[i(2a)^{-1}]}}{1 - 2ia\xi} \\ = -\bar{\Psi}^+(\xi) - \frac{\omega(\xi)}{\bar{\omega}'(\xi)} \bar{\Phi}'^+(\xi) - \frac{2\mu}{\kappa + 1}(\delta_2 + i\delta_3)(D(\xi) - P(\xi)) \\ + \frac{3\mu}{\kappa + 1} \frac{(\delta_3 + i\delta_2)[\overline{D'[i(2a)^{-1}] - P'[i(2a)^{-1}]}]}{2a(1 - 2ia\xi)} + \frac{2\mu}{\kappa + 1} \frac{(\delta_2 - i\delta_3)\overline{D[i(2a)^{-1}]D'[i(2a)^{-1}]}}{1 - 2ia\xi}, \end{aligned} \quad \text{Im } \xi = 0. \quad (18)$$

The left and right sides of (18) are analytic in the lower and upper half-planes, respectively, including the point at infinity. By applying Liouville's theorem, we conclude that the left and right sides of (18) are identically zero. We thus arrive at the following expressions for $\Phi(\xi)$ and $\Psi(\xi)$:

$$\begin{aligned} \Phi(\xi) &= -\frac{2\mu}{\kappa+1}(\delta_2-i\delta_3)\frac{\omega(\xi)}{\bar{\omega}'(\xi)}(\bar{D}'(\xi)-\bar{P}'(\xi))+\frac{2\mu}{\kappa+1}\left[2\delta_1(\bar{D}(\xi)-\bar{P}(\xi))+(\delta_2-i\delta_3)\left(\frac{\bar{D}(\xi)\bar{D}'(\xi)}{\bar{\omega}'(\xi)}-\bar{Q}(\xi)\right)\right] \\ &\quad -\frac{3\mu}{\kappa+1}\frac{(\delta_3+i\delta_2)(\overline{D'[i(2a)^{-1}]}-\overline{P'[i(2a)^{-1}]})}{2a(1-2ia\xi)}-\frac{2\mu}{\kappa+1}\frac{(\delta_2-i\delta_3)\overline{D[i(2a)^{-1}]D'[i(2a)^{-1}]}}{1-2ia\xi}, \\ \Psi(\xi)+\frac{\bar{\omega}(\xi)}{\omega'(\xi)}\Phi'(\xi) &= -\frac{2\mu}{\kappa+1}(\delta_2-i\delta_3)(\bar{D}(\xi)-\bar{P}(\xi)) \\ &\quad +\frac{3\mu}{\kappa+1}\frac{(\delta_3-i\delta_2)(D'[i(2a)^{-1}]-P'[i(2a)^{-1}])}{2a(1+2ia\xi)}+\frac{2\mu}{\kappa+1}\frac{(\delta_2+i\delta_3)D[i(2a)^{-1}]D'[i(2a)^{-1}]}{1+2ia\xi}, \end{aligned}$$

Im $\xi \leq 0$. (19)

It is not difficult to verify that $\Phi(\xi)$ is regular at $\xi = -i/2a$. It follows from (17) and (19) that

$$\begin{aligned} \frac{\kappa+1}{2\mu}\varphi_1(\xi) &= (\delta_2+i\delta_3)(D(\xi)-P(\xi))-(\delta_2-i\delta_3)\frac{\omega(\xi)}{\bar{\omega}'(\xi)}(\bar{D}'(\xi)-\bar{P}'(\xi)) \\ &\quad +2\delta_1(\bar{D}(\xi)-\bar{P}(\xi))+(\delta_2-i\delta_3)\left(\frac{\bar{D}(\xi)\bar{D}'(\xi)}{\bar{\omega}'(\xi)}-\bar{Q}(\xi)\right) \\ &\quad -\frac{3(\delta_3+i\delta_2)(\overline{D'[i(2a)^{-1}]}-\overline{P'[i(2a)^{-1}]})}{4a(1-2ia\xi)}-\frac{(\delta_2-i\delta_3)\overline{D[i(2a)^{-1}]D'[i(2a)^{-1}]}}{1-2ia\xi}, \\ \frac{\kappa+1}{2\mu}\psi_1(\xi) &= -\frac{\kappa+1}{2\mu}\frac{\bar{\omega}(\xi)\varphi_1'(\xi)}{\omega'(\xi)}-2\delta_1(D(\xi)-P(\xi))-(\delta_2+i\delta_3)\left(\frac{D(\xi)D'(\xi)}{\omega'(\xi)}-Q(\xi)\right) \\ &\quad +(\delta_2+i\delta_3)\frac{\bar{\omega}(\xi)}{\omega'(\xi)}(D'(\xi)-P'(\xi))-(\delta_2-i\delta_3)(\bar{D}(\xi)-\bar{P}(\xi)) \\ &\quad +\frac{3(\delta_3-i\delta_2)(D'[i(2a)^{-1}]-P'[i(2a)^{-1}])}{4a(1+2ia\xi)}+\frac{(\delta_2+i\delta_3)D[i(2a)^{-1}]D'[i(2a)^{-1}]}{1+2ia\xi}, \end{aligned}$$

$\xi \in \Omega_1$; (20)

$$\begin{aligned} \frac{\kappa+1}{2\mu}\varphi_2(\xi) &= -\delta_1\omega(\xi)-(\delta_2+i\delta_3)P(\xi)-(\delta_2-i\delta_3)\frac{\omega(\xi)}{\bar{\omega}'(\xi)}(\bar{D}'(\xi)-\bar{P}'(\xi)) \\ &\quad +2\delta_1(\bar{D}(\xi)-\bar{P}(\xi))+(\delta_2-i\delta_3)\left(\frac{\bar{D}(\xi)\bar{D}'(\xi)}{\bar{\omega}'(\xi)}-\bar{Q}(\xi)\right) \\ &\quad -\frac{3(\delta_3+i\delta_2)(\overline{D'[i(2a)^{-1}]}-\overline{P'[i(2a)^{-1}]})}{4a(1-2ia\xi)}-\frac{(\delta_2-i\delta_3)\overline{D[i(2a)^{-1}]D'[i(2a)^{-1}]}}{1-2ia\xi}, \\ \frac{\kappa+1}{2\mu}\psi_2(\xi) &= -\frac{\kappa+1}{2\mu}\frac{\bar{\omega}(\xi)\varphi_2'(\xi)}{\omega'(\xi)}+(\delta_2-i\delta_3)\omega(\xi)+2\delta_1P(\xi)+(\delta_2+i\delta_3)Q(\xi) \\ &\quad -\delta_1\bar{\omega}(\xi)-(\delta_2+i\delta_3)\frac{\bar{\omega}(\xi)P'(\xi)}{\omega'(\xi)}-(\delta_2-i\delta_3)(\bar{D}(\xi)-\bar{P}(\xi)) \\ &\quad +\frac{3(\delta_3-i\delta_2)(D'[i(2a)^{-1}]-P'[i(2a)^{-1}])}{4a(1+2ia\xi)}+\frac{(\delta_2+i\delta_3)D[i(2a)^{-1}]D'[i(2a)^{-1}]}{1+2ia\xi}, \end{aligned}$$

$\xi \in \Omega_2$; (21)

For a thermal inclusion ($\varepsilon_{11}^* = \varepsilon_{22}^*$, $\varepsilon_{12}^* = 0$ or $\delta_2 = \delta_3 = 0$; see [Ru 1999]), Equations (20) and (21) simplify to

$$\begin{aligned} \frac{\kappa + 1}{2\mu} \varphi_1(\xi) &= 2\delta_1 (\bar{D}(\xi) - \bar{P}(\xi)), \\ \frac{\kappa + 1}{2\mu} \psi_1(\xi) &= -2\delta_1 (D(\xi) - P(\xi)) - 2\delta_1 \frac{\bar{\omega}(\xi)}{\omega'(\xi)} (\bar{D}'(\xi) - \bar{P}'(\xi)), \quad \xi \in \Omega_1; \end{aligned} \quad (22)$$

$$\begin{aligned} \frac{\kappa + 1}{2\mu} \varphi_2(\xi) &= -\delta_1 \omega(\xi) + 2\delta_1 (\bar{D}(\xi) - \bar{P}(\xi)), \\ \frac{\kappa + 1}{2\mu} \psi_2(\xi) &= 2\delta_1 P(\xi) - 2\delta_1 \frac{\bar{\omega}(\xi)}{\omega'(\xi)} (\bar{D}'(\xi) - \bar{P}'(\xi)), \quad \xi \in \Omega_1. \end{aligned} \quad (23)$$

When $a = 0$ (straight boundary), the results in (20)–(23) recover those by [Ru 1999] for a half-plane.

3.2. Anti-plane eigenstrains (ε_{31}^* , ε_{32}^*). In this case, the boundary value problem in the ξ -plane takes the following form:

$$f_1(\xi) + \overline{f_1(\xi)} = f_2(\xi) + \overline{f_2(\xi)}, \quad (24a)$$

$$f_1(\xi) - \overline{f_1(\xi)} = f_2(\xi) - \overline{f_2(\xi)} + 2(\varepsilon_{32}^* + i\varepsilon_{31}^*)\omega(\xi) - 2(\varepsilon_{32}^* - i\varepsilon_{31}^*)\overline{\omega(\xi)}, \quad \xi \in L;$$

$$f_1(\xi) + \overline{f_1(\xi)} = 0, \quad \text{Im } \xi = 0^-; \quad (24b)$$

$$f_1(\xi) \cong O(1), \quad |\xi| \rightarrow \infty. \quad (24c)$$

The two interface conditions in (24a) can be rewritten as

$$f_1(\xi) + (\varepsilon_{32}^* - i\varepsilon_{31}^*)(D(\xi) - P(\xi)) = f_2(\xi) + (\varepsilon_{32}^* + i\varepsilon_{31}^*)\omega(\xi) - (\varepsilon_{32}^* - i\varepsilon_{31}^*)P(\xi), \quad \xi \in L, \quad (25)$$

where $D(\xi)$ and $P(\xi)$ have been defined in (12) and (13).

We now introduce the auxiliary function $h(\xi)$ defined by

$$h(\xi) = \begin{cases} f_1(\xi) + (\varepsilon_{32}^* - i\varepsilon_{31}^*)(D(\xi) - P(\xi)), & \xi \in \Omega_1; \\ f_2(\xi) + (\varepsilon_{32}^* + i\varepsilon_{31}^*)\omega(\xi) - (\varepsilon_{32}^* - i\varepsilon_{31}^*)P(\xi), & \xi \in \Omega_2. \end{cases} \quad (26)$$

It is seen from the above definition and (25) that $h(\xi)$ is continuous across L and then analytic in the lower half ξ -plane including the point at infinity. The traction-free condition in (24b) can be expressed in terms of $h(\xi)$ as follows:

$$h^-(\xi) - (\varepsilon_{32}^* + i\varepsilon_{31}^*)(\bar{D}(\xi) - \bar{P}(\xi)) = -\bar{h}^+(\xi) + (\varepsilon_{32}^* - i\varepsilon_{31}^*)(D(\xi) - P(\xi)), \quad \text{Im } \xi = 0. \quad (27)$$

The left and right sides of (27) are again analytic in the lower and upper half-planes, respectively, including the point at infinity. As above, by applying Liouville's theorem, the left and right sides of (27) should be identically zero. Thus, we arrive at the following expression for $h(\xi)$:

$$h(\xi) = (\varepsilon_{32}^* + i\varepsilon_{31}^*)[\bar{D}(\xi) - \bar{P}(\xi)], \quad \text{Im } \xi \leq 0. \quad (28)$$

It then follows from (26) and (28) that

$$\begin{aligned} f_1(\xi) &= (\varepsilon_{32}^* + i\varepsilon_{31}^*)[\bar{D}(\xi) - \bar{P}(\xi)] - (\varepsilon_{32}^* - i\varepsilon_{31}^*)[D(\xi) - P(\xi)], \quad \xi \in \Omega_1; \\ f_2(\xi) &= (\varepsilon_{32}^* + i\varepsilon_{31}^*)[\bar{D}(\xi) - \bar{P}(\xi)] - (\varepsilon_{32}^* + i\varepsilon_{31}^*)\omega(\xi) + (\varepsilon_{32}^* - i\varepsilon_{31}^*)P(\xi), \quad \xi \in \Omega_2; \end{aligned} \quad (29)$$

It is clear that when the subdomain undergoes only anti-plane eigenstrains, the expressions for the two analytic functions $f_1(\xi)$ and $f_2(\xi)$ are relatively simple.

4. Examples

In this section, several examples will be presented to demonstrate the general solutions obtained in the previous section.

4.1. $\xi \in L$ is a circle. When $\xi \in L$ is a circle described by

$$|\xi - \xi_0| = R, \quad \xi \in L, \quad (30)$$

the explicit expressions for $D(\xi)$, $D(\xi)D'(\xi)/\omega'(\xi)$, $P(\xi)$ and $Q(\xi)$ are given by

$$\begin{aligned} D(\xi) &= \frac{R^2(1 - 2ia\bar{\xi}_0)}{\xi - \xi_0} - \frac{iaR^4}{(\xi - \xi_0)^2} + \bar{\xi}_0 - ia\bar{\xi}_0^2, \\ \frac{D(\xi)D'(\xi)}{\omega'(\xi)} &= \frac{1}{1 + 2ia\xi} \left[-\frac{R^2(\bar{\xi}_0 - ia\bar{\xi}_0^2)(1 - 2ia\bar{\xi}_0)}{(\xi - \xi_0)^2} + \frac{R^2(-1 + 6ia\bar{\xi}_0 + 6a^2\bar{\xi}_0^2)}{(\xi - \xi_0)^3} \right. \\ &\quad \left. + \frac{3iaR^6(1 - 2ia\bar{\xi}_0)}{(\xi - \xi_0)^4} + \frac{2a^2R^8}{(\xi - \xi_0)^5} \right], \end{aligned} \quad (31)$$

$$P(\xi) = \bar{\xi}_0 - ia\bar{\xi}_0^2, \quad Q(\xi) = 0.$$

By substituting the above expressions into (20), (21) and (29), we arrive at the six analytic functions $\varphi_j(\xi)$, $\psi_j(\xi)$, $f_j(\xi)$, $j = 1, 2$. We emphasize that although $\xi \in L$ is a circle, $z \in \Gamma$ is of irregular shape. For a thermal inclusion, the hoop stress along the parabola and the average mean stress within the inclusion are given explicitly by

$$\sigma_{tt} = -\frac{16\mu\delta_1}{\kappa + 1} \operatorname{Re} \left\{ \frac{1}{1 + 2iax_1} \left[\frac{R^2(1 + 2ia\xi_0)}{(x_1 - \bar{\xi}_0)^2} + \frac{2iaR^4}{(x_1 - \bar{\xi}_0)^3} \right] \right\} \quad \text{on } x_2 = ax_1^2, \quad (32)$$

$$\langle \sigma_{11} + \sigma_{22} \rangle = \frac{4\mu\delta_1}{\kappa + 1} \left[\frac{R^2}{(\operatorname{Im} \xi_0)^2} + \frac{aR^4}{(\operatorname{Im} \xi_0)^3} \frac{1 - 2a \operatorname{Im} \xi_0}{|1 + 2ia\xi_0|^2} - 2 \right], \quad (33)$$

where $\langle \cdot \rangle$ denotes the average. Although the thermal inclusion is of irregular shape, an analytical expression for the average mean stress inside the inclusion can be derived in view of the fact that $\xi \in \Omega_2$ is circular. In the following numerical studies of (32) and (33) (Figures 3–6), it is assumed that $\delta_1 > 0$.

Figures 3 and 4 illustrate the hoop stress distributions along the parabola for different values of $a\xi_0$ with $aR = 1$. In Figure 3, the center of the circle $\xi \in L$ lies on the negative imaginary axis (i.e., $\operatorname{Re} \xi_0 = 0$); whilst in Figure 4, the circle $\xi \in L$ is just touching the real axis (i.e., $\operatorname{Im} \xi_0 = -R$). It is observed from Figure 3 that: (i) the hoop stress is an even function of x_1 , which is intuitively consistent; (ii) the magnitude of the hoop stress reduces as the center of the circle $\xi \in L$ moves further away from the real axis in the ξ -plane; (iii) the hoop stress is tensile ($\sigma_{tt} > 0$) when $a|x_1|$ is sufficiently small, but

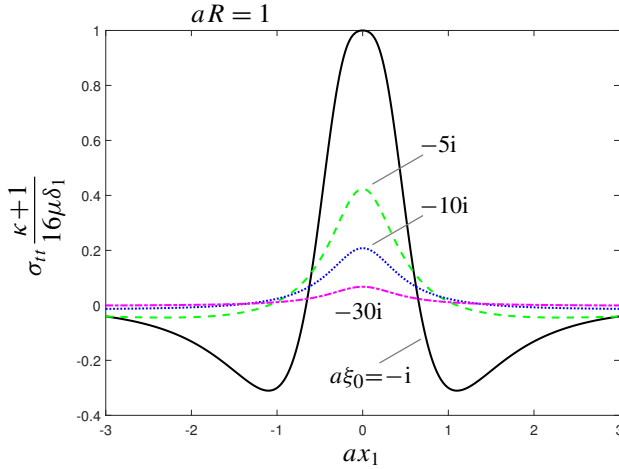


Figure 3. The hoop stress distributions along the parabola for $a\xi_0$ taking the values $-i$, $-5i$, $-10i$, $-30i$, with $aR = 1$ and $\text{Re } \xi_0 = 0$.

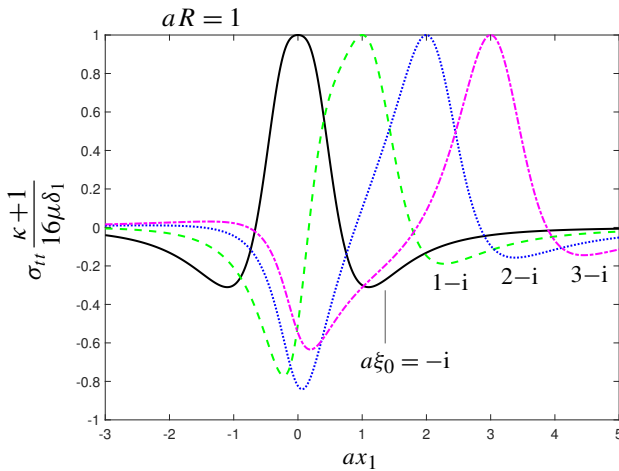


Figure 4. The hoop stress distributions along the parabola for $a\xi_0$ taking the values $-i$, $1 - i$, $2 - i$, and $3 - i$, with $aR = 1$ and $\text{Im } \xi_0 = -R$.

compressive ($\sigma_{tt} < 0$) when $a|x_1|$ becomes sufficiently large; (iv) the maximum value of the hoop stress:

$$\max\{\sigma_{tt}\} = \frac{16\mu\delta_1}{\kappa + 1} \frac{(aR)^2[|a\xi_0| + 2|a\xi_0|^2 - 2(aR)^2]}{|a\xi_0|^3} > 0, \tag{34}$$

occurs at $x_1 = 0$ for a fixed value of $a\xi_0$. It is observed from **Figure 4** that: (i) when the center of the circle is not on the imaginary axis, the hoop stress is no longer an even function of x_1 ; (ii) the maximum value of the hoop stress $\max\{\sigma_{tt}\} = 16\mu\delta_1/(\kappa + 1)$ occurs at $x_1 = \text{Re } \xi_0$ for a fixed value of $a\xi_0$; (iii) the magnitude of the compressive hoop stress is considerable when $a \text{Re } \xi_0 = 1 \sim 2$.

Figure 5 plots the average mean stress within the inclusion as a function of $a \text{Im } \xi_0$ and aR with $\text{Re } \xi_0 = 0$ (the center of the circle $\xi \in L$ lies on the negative imaginary axis). It is seen from **Figure 5** that:

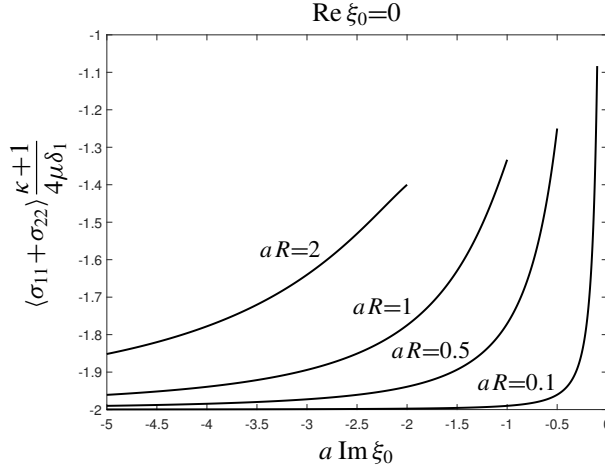


Figure 5. The average mean stress within the inclusion as a function of $a \operatorname{Im} \xi_0$ and aR with $\operatorname{Re} \xi_0 = 0$.

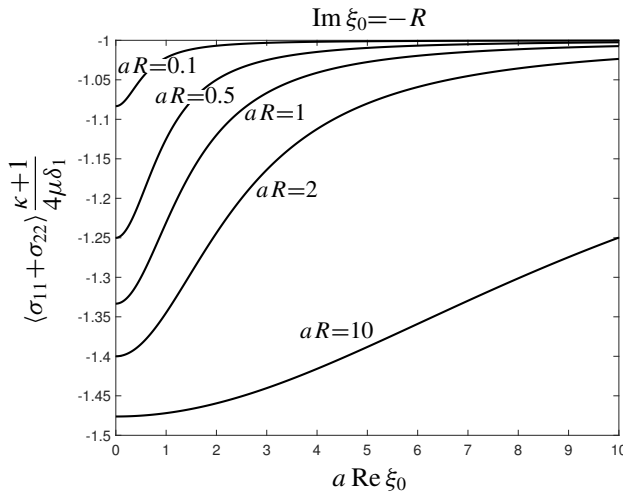


Figure 6. The average mean stress within the inclusion as a function of $a \operatorname{Re} \xi_0$ and aR with $\operatorname{Im} \xi_0 = -R$.

(i) $\langle \sigma_{11} + \sigma_{22} \rangle$ is an increasing function of both $a \operatorname{Im} \xi_0$ and aR ; (ii) $\langle \sigma_{11} + \sigma_{22} \rangle$ is always negative and reaches its maximum when $\xi_0 = -iR$; (iii) as $a \operatorname{Im} \xi_0 \rightarrow -\infty$ or $aR \rightarrow 0$, $\langle \sigma_{11} + \sigma_{22} \rangle \cong -8\mu\delta_1/(\kappa + 1)$, which is simply the value of a circular thermal inclusion in a homogeneous plane [Ru 1999]. Figure 6 plots the average mean stress within the inclusion as a function of $a \operatorname{Re} \xi_0$ and aR with $\operatorname{Im} \xi_0 = -R$ (the inclusion just touches the parabola). It is seen from Figure 6 that: (i) $\langle \sigma_{11} + \sigma_{22} \rangle$ is an increasing function of $a \operatorname{Re} \xi_0$ and a decreasing function of aR ; (ii) $\langle \sigma_{11} + \sigma_{22} \rangle$ is always negative, and

$$\min\{\langle \sigma_{11} + \sigma_{22} \rangle\} = -\frac{4\mu\delta_1}{\kappa + 1} \frac{1 + 3aR}{1 + 2aR} \geq -\frac{6\mu\delta_1}{\kappa + 1}, \tag{35}$$

occurs at $\operatorname{Re} \xi_0 = 0$; (iii) $\langle \sigma_{11} + \sigma_{22} \rangle \cong -4\mu\delta_1/(\kappa + 1)$ as $a \operatorname{Re} \xi_0 \rightarrow \infty$ or $aR \rightarrow 0$.

4.2. A thermal inclusion with $\xi \in L$ describing an ellipse. We consider a thermal inclusion. In addition, $\xi \in L$ is an ellipse described by

$$\xi = w(\eta) = R\left(\eta + \frac{m}{\eta}\right) + \xi_0, \quad R > 0, \quad 0 < |m| < 1, \quad |\eta| = 1, \quad (36)$$

in which m and ξ_0 are complex numbers.

In this case, $D(\xi)$, $P(\xi)$ and $D(\xi) - P(\xi)$ are determined to be

$$\begin{aligned} D(\xi) &= (\bar{m} - m^{-1})[1 - 2ia\bar{\xi}_0 - ia(\bar{m} + m^{-1})(\xi - \xi_0)] \left[\frac{\xi - \xi_0}{2} + \left(\frac{(\xi - \xi_0)^2}{4} - mR^2 \right)^{1/2} \right] \\ &\quad + \bar{\xi}_0 + ia[R^2m^{-1}(1 - |m|^2)^2 - \bar{\xi}_0^2] + m^{-1}(\xi - \xi_0)[1 - 2ia\bar{\xi}_0 - iam^{-1}(\xi - \xi_0)], \\ P(\xi) &= -iam\bar{m}^2\xi^2 + \bar{m}[1 - 2ia(\bar{\xi}_0 - \bar{m}\xi_0)]\xi + \bar{\xi}_0 - \bar{m}\xi_0 + ia[2R^2\bar{m}(|m|^2 - 1) - (\bar{\xi}_0 - \bar{m}\xi_0)^2], \\ D(\xi) - P(\xi) &= (\bar{m} - m^{-1})[1 - 2ia\bar{\xi}_0 - ia(\bar{m} + m^{-1})(\xi - \xi_0)] \left[\left(\frac{(\xi - \xi_0)^2}{4} - mR^2 \right)^{1/2} - \frac{\xi - \xi_0}{2} \right] \\ &\quad - iamR^2(\bar{m}^2 - m^{-2}). \end{aligned} \quad (37)$$

By substituting the above into (22) and (23), we arrive at the two pairs of analytic functions $\varphi_j(\xi)$, $\psi_j(\xi)$, $j = 1, 2$. We emphasize that although $\xi \in L$ is an ellipse (see Figure 2), $z \in \Gamma$ is non-elliptical (see Figure 1). The explicit expressions for the hoop stress along the parabola and the mean stress within the thermal inclusion are finally found to be

$$\begin{aligned} \sigma_{tt} &= \frac{8\mu\delta_1}{\kappa + 1} \operatorname{Re} \left\{ \frac{(m - \bar{m}^{-1})(1 + 2ia\xi_0)}{1 + 2iax_1} \left[\frac{x_1 - \bar{\xi}_0}{\sqrt{(x_1 - \bar{\xi}_0)^2 - 4\bar{m}R^2}} - 1 \right] \right\} \\ &\quad - \frac{32\mu\delta_1aR^2}{\kappa + 1} \operatorname{Im} \left\{ \frac{\bar{m}(m^2 - \bar{m}^{-2})}{1 + 2iax_1} \left[\frac{1}{\sqrt{(x_1 - \bar{\xi}_0)^2 - 4\bar{m}R^2}} - \frac{2}{x_1 - \bar{\xi}_0 + \sqrt{(x_1 - \bar{\xi}_0)^2 - 4\bar{m}R^2}} \right] \right\}, \\ &\text{on } x_2 = ax_1^2, \end{aligned} \quad (38)$$

$$\begin{aligned} \sigma_{11} + \sigma_{22} &= -\frac{8\mu\delta_1}{\kappa + 1} + \frac{8\mu\delta_1}{\kappa + 1} \operatorname{Re} \left\{ \frac{(m - \bar{m}^{-1})(1 + 2ia\xi_0)}{1 + 2ia\xi} \left[\frac{\xi - \bar{\xi}_0}{\sqrt{(\xi - \bar{\xi}_0)^2 - 4\bar{m}R^2}} - 1 \right] \right\} \\ &\quad - \frac{32\mu\delta_1aR^2}{\kappa + 1} \operatorname{Im} \left\{ \frac{\bar{m}(m^2 - \bar{m}^{-2})}{1 + 2ia\xi} \left[\frac{1}{\sqrt{(\xi - \bar{\xi}_0)^2 - 4\bar{m}R^2}} - \frac{2}{\xi - \bar{\xi}_0 + \sqrt{(\xi - \bar{\xi}_0)^2 - 4\bar{m}R^2}} \right] \right\}, \\ &\xi \in \Omega_2. \end{aligned} \quad (39)$$

5. Conclusions

A novel procedure is presented to derive analytic solutions for the Eshelby's problem of an inclusion of arbitrary shape in an isotropic plane with parabolic boundary. First, a conformal mapping function, which maps the region with the parabolic boundary in the physical plane onto the lower half of the image ξ -plane, is introduced in (8). In the ξ -plane, an auxiliary function $D(\xi)$ is then constructed via (12). The technique of analytic continuation is further applied with this auxiliary function to derive the analytic functions $\varphi_j(\xi)$, $\psi_j(\xi)$, $f_j(\xi)$, $j = 1, 2$. In contrast to the method used by [Ru 1999] in the analysis of

the corresponding “straight boundary problems”, our analysis remains in the ξ -plane where the parabola is conveniently mapped onto the real axis.

Acknowledgements

This work is supported by the National Natural Science Foundation of China (Grant No. 11272121) and through a Discovery Grant from the Natural Sciences and Engineering Research Council of Canada (RGPIN–2017-03716115112).

References

- [England 1971] A. H. England, *Complex variable methods in elasticity*, Wiley, London, 1971.
- [Muskhelishvili 1953] N. I. Muskhelishvili, *Some basic problems of the mathematical theory of elasticity*, Noordhoff, Groningen, 1953.
- [Ru 1999] C. Q. Ru, “Analytic solution for Eshelby’s problem of an inclusion of arbitrary shape in a plane or half-plane”, *J. Appl. Mech. (ASME)* **66** (1999), 315–322.
- [Ru 2000] C. Q. Ru, “Eshelby’s problem for two-dimensional piezoelectric inclusions of arbitrary shape”, *Proc. Roy. Soc. London A* **456** (2000), 1051–1068.
- [Ru 2003] C. Q. Ru, “Eshelby inclusion of arbitrary shape in an anisotropic plane/half-plane”, *Acta Mech.* **160** (2003), 219–234.
- [Savin 1961] G. N. Savin, *Stress concentration around holes*, Pergamon Press, London, 1961.
- [Ting 1996] T. C. T. Ting, *Anisotropic elasticity: theory and applications*, Oxford University Press, New York, 1996.
- [Ting et al. 2001] T. C. T. Ting, Y. Hu, and H. O. K. Kirchner, “Anisotropic elastic materials with a parabolic or hyperbolic boundary: a classical problem revisited”, *J. Appl. Mech. (ASME)* **68** (2001), 537–542.
- [Wang 2004] X. Wang, “Eshelby’s problem of an inclusion of arbitrary shape in a decagonal quasicrystalline plane or half-plane”, *Int. J. Eng. Sci.* **42** (2004), 1911–1930.
- [Wang and Schiavone 2015] X. Wang and P. Schiavone, “Eshelby’s problem for infinite, semi-infinite and two bonded semi-infinite laminated anisotropic thin plates”, *Arch. Appl. Mech.* **85** (2015), 573–585.
- [Wang and Zhou 2014] X. Wang and K. Zhou, “An inclusion of arbitrary shape in an infinite or semi-infinite isotropic multi-layered plate”, *Int. J. Appl. Mech.* **6** (2014), art. id 1450001 (21 pages).
- [Zhou et al. 2013] K. Zhou, H. J. Hoh, X. Wang, L. M. Keer, J. H. L. Pang, B. Song, and Q. J. Wang, “A review of recent works on inclusions”, *Mech. Mater.* **60** (2013), 144–158.

Received 2 Nov 2017. Revised 29 Nov 2017. Accepted 5 Dec 2017.

XU WANG: xuwang@ecust.edu.cn

School of Mechanical and Power Engineering, East China University of Science and Technology, 130 Meilong Road, Shanghai, 200237, China

LIANG CHEN: liangchen5962@mail.ecust.edu.cn

School of Mechanical and Power Engineering, East China University of Science and Technology, 130 Meilong Road, Shanghai, 200237, China

PETER SCHIAVONE: p.schiavone@ualberta.ca

Department of Mechanical Engineering, University of Alberta, 10-203 Donadeo Innovation Center for Engineering, 9211-116 Street NW, Edmonton AB T6G 1H9, Canada

BURMISTER'S PROBLEM EXTENDED TO A MICROSTRUCTURED LAYER

THANASIS ZISIS

The problem of calculating the displacement and stress field in a layered elastic system loaded on its surface by a certain pressure distribution often arises in engineering analysis and design, in a number of scientific areas ranging from mechanical engineering to soil mechanics and materials science. The solution of such a problem is very important and was first introduced by Biot (1935) but later it was Burmister who presented a complete solution for the stresses and displacements in a general two layer elastic system in which the lower layer is not necessarily rigid (Burmister 1943; Burmister et al. 1944). His results found great application in the field of civil engineering but nowadays can be extended to the technology of barrier, multilayered and/or functionally coatings. Furthermore, due to the ease of manufacturing and assembly, coatings with micro- or even nano-thickness are pursued by manufacturers as hybrid materials for multifunctional devices but as manufacturing scales reduce progressively, the material microstructure itself can play an important role and size effects can be dominant upon the macroscopic mechanical response of the layer/coating. In this study we focus on the loading of a microstructural layer by a normal point load and we present the corresponding Green's functions by extending the solutions suggested by Burmister et al. in order to introduce into the generated displacement and stress fields the effect of the microstructural characteristics of the layer. In order to incorporate the layer material microstructural characteristics we use an effective generalized continuum theory, that is the couple-stress elasticity, in which the material microstructure is introduced constitutively through a length scale. The presented results suggest deviation from those suggested by Burmister et al. in the context of *classical* elasticity for a *layer of finite thickness* as well as from those suggested by Gourgiotis and Zisis (2016) in the context of couple stress elasticity for a *half-plane*.

1. Introduction

Contact situations occur in a multitude of engineering applications ranging from mechanical and civil engineering to materials science. Many structures are founded in reinforced concrete footings or pads buried at relatively shallow depths beneath the ground surface and large scale contacts take place between the footings and the deformable ground. On the other hand, small scale contacts appear in nano-indentation tests in the area of mechanical engineering and/or material science. In an ideal contact situation between two bodies, either within the context of civil engineering where the footing essentially acts as an indenter that lies upon a deformable body (i.e. the ground) or within the spirit of an indentation experiment where the flat surface of the underlying material is mounted perpendicular to the tip of the indenter, the indenter touches the surface of the material and penetration is performed. The details of such penetration may be interpreted in terms of the stress distribution below the indenter and subsequently the stress distribution within the bodies in contact, the surface displacements, the contact site, etc. Such analysis is crucial

Keywords: micromechanics, couple-stress elasticity, Green's functions, microstructured layers, coatings.

for design purposes in geotechnical and footing engineering, or in the case of material characterization through indentation tests.

Coatings with thickness ranging from micro- to nanometers are currently manufactured as materials for multifunctional devices. Such applications of coatings range from insulators to thermal and corrosion barrier systems. The mechanical properties of such coatings and the observed failure mechanisms are of great interest for design purposes and a very efficient technique in order to extract such mechanical characteristics is the micro- and nano-indentation experiment. Furthermore, material systems that comprise of several layers are usually found in the field of soil mechanics and from structural considerations the problem of calculating the stress and displacement fields within the material system as well as at the layer interface is of great importance.

It is well known that under loading conditions, size effects can be dominant especially when the characteristic lengths of the problems are comparable to the characteristic material length scale which is associated to the materials inherent microstructure. In fact, the macroscopical behavior of most microstructured materials with nonhomogeneous microstructure, like ceramics, composites, cellular materials, foams, masonry, bone tissues, glassy and semicrystalline polymers, is strongly influenced by the microstructural characteristic lengths, especially in the presence of large stress (or strain) gradients [Maranganti and Sharma 2007].

The generalized continuum theories smear-out the material microstructure and enrich the classical continuum with additional material characteristic length scales extending, thus, the range of applicability of the “continuum” concept in an effort to bridge the gap between classical continuum theories and atomic-lattice theories. This approach is very effective since it can be incorporated efficiently into large computations but of course lacks the detailed description of a discrete representation and treats the microstructural length in an average sense [Muki and Sternberg 1965; Poole et al. 1996; Begley and Hutchinson 1998; Nix and Gao 1998; Shu and Fleck 1998; Wei and Hutchinson 2003; Zisis et al. 2014; Zisis 2017; Gourgiotis et al. 2018].

The physical relevance of the material length scale as introduced through generalized continuum theories has been the subject of numerous theoretical and experimental studies. Chen et al. [1998], for example, developed a continuum model for cellular materials and concluded that the continuum description of these materials obeys a gradient elasticity theory of the couple-stress type. In the latter study, the intrinsic material length was identified with the cell size. Tekoglu and Onck [2008] compared the analytical results of various gradient type generalized continuum theories with the computational results of discrete models through a range of basic boundary value problems based on Voronoi representations of cellular microstructures. The analysis they performed, strictly within the elastic regime, assessed the capabilities of generalized continuum theories in capturing size effects in cellular solids and connected the cell size with the microstructural length-scale. Two recent studies [Bigoni and Drugan 2007; Bacca et al. 2013] provide an account of the determination of the couple-stress moduli via homogenization of heterogeneous materials. Finally, Shodja et al. [2013], using ab initio DFT calculations, evaluated the characteristic material lengths of the gradient elasticity theory for several fcc and bcc metal crystals.

One effective generalized continuum theory has proved to be that of couple-stress elasticity, also known as Cosserat theory with constrained rotations [Mindlin and Tiersten 1962; Toupin 1964]. In the context of couple-stress elasticity, the strain-energy density and the resulting constitutive relations involve, besides the usual infinitesimal strains, certain strain gradients known as the rotation gradients.

The generalized stress-strain relations for the isotropic case include, in addition to the conventional pair of elastic constants, two new elastic constants, one of which is expressible in terms of a material parameter ℓ that has dimension of [length]. The presence of this length parameter, in turn, implies that the modified theory encompasses the analytical possibility of size effects, which are absent in the classical theory.

The simplest case of a layered system is that of an elastic layer bonded on a rigid base. For a multitude of layered systems, ranging from materials science to soil mechanics, the bonding condition sufficiently describes the interface characteristics. This problem, in the context of classical elasticity, has received attention from several investigators. Marguerre [1931] obtained a solution for the stresses in the layer under plane strain conditions, while Biot [1935] examined both the case of plain strain and axial symmetry with restriction to the calculation of the normal stresses. Biot's work was extended by Pickett [1938], who presented the complete stress and displacement fields under both plane strain and axisymmetric conditions.

A general solution in terms of a two-layer elastic system in which the lower layer is not necessarily rigid was given in [Burmister 1943; Burmister et al. 1944; Burmister 1945a; 1945b]. In [Burmister 1956] this was extended to a complete mathematical solution regarding the stress and displacement fields in a layer bonded on a rigid substrate loaded by a point load. This now classical problem, bearing Burmister's name, finds applications in mechanical and civil engineering as well as materials science. A number of works have followed since, that either extended the classical Burmister's problem to different geometries and different loading conditions but all in the context of classical elasticity [Schiffman 1957; Davis and Taylor 1961; Davis and Poulos 1963; Poulos 1967].

Our purpose is to study the macroscopic response of a bonded layer with microstructural characteristics. For this reason in the present work, we extend the classical work of Burmister and we examine the mechanics under which the presence of a rigid substrate, the finite thickness of the deformable layer as well as the material microstructural characteristics, influence the displacement and stress fields.

The problem under investigation is solved in the frame of couple stress theory and it is anticipated that our results will be essentially intermediate to those of [Burmister 1956] for the case of a layer in the context of classical elasticity and those of [Gourgiotis and Zisis 2016] for the half-plane in the frame of couple-stress theory.

2. Basic equations of couple-stress elasticity in plane-strain

In this section, we summarize the main features of the linearized couple-stress theory of homogeneous and isotropic elastic solids [Mindlin and Tiersten 1962; Koiter 1964a; Koiter 1964b]. An exposition of the theory under plane-strain conditions was given in [Muki and Sternberg 1965], and more recently by [Gourgiotis and Piccolroaz 2014] in the elastodynamic case including micro-inertial effects.

For a body that occupies a domain in the (x, y) -plane under conditions of plane-strain, the equations of equilibrium in the absence of body forces and body moments reduce to

$$\frac{\partial \sigma_{xx}}{\partial x} + \frac{\partial \sigma_{yx}}{\partial y} = 0, \quad \frac{\partial \sigma_{xy}}{\partial x} + \frac{\partial \sigma_{yy}}{\partial y} = 0, \quad \sigma_{xy} - \sigma_{yx} + \frac{\partial m_{xz}}{\partial x} + \frac{\partial m_{yz}}{\partial y} = 0, \quad (1)$$

where $(\sigma_{xx}, \sigma_{xy}, \sigma_{yx}, \sigma_{yy})$ and (m_{xz}, m_{yz}) are the nonvanishing components of the (asymmetric) stress and couple-stress tensors, respectively. The complete solution of (1) admits the following representation in terms of two sufficiently smooth stress functions $\Phi \equiv \Phi(x, y)$ and $\Psi \equiv \Psi(x, y)$ [Mindlin 1963]:

$$\begin{aligned}\sigma_{xx} &= \frac{\partial^2 \Phi}{\partial y^2} - \frac{\partial^2 \Psi}{\partial x \partial y}, & \sigma_{yy} &= \frac{\partial^2 \Phi}{\partial x^2} + \frac{\partial^2 \Psi}{\partial x \partial y}, \\ \sigma_{xy} &= -\frac{\partial^2 \Phi}{\partial x \partial y} - \frac{\partial^2 \Psi}{\partial y^2}, & \sigma_{yx} &= -\frac{\partial^2 \Phi}{\partial x \partial y} + \frac{\partial^2 \Psi}{\partial x^2},\end{aligned}\quad (2)$$

and

$$m_{xz} = \frac{\partial \Psi}{\partial x}, \quad m_{yz} = \frac{\partial \Psi}{\partial y}.\quad (3)$$

Accordingly, the displacement field assumes the following general form:

$$u_x \equiv u_x(x, y), \quad u_y \equiv u_y(x, y), \quad u_z \equiv 0.\quad (4)$$

The governing kinematic relations in the framework of the geometrically linear theory then become:

$$\varepsilon_{xx} = \frac{\partial u_x}{\partial x}, \quad \varepsilon_{yy} = \frac{\partial u_y}{\partial y}, \quad \varepsilon_{xy} = \varepsilon_{yx} = \frac{1}{2} \left(\frac{\partial u_y}{\partial x} + \frac{\partial u_x}{\partial y} \right),\quad (5)$$

$$\omega_z = \frac{1}{2} \left(\frac{\partial u_y}{\partial x} - \frac{\partial u_x}{\partial y} \right), \quad \kappa_{xz} = \frac{\partial \omega_z}{\partial x}, \quad \kappa_{yz} = \frac{\partial \omega_z}{\partial y},\quad (6)$$

where $\boldsymbol{\varepsilon}$ is the usual strain tensor, ω_z is the rotation, and $(\kappa_{xz}, \kappa_{yz})$ are the nonvanishing components of the curvature tensor (i.e. the gradient of rotation) expressed in dimensions of $[\text{length}]^{-1}$. For a homogeneous and isotropic couple-stress material the constitutive equations furnish:

$$\begin{aligned}\varepsilon_{xx} &= (2\mu)^{-1} [\sigma_{xx} - \nu(\sigma_{xx} + \sigma_{yy})], & \varepsilon_{yy} &= (2\mu)^{-1} [\sigma_{yy} - \nu(\sigma_{xx} + \sigma_{yy})], \\ \varepsilon_{xy} &= (4\mu)^{-1} (\sigma_{xy} + \sigma_{yx}),\end{aligned}\quad (7)$$

and

$$\kappa_{xz} = (4\mu\ell^2)^{-1} m_{xz}, \quad \kappa_{yz} = (4\mu\ell^2)^{-1} m_{yz},\quad (8)$$

where μ , ν , and ℓ stand for the shear modulus, Poisson's ratio, and characteristic material length of couple-stress theory, respectively [Mindlin and Tiersten 1962].

Further, substitution of (2) and (3) into (7) and (8) results in the compatibility equations for the Mindlin's stress functions:

$$\frac{\partial}{\partial x} (\Psi - \ell^2 \nabla^2 \Psi) = -2(1 - \nu) \ell^2 \nabla^2 \left(\frac{\partial \Phi}{\partial y} \right),\quad (9)$$

$$\frac{\partial}{\partial y} (\Psi - \ell^2 \nabla^2 \Psi) = 2(1 - \nu) \ell^2 \nabla^2 \left(\frac{\partial \Phi}{\partial x} \right),\quad (10)$$

from which, in turn, we obtain the following uncoupled partial differential equations:

$$\nabla^4 \Phi = 0,\quad (11)$$

$$\nabla^2 \Psi - \ell^2 \nabla^4 \Psi = 0.\quad (12)$$

Note that as the quantities ℓ , $\partial \Psi / \partial x$, and $\partial \Psi / \partial y$ tend to zero, the above representation passes over into the classical Airy's representation.

3. Concentrated load at the surface of a bonded layer with microstructure

The definition of a Green's function can be used mathematically to derive solutions to point load problems, either within the elastic body or on its surface. A multitude of Green's functions within the context of classical elasticity are available in the literature for different surface geometries (see e.g., [Green and Zerna 1968]). In a 2D setting, the problem of determining the stress and displacement fields in an isotropic half-plane subjected to a concentrated line load on its surface is the celebrated Flamant–Boussinesq problem. The Flamant–Boussinesq solution of classical elasticity is discussed among others, e.g., by [Love 1952; Fung 1965; Timoshenko and Goodier 1970], and enjoys important applications mainly in Contact Mechanics and Tribology, since it can be used as a building block for the formulation of complicated contact problems (see e.g. [Johnson 1985; Hills and Nowell 1994; Barber 2010]).

In the context of generalized continuum theories, concentrated load problems have been extensively studied suggesting solutions that significantly depart from the predictions of classical elasticity (see for example the works of [Georgiadis and Anagnostou 2008; Gourgiotis and Zisis 2016; Zisis 2017; Gourgiotis et al. 2018]). Regarding the couple-stress theory, [Muki and Sternberg 1965] were the first to derive the asymptotic fields for the stress field in the Flamant–Boussinesq problem while recently full field solutions were presented by [Gourgiotis and Zisis 2016]. Here, we provide a solution for the concentrated load problem at the surface of a microstructured layer in the context of couple stress theory of elasticity which can accordingly be used as the pertinent Green's function for the formulation of the plane contact problems.

Consider a body occupying the half-plane ($-\infty < x < \infty$, $0 \leq y \leq h$) under plane strain conditions subjected to a normal line load P on its surface (see Figure 1). The point of application of the concentrated load is taken as the origin ($x = y = 0$) of a Cartesian rectangular coordinate system. The intensities of the concentrated loads are expressed in dimensions of [force][length] $^{-1}$.

Accordingly, the boundary conditions along the surface $y = 0$ become:

$$\sigma_{yy}(x, 0) = -P\delta(x), \quad -\infty < x < \infty, \quad (13)$$

$$\sigma_{yx}(x, 0) = 0, \quad -\infty < x < \infty, \quad (14)$$

$$m_{yz}(x, 0) = 0, \quad -\infty < x < \infty, \quad (15)$$

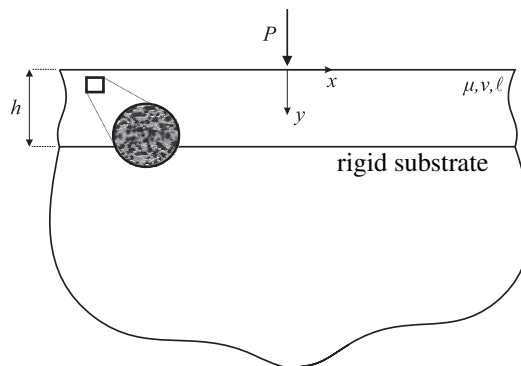


Figure 1. Normal load acting on the surface of an elastic layer of thickness h bonded onto the rigid substrate. This is Burmister's problem (1953) extended to a microstructured layer in the context of couple-stress elasticity.

where $\delta(x)$ is the Dirac delta function. The solution procedure for the case of a tangential load acting on the surface of a half-plane is directly analogous to what will be presented in what follows and is omitted for sake of brevity.

Regarding the boundary conditions at the interface between the microstructured layer and the rigid substrate, we can define two different sets of boundary conditions as follows:

(1) The first set suggests vanishing displacements and rotations as:

$$u_x(x, h) = 0, \quad -\infty < x < \infty, \quad (16)$$

$$u_y(x, h) = 0, \quad -\infty < x < \infty, \quad (17)$$

$$\omega_z(x, h) = 0, \quad -\infty < x < \infty, \quad (18)$$

(2) The second set suggests vanishing displacements and couple stresses m_{yz} as:

$$u_x(x, h) = 0, \quad -\infty < x < \infty, \quad (19)$$

$$u_y(x, h) = 0, \quad -\infty < x < \infty, \quad (20)$$

$$m_{yz}(x, h) = 0, \quad -\infty < x < \infty, \quad (21)$$

Note that the first set of boundary conditions corresponds to an over-constrained version of the classical elasticity solution while the second set of boundary conditions allows for a direct comparison of the current solution with the classical elasticity results.

The problem is attacked with the aid of the Fourier transform on the basis of the stress function formulation summarized earlier. The direct Fourier transform and its inverse are defined by

$$\hat{f}(\xi) = \int_{-\infty}^{\infty} f(x)e^{i\xi x} dx, \quad f(x) = \frac{1}{2\pi} \int_{-\infty}^{\infty} \hat{f}(\xi)e^{-i\xi x} d\xi. \quad (22)$$

The transformation of (11) and (12) through (22) yields the following ODEs for the transformed stress functions:

$$\frac{d^4 \hat{\Phi}}{dy^4} - 2\xi^2 \frac{d^2 \hat{\Phi}}{dy^2} + \xi^4 \hat{\Phi} = 0, \quad (23)$$

$$\ell^2 \frac{d^4 \hat{\Psi}}{dy^4} - (1 + 2\ell^2 \xi^2) \frac{d^2 \hat{\Psi}}{dy^2} + \xi^2 (1 + \ell^2 \xi^2) \hat{\Psi} = 0. \quad (24)$$

The transformed stresses and couple-stresses become

$$\begin{aligned} \hat{\sigma}_{xx} &= \frac{d^2 \hat{\Phi}}{dy^2} + i\xi \frac{d\hat{\Psi}}{dy}, & \hat{\sigma}_{yy} &= -\xi^2 \hat{\Phi} - i\xi \frac{d\hat{\Psi}}{dy}, \\ \hat{\sigma}_{yx} &= i\xi \frac{d\hat{\Phi}}{dy} - \xi^2 \hat{\Psi}, & \hat{\sigma}_{xy} &= i\xi \frac{d\hat{\Phi}}{dy} - \frac{d^2 \hat{\Psi}}{dy^2}, \end{aligned} \quad (25)$$

$$\hat{m}_{xz} = -i\xi \hat{\Psi}, \quad \hat{m}_{yz} = \frac{d\hat{\Psi}}{dy}, \quad (26)$$

whereas the displacements become

$$\begin{aligned} \hat{u}_x &= \frac{1}{2\mu\xi} \left(i(1-\nu) \frac{d^2\hat{\Phi}}{dy^2} - \xi \frac{d\hat{\Psi}}{dy} + i\nu\xi^2\hat{\Phi} \right), \\ \hat{u}_y &= \frac{1}{2\mu\xi^2} \left((1-\nu) \frac{d^3\hat{\Phi}}{dy^3} - (2-\nu)\xi^2 \frac{d\hat{\Phi}}{dy} - i\xi^3\hat{\Psi} \right). \end{aligned} \tag{27}$$

The governing equations (23) and (24) have the following general solution:

$$\hat{\Phi}(\xi, y) = [C_1(\xi) + yC_2(\xi)]e^{-|\xi|y} + [C_3(\xi) + yC_4(\xi)]e^{|\xi|y}, \tag{28}$$

$$\hat{\Psi}(\xi, y) = B_1(\xi)e^{-|\xi|y} + B_2(\xi)e^{-\gamma y} + B_3(\xi)e^{\xi y} + B_4(\xi)e^{\gamma y}, \tag{29}$$

where $\gamma \equiv \gamma(\xi) = (1/\ell^2 + \xi^2)^{1/2}$.

Enforcing the boundary conditions (13)–(15) for the layer surface and (16)–(18) or (19)–(21) for the base of the layer, and the compatibility equations (9) and (10), we obtain a system of eight equations (written in matrix form in Appendix) which are solved for the unknown functions $B_i(\xi)$ and $C_i(\xi)$ with $i = 1, \dots, 4$. Auxiliary conditions are obtained through the compatibility equations as:

$$B_1(\xi) = -4i\ell^2(1-\nu)\xi C_2(\xi), \tag{30}$$

$$B_3(\xi) = -4i\ell^2(1-\nu)\xi C_4(\xi). \tag{31}$$

Upon substitution of the functions $B_i(\xi)$, $C_i(\xi)$ into (27)–(29), and utilizing the fact that $\hat{u}_x(x, \xi)$, $\hat{\omega}_z(x, \xi)$ and $\hat{u}_y(x, \xi)$ are odd, odd and even functions of ξ , respectively, the components of the transformed displacement and rotation field become:

$$u_x(x, y) = \frac{-i}{\pi} \int_0^\infty \hat{u}_x(\xi, y) \sin(\xi x) d\xi, \tag{32}$$

$$u_y(x, y) = \frac{1}{\pi} \int_0^\infty \hat{u}_y(\xi, y) \cos(\xi x) d\xi, \tag{33}$$

$$\omega_z(x, y) = \frac{-i}{\pi} \int_0^\infty \hat{\omega}_z(\xi, y) \sin(\xi x) d\xi, \tag{34}$$

while under similar considerations, the stresses and couple stresses read:

$$\sigma_{xx}(x, y) = \frac{1}{\pi} \int_0^\infty \hat{\sigma}_{xx}(\xi, y) \cos(\xi x) d\xi, \tag{35}$$

$$\sigma_{yy}(x, y) = \frac{1}{\pi} \int_0^\infty \hat{\sigma}_{yy}(\xi, y) \cos(\xi x) d\xi, \tag{36}$$

$$\sigma_{xy}(x, y) = \frac{-i}{\pi} \int_0^\infty \hat{\sigma}_{xy}(\xi, y) \sin(\xi x) d\xi, \tag{37}$$

$$\sigma_{yx}(x, y) = \frac{-i}{\pi} \int_0^\infty \hat{\sigma}_{yx}(\xi, y) \sin(\xi x) d\xi, \tag{38}$$

$$m_{xz}(x, y) = \frac{1}{\pi} \int_0^\infty \hat{m}_{xz}(\xi, y) \cos(\xi x) d\xi, \tag{39}$$

$$m_{yz}(x, y) = \frac{-i}{\pi} \int_0^\infty \hat{m}_{yz}(\xi, y) \sin(\xi x) d\xi. \tag{40}$$

In fact for the same problem, in terms of loading conditions and in the context of couple stress theory, the half-plane solution for the displacement and rotation field reads thus [Gourgiotis and Zisis 2016]:

$$u_x(x, y) = \frac{P}{2\mu\pi} \int_0^\infty \frac{4\ell^2(1-\nu)\xi^2\gamma e^{-\gamma y} + (\gamma(y\xi - 1 + 2\nu) - 4\ell^2(1-\nu)\xi^3)e^{-\xi y}}{\xi(\gamma - 4(1-\nu)\ell^2\xi^2(\xi - \gamma))} \sin(\xi x) d\xi, \quad (41)$$

$$u_y(x, y) = \frac{P}{2\mu\pi} \int_0^\infty \frac{4\ell^2(1-\nu)\xi^3 e^{-\gamma y} + (\gamma(y\xi + 2(1-\nu)) - 4\ell^2(1-\nu)\xi^3)e^{-\xi y}}{\xi(\gamma - 4(1-\nu)\ell^2\xi^2(\xi - \gamma))} \cos(\xi x) d\xi, \quad (42)$$

$$\omega_z(x, y) = \frac{P}{2\mu\pi} \int_0^\infty \frac{e^{-y(\gamma+\xi)}(1-\nu)(e^{y\xi}\ell^2\xi(\gamma-\xi)(\gamma+\xi) - e^{y\gamma}\gamma)}{\gamma - 4\ell^2\gamma(-1+\nu)\xi^2 + 4\ell^2(-1+\nu)\xi^3} \sin(\xi x) d\xi, \quad (43)$$

while the stresses and couple-stresses follow as:

$$\sigma_{xx}(x, y) = \frac{P}{\pi} \int_0^\infty \frac{e^{-y(\gamma+\xi)}(e^{y\gamma}(\gamma - y\gamma\xi + 4\ell^2(1-\nu)\xi^3) - 4e^{y\xi}\ell^2\gamma(1-\nu)\xi^2)}{4\ell^2(1-\nu)\xi^3 - \gamma(1 + 4\ell^2(1-\nu)\xi^2)} \cos(\xi x) d\xi, \quad (44)$$

$$\sigma_{yy}(x, y) = \frac{P}{\pi} \int_0^\infty \frac{e^{-y(\gamma+\xi)}(4e^{y\xi}\ell^2\gamma(1-\nu)\xi^2 + e^{y\gamma}(\gamma + y\gamma\xi - 4\ell^2(1-\nu)\xi^3))}{4\ell^2(1-\nu)\xi^3 - \gamma(1 + 4\ell^2(1-\nu)\xi^2)} \cos(\xi x) d\xi, \quad (45)$$

$$\sigma_{xy}(x, y) = \frac{P}{\pi} \int_0^\infty \frac{e^{-y(\gamma+\xi)}\xi(4e^{y\xi}\ell^2\gamma^2(1-\nu) + e^{y\gamma}(y\gamma - 4\ell^2(1-\nu)\xi^2))}{4\ell^2(1-\nu)\xi^3 - \gamma(1 + 4\ell^2(1-\nu)\xi^2)} \sin(\xi x) d\xi, \quad (46)$$

$$\sigma_{yx}(x, y) = \frac{P}{\pi} \int_0^\infty \frac{e^{-y(\gamma+\xi)}(4e^{y\xi}\ell^2(1-\nu)\xi^2 + e^{y\gamma}(y\gamma - 4\ell^2(1-\nu)\xi^2))}{4\ell^2(1-\nu)\xi^3 - \gamma(1 + 4\ell^2(1-\nu)\xi^2)} \sin(\xi x) d\xi, \quad (47)$$

$$m_{xz}(x, y) = \frac{P}{\pi} \int_0^\infty \frac{4e^{-y(\gamma+\xi)}(1-\nu)(e^{y\xi}\xi - e^{y\gamma}\gamma)\ell^2\xi}{\gamma(1 + 4\ell^2(1-\nu)\xi^2) - 4\ell^2(1-\nu)\xi^3} \cos(\xi x) d\xi, \quad (48)$$

$$m_{yz}(x, y) = \frac{P}{\pi} \int_0^\infty \frac{4e^{-y(\gamma+\xi)}(1-\nu)(e^{y\gamma} - e^{y\xi})\gamma\ell^2\xi}{\gamma(1 + 4\ell^2(1-\nu)\xi^2) - 4\ell^2(1-\nu)\xi^3} \sin(\xi x) d\xi. \quad (49)$$

In classical elasticity, for a layer of finite thickness h loaded on its surface by a normal load, the corresponding to (32) and (33) for $y = 0$ are given as:

$$u_x^{\text{class-layer}}(x, 0) = \frac{P}{2\mu\pi} \int_0^\infty \frac{(3-2\nu(5-4\nu)+2h^2\xi^2-(3-2(5-4\nu)\nu) \cosh(2h\xi))}{\xi(5-4\nu(3-2\nu)+2h^2\xi^2+(3-4\nu) \cosh(2h\xi))} \sin(\xi x) d\xi, \quad (50)$$

$$u_y^{\text{class-layer}}(x, 0) = \frac{P}{\mu\pi} \int_0^\infty \frac{(1-\nu)((3-4\nu) \sinh(2h\xi))}{\xi(5-4\nu(3-2\nu)+2h^2\xi^2+(3-4\nu) \cosh(2h\xi))} \sin(\xi x) d\xi, \quad (51)$$

$$\omega_z^{\text{class-layer}}(x, 0) = \frac{P}{\mu\pi} \int_0^\infty \frac{(1-\nu)(2h\xi - (3-4\nu) \sinh(2h\xi))}{\mu(5-4\nu)(3-2\nu)+2h^2\xi^2+(3-4\nu) \cosh(2h\xi)} \sin(\xi x) d\xi, \quad (52)$$

while the stress field at the interface ($y = h$) reads:

$$\sigma_{yy}^{\text{class-layer}}(x, h) = \frac{P}{\pi} \int_0^\infty \frac{-4(1-\nu)(2(1-\nu) \cosh(h\xi) + h\xi \sinh(h\xi))}{5-4\nu(3-2\nu)+2h^2\xi^2+(3-4\nu) \cosh(2h\xi)} \cos(\xi x) d\xi, \quad (53)$$

$$\sigma_{yx}^{\text{class-layer}}(x, h) = \frac{P}{\pi} \int_0^\infty \frac{4(1-\nu)(h\xi \cosh(h\xi) - (1-2\nu) \sinh(h\xi))}{5-4\nu(3-2\nu)+2h^2\xi^2+(3-4\nu) \cosh(2h\xi)} \sin(\xi x) d\xi. \quad (54)$$

The preceding equations for the half-plane reduce to the following set:

$$u_x^{\text{class}}(x, 0) = -\frac{P(1-2\nu)}{4\mu} \text{sgn}(x), \quad (55)$$

$$u_y^{\text{class}}(x, 0) = \frac{-P(1-\nu)}{\pi\mu} \log(x), \quad (56)$$

$$\omega_z^{\text{class}}(x, 0) = \frac{P(1-\nu)}{\pi\mu x}, \quad (57)$$

$$\sigma_{yy}^{\text{class}}(x, y) = -\frac{2Py^3}{\pi(x^2+y^2)^2}, \quad (58)$$

$$\sigma_{yx}^{\text{class}}(x, y) = -\frac{2Pxy^2}{\pi(x^2+y^2)^2}. \quad (59)$$

The asymptotic behavior of the tangential and normal displacements in the context of couple-stress elasticity for a half-plane was examined near the point of the application of the concentrated load by [Gourgiotis and Zisis 2016] by employing theorems of the Abel–Tauber type and examining the behavior of the transformed solutions for the displacements as $\xi \rightarrow \infty$. It was shown that

$$u_x^{\text{asympt}}(x, y) = \frac{P}{2\mu\pi(3-2\nu)} \left[-(1-2\nu) \frac{xy}{r^2} + \tan^{-1}\left(\frac{x}{y}\right) \right], \quad (60)$$

$$u_y^{\text{asympt}}(x, y) = -\frac{P}{2\mu\pi(3-2\nu)} \left[(1-2\nu) \frac{y^2}{r^2} + 2(1-\nu) \log(r) \right], \quad (61)$$

with $r = (x^2 + y^2)^{1/2}$.

As a final comment we note that examination of the transformed normal displacements for the case of the layer and regardless of the theory employed, suggests that $u_y(x, 0) \rightarrow 0$ as $x \rightarrow 0$. In marked difference, for the case of the half-plane, the integrand in (33) behaves as $\hat{u}_y(\xi, y) = O(\xi^{-1})$ for $\xi \rightarrow 0$, and, thus, $u_y(x, y)$ exhibits a logarithmic behavior as $x \rightarrow \infty$. It can be furthermore shown that regardless again of the theory employed, the strains remain singular and behave as $\varepsilon_{ij} = O(x^{-1})$ for $x \rightarrow 0$. However, in marked contrast to the classical elasticity theory, in the couple stress theory, the rotation is bounded at the point of application of the load. It is noted that in the classical theory the rotation is singular, exhibiting $O(x^{-1})$ singular behavior as $x \rightarrow 0$, see (57).

4. Results and discussion

Results regarding the behavior of the surface ($y = 0$) in terms of displacement and rotation of a layer loaded by a normal load in the frame of classical as well as in couple-stress elasticity are presented in Figures 2–5. Furthermore, full-field results are presented in terms of contours in Figures 6–8. Normalization of the problem suggests that the distance from the point of the application of the load should be normalized with the thickness of the layer (x/h), the normal and tangential displacements should be normalized as $\mu u_x/P$, $\mu u_y/P$ respectively and the rotations should be normalized as $\mu h \omega_z/P$.

We begin the discussion from the case of the layer in the context of classical elasticity. In Figure 2 we present the displacements and rotation of the layer's surface ($y = 0$) for two different values of the

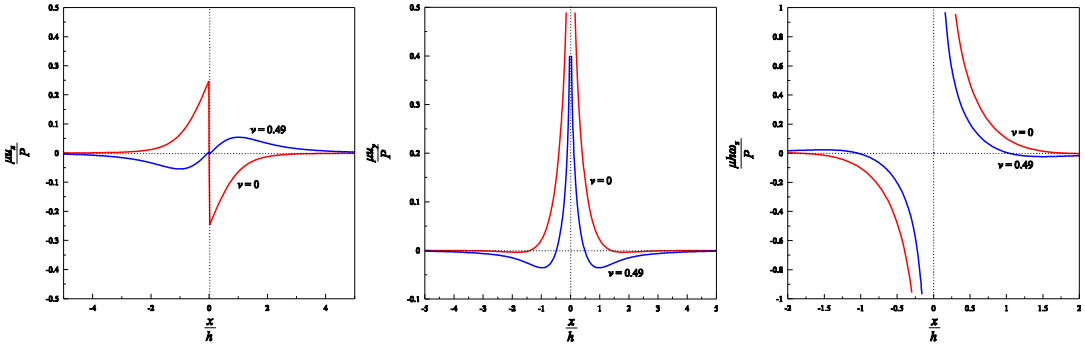


Figure 2. Behavior of the surface of a layer of thickness h under the action of a normal point load in the frame of classical elasticity. Tangential displacement $\mu u_x/P$ (left), normal displacement $\mu u_y/P$ (middle) and rotation angle $\mu h\omega_z/P$ (right) are presented as functions of the normalized distance x/h from the point of the application of the load P for two different Poisson's ratios: $\nu = 0$ (red) and $\nu = 0.49$ (blue).

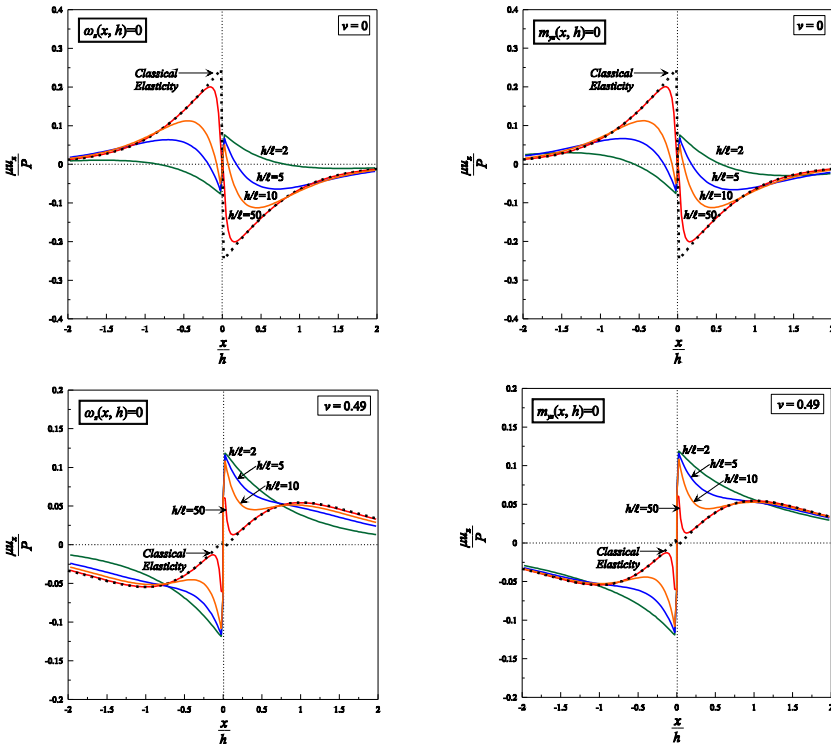


Figure 3. Behavior of the surface of a layer of thickness h under the action of a normal point load in the frame of couple stress elasticity. The normalized tangential displacements $\mu u_x/P$ are plotted versus the normalized distance x/h from the point of the application of the load P for two Poisson's ratios (top, $\nu = 0$; bottom, $\nu = 0.49$) and two different boundary conditions at the interface: either $\omega_z(x, h) = 0$ (left) or $m_{yz}(x, h) = 0$ (right). The classical elasticity solution for the layer of thickness h is superimposed.

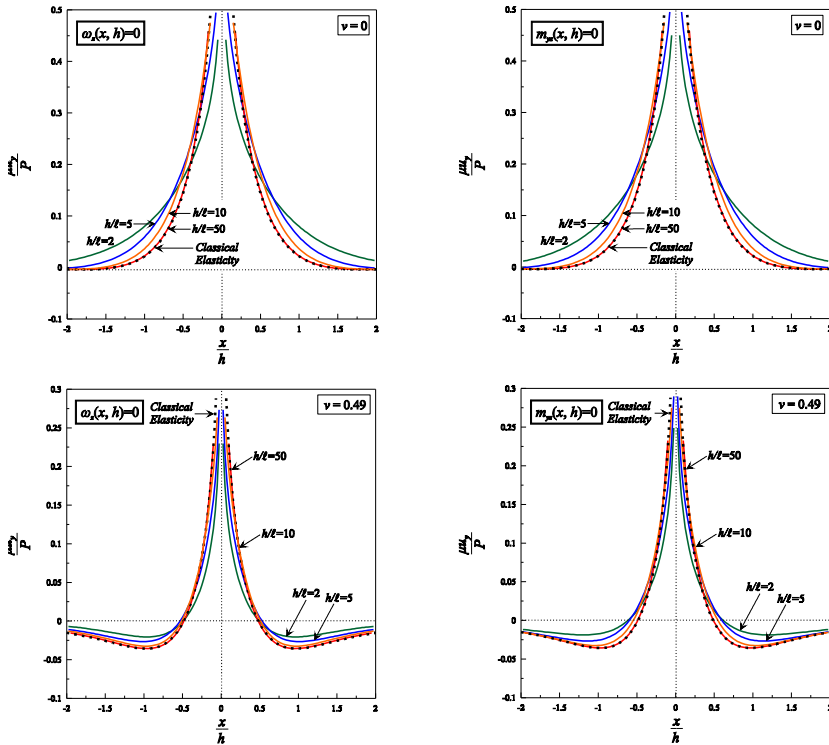


Figure 4. Behavior of the surface of a layer of thickness h under the action of a normal point load in the frame of couple stress elasticity. The normalized normal displacements $\mu u_y/P$ are plotted versus the normalized distance x/h from the point of the application of the load P for two Poisson's ratios (top, $\nu = 0$; bottom, $\nu = 0.49$) and two different boundary conditions at the interface: either $\omega_z(x, h) = 0$ (left) or $m_{yz}(x, h) = 0$ (right). The classical elasticity solution for the layer of thickness h is superimposed.

Poisson's ratio. The normalization proposed suggests that in the case of classical elasticity the curves are unique for a fixed value of Poisson's ratio. The discontinuous tangential displacement and the singular behavior of the normal displacement at the point of the application of the load are the same as in the case of the half-plane ($h \rightarrow \infty$) but as we move further from the point of the application of the load the normal displacements decay and can be seen that essentially for $x/h \geq 5$ they vanish for both values of Poisson's ratio. It is further noted that for almost incompressible material the surface laterally to the point of the application of the load is piling-up (Figure 2, middle) while the rotation, being unbounded at the point of application of the load, increases for decreasing Poisson's ratio.

Next, we move to the case of the surface of the layer in the frame of couple-stress elasticity (Figures 3–8). Here we present the normal and tangential displacements as well as the rotation for selected values of Poisson's ratio. The results are shown for two different sets of boundary conditions at the layer/rigid substrate interface. We conclude that the effect of the two different sets of boundary conditions at the bottom of the layer is of minor importance upon the displacements and the rotation at the surface. As expected as the layer thickness increases the effect decays.

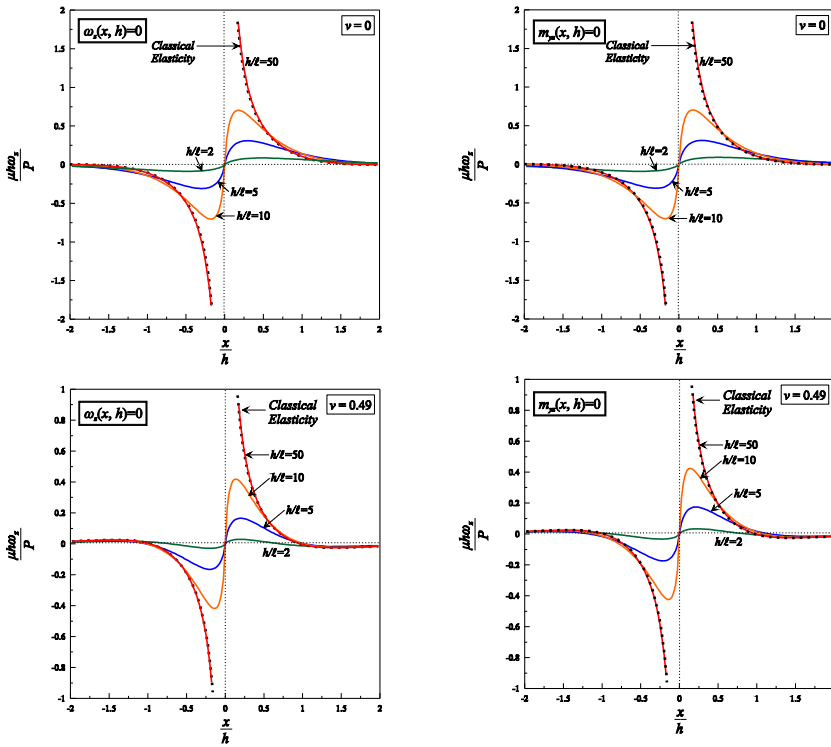


Figure 5. Behavior of the surface of a layer of thickness h under the action of a normal point load in the frame of couple stress elasticity. The normalized rotation $\mu h \omega_z / P$ is presented as a function of the normalized distance x / h from the point of the application of the load P for two Poisson's ratios (top, $\nu = 0$; bottom, $\nu = 0.49$) and two different boundary conditions at the interface: either $\omega_z(x, h) = 0$ (left) or $m_{yz}(x, h) = 0$ (right). The classical elasticity solution for the layer of thickness h is superimposed.

In the case of couple-stress elasticity the displacement components and the rotation at the surface depend upon both the Poisson's ratio and the normalized length h/ℓ . For fixed layer thickness h and increasing ℓ or increasing Poisson's ratio the layer becomes stiffer. In fact it can be seen that both ℓ and ν play an important role in the qualitative characteristics of the behavior of the layer's surface. Note that in all the cases the classical elasticity layer solution is added. In general all the significant variations are observed in a region that extends about $x/h \approx 2$ laterally to the point of the application of the load and the gradient effects become important for decreasing h/ℓ —a stiffer layer can be obtained by reducing the thickness h or increasing the microstructural length ℓ . Furthermore, for increasing ℓ and decreasing ν the deformation field is rather confined to a region near the point of application of the load and the effect of the boundary conditions becomes significant as ℓ increases compared to the layer thickness.

Moving further from the point of the application of the load the effect of the rotation gradients gradually diminishes and the results regarding all the measured quantities converge to those of classical elasticity. In fact for increasing h/ℓ ratio the region of significance of the effect of the rotation gradients, in terms of x/h , decreases. It is concluded that for $h \geq 50\ell$ the displacements and the rotation have essentially

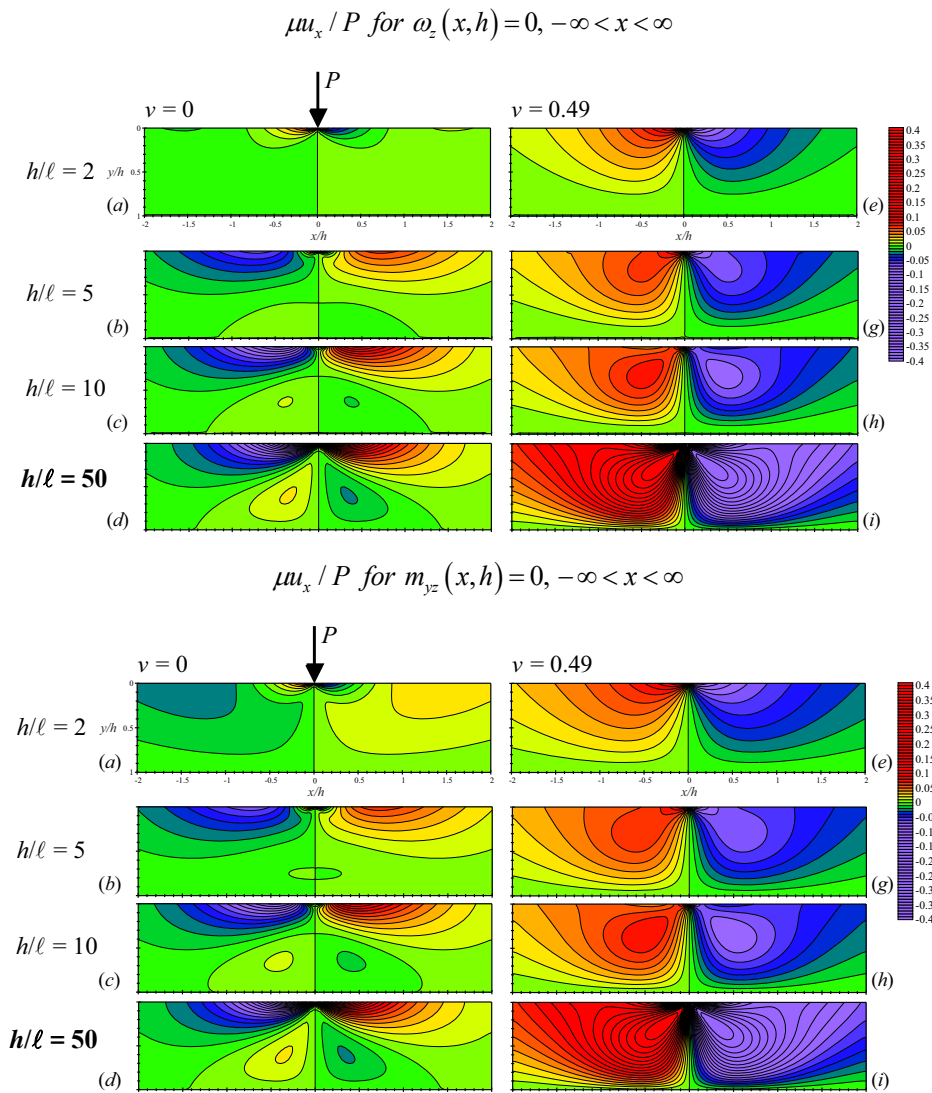


Figure 6. Contour fields of the normalized displacements $\mu u_x / P$ for different ratios h/ℓ and Poisson's ratios $\nu = 0$ and $\nu = 0.49$ in the frame of couple stress elasticity for $\omega_z(x, h) = 0$ and $m_{yz}(x, h) = 0$ at the interface. For increasing ℓ and decreasing ν the deformation field is confined to the region near the point of the application of the load.

converged to those obtained by classical elasticity excluding of course the singular behavior of the rotation observed in classical elasticity.

Next we examine the stress, couple stress and rotation fields at $y = h$ (that is the interface between the layer and the rigid substrate). The two different boundary conditions discussed previously are again considered and when $m_{yz} = 0$ we present the variation of the conjugate ω_z along the interface. The results are shown for selected values of Poisson's ratio ($\nu = 0$ and $\nu = 0.49$). For $\nu = 0$ and $\omega_z(x, h) = 0$ the

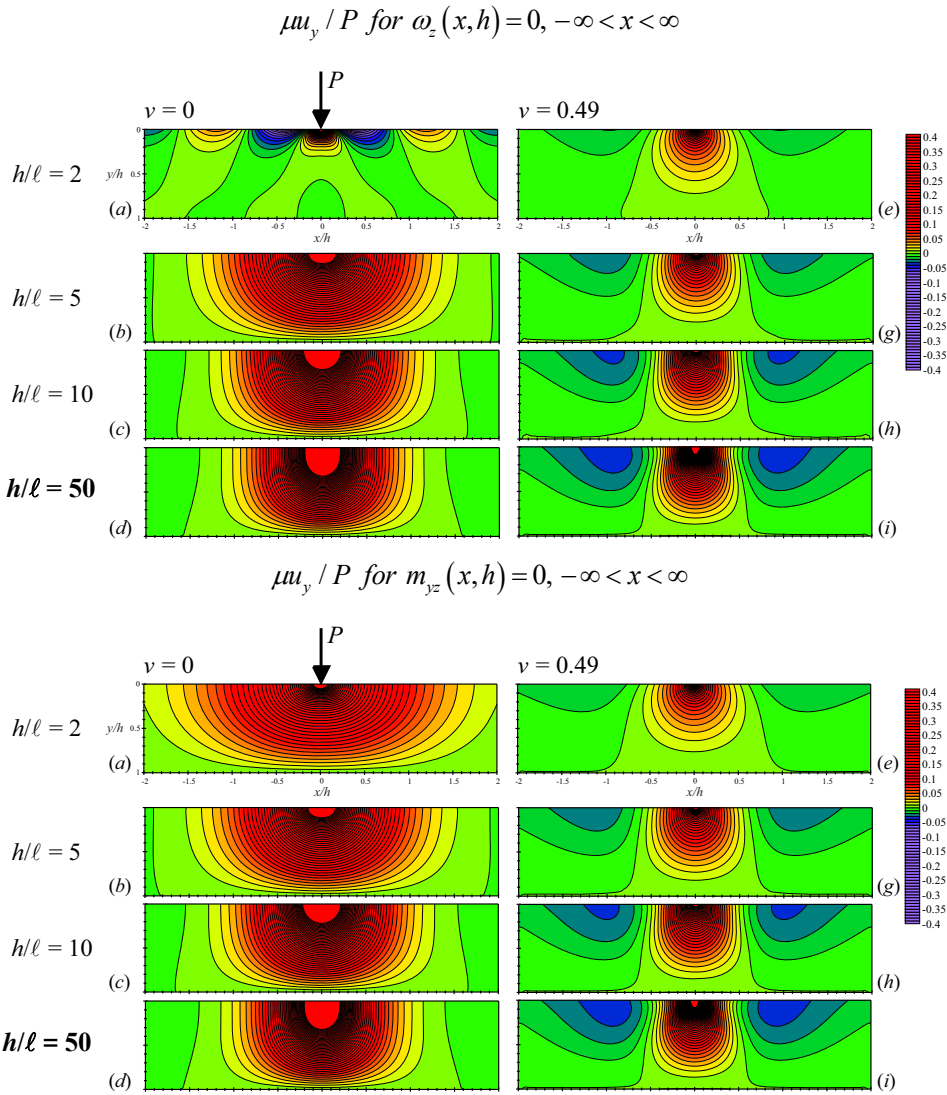


Figure 7. Contour fields of the normalized displacements $\mu u_y / P$ for different ratios h/ℓ and Poisson's ratios $\nu = 0$ and $\nu = 0.49$ in the frame of couple stress elasticity for $\omega_z(x, h) = 0$ and $m_{yz}(x, h) = 0$ at the interface.

normal stresses decrease for decreasing h/ℓ , everywhere along the interface are compressive and their peak values are bounded by the corresponding normal stresses obtained from classical elasticity. The shear stresses σ_{yx} are found decreased (at the region $-1 \leq x/h \leq 1$) compared to those that correspond to classical elasticity and at fixed x/h change sign for decreasing h/ℓ . Furthermore, m_{yz} decreases for increasing h/ℓ . For increasing Poisson's ratio all the stresses and couple-stresses increase and become higher than those obtained by classical elasticity theory. Furthermore, for decreasing h/ℓ and increasing Poisson's ratio the normal stresses become tensile at $1 \leq x/h \leq 2$ from the point of the application of

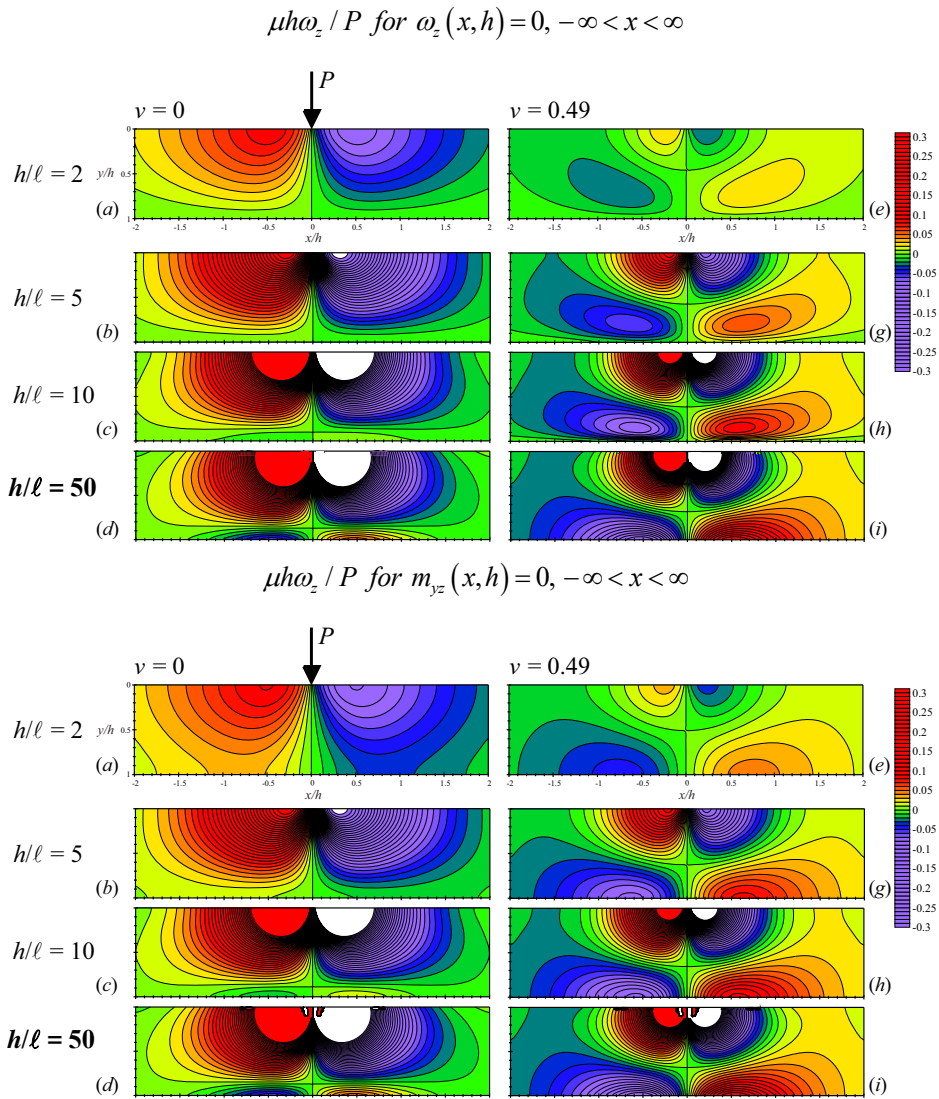


Figure 8. Contour fields of the normalized rotation $\mu h \omega_z / P$ for different ratios h/ℓ and Poisson's ratios $\nu = 0$ and $\nu = 0.49$ in the frame of couple stress elasticity for $\omega_z(x, h) = 0$ and $m_{yz}(x, h) = 0$ at the interface. The white region indicates $\mu h \omega_z / P < -0.3$.

the load. Finally, this region of tensile stresses vanishes for $m_{yz}(x, h) = 0$ instead of $\omega_z(x, h) = 0$ at $\nu = 0.49$.

We further note that bounded rotations have been found in both static as well as dynamic problems for concentrated loads in the context of the anisotropic couple-stress elasticity (see [Gourgiotis and Bigoni 2016; 2017] while similar results, in terms of rotations, have been observed in problems involving cracks within the same theory [Gourgiotis 2017; Mishuris et al. 2012; Morini et al. 2013; 2014; Piccolroaz et al.

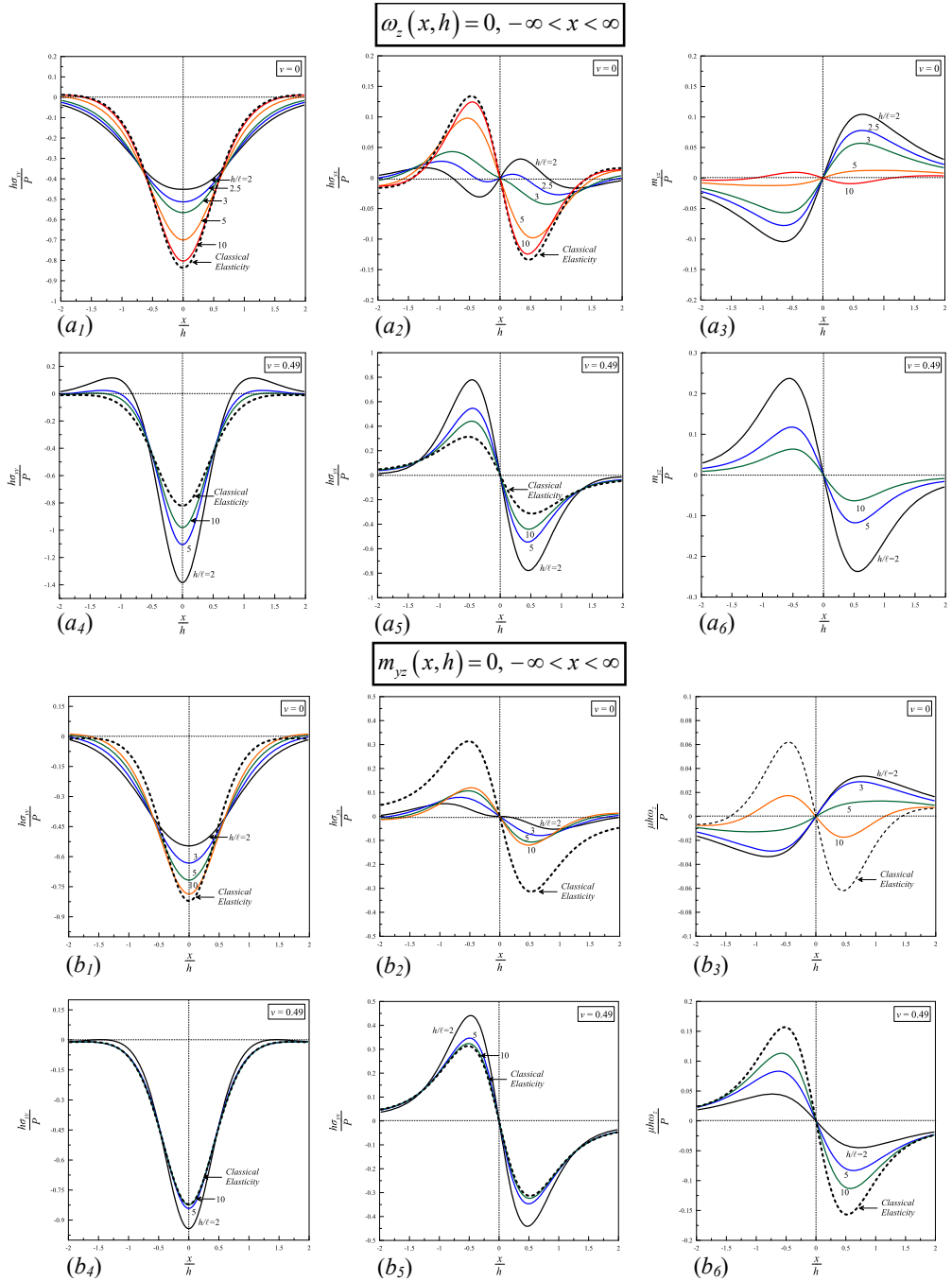


Figure 9. Normalized stress (σ_{yy} , σ_{yx}), couple stress (m_{yz}) or rotation (ω_z) distributions along the interface between the layer and the rigid substrate ($y = h$) in the frame of couple stress elasticity. Results are presented for the two different boundary conditions at the interface, $\omega_z(x, h) = 0$ (top) and $m_{yz}(x, h) = 0$ (bottom). The effect of Poisson's ratio is also shown for $\nu = 0$ and $\nu = 0.49$. The classical elasticity results are superimposed.

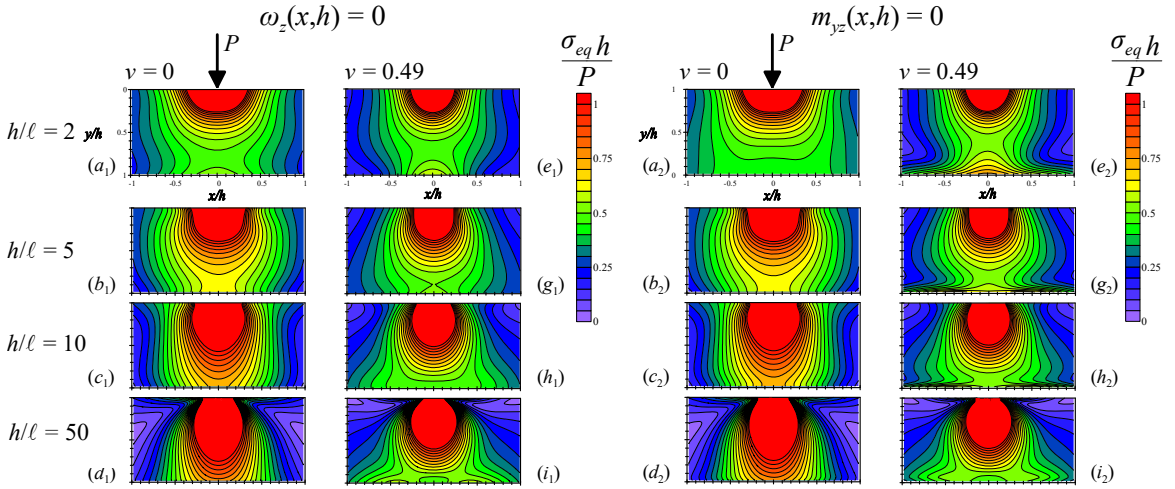


Figure 10. Contours of normalized equivalent stress $\sigma_{eq} h / P$ for different ratios h/ℓ . Results are presented for the two different boundary conditions at the interface, $\omega_z(x, h) = 0$ (left) and $m_{yz}(x, h) = 0$ (right). The effect of Poisson's ratio is also shown for $\nu = 0$ and $\nu = 0.49$.

2012; Radi 2008]. It should be further underlined that in contrast to concentrated load problems in the frame of the antiplane couple stress formulation, which predict bounded displacements as well as bounded strains at the point of the application of the load, here, in the plane strain formulation, both normal displacements as well as strains are in fact unbounded [Gourgiotis and Bigoni 2016; 2017; Zisis 2017]. Bounded strains have been found in Mode III cracks in the context of couple stress elasticity [Mishuris et al. 2012; Morini et al. 2013; 2014; Piccolroaz et al. 2012; Radi 2008].

It is also instructive to examine the equivalent stress in order identify the severest stress state and accordingly the potential regions with respect to the point of the application of the load, that plasticity may emanate. In the context of couple stress theory the shape of the equivalent stress contours depends upon the microstructural characteristics of the material. For the case of couple stress elasticity and according to J_2 -flow theory, following [de Borst 1993] and [Shu and Fleck 1998], we introduce a general form of the normalized equivalent stress as:

$$\sigma_{eq} = \sqrt{3 \left(\frac{1}{2} (s_{xx}^2 + s_{yy}^2 + s_{zz}^2) + \frac{1}{4} \sigma_{xy}^2 + \frac{1}{2} \sigma_{xy} \sigma_{yx} + \frac{1}{4} \sigma_{yx}^2 + \frac{1}{2} \ell^2 (m_{xz}^2 + m_{yz}^2) \right)}, \quad (62)$$

where $s_{ij} = \sigma_{ij} - \frac{1}{3} \delta_{ij} \sigma_{\kappa\kappa}$ is the deviatoric stress.

When the equivalent stress reaches the material yield stress, yielding will commence — although the plastic enclave will be surrounded by elastic material — and at loads modestly above the elastic limit might be approximated in shape by one of the contours in Figure 10 depending upon the microstructural characteristic length ℓ and the Poisson's ratio ν assuming fixed layer thickness h . It is observed that for decreasing ℓ the maximum equivalent stress increases and the region of maximum equivalent stress expands vertically while it rather shrinks horizontally. For $\ell \rightarrow 0$ ($h/\ell \rightarrow \infty$, the classical elasticity solution), the maximum of the equivalent stress is shifted inside the layer and the potential yielding

region increases substantially almost reaching the interface between the layer and the rigid substrate. The effect of the boundary conditions at the interface upon the equivalent stress is also shown. As a final comment we note that classical elasticity suggest that at the surface of the layer or the half-plane the equivalent stress vanish. It can be seen from [Figure 10](#) that this is not true for the case of couple stress elasticity due to the fact that as $y \rightarrow 0$, σ_{xx} , σ_{xy} and m_{xz} need not necessarily vanish. It is concluded that in order to avoid extensive plastic regions within the layer the ratio h/ℓ should be kept as low as possible, and the Poisson's ratio should be increased.

5. Conclusions

In the present work we examined the behavior of a microstructured layer bonded on a rigid substrate, under the action of a point load on its surface. This is essentially an extended version of the classical Burmister's problem in the context of a generalized theory of elasticity.

We have shown that both displacements (tangential and normal) present the same asymptotic characteristics near the point of the application of the load for both classical as well couple stress elasticity and this is in fact true for the case of the half-plane as well as the case of the layer of finite thickness. Nevertheless, both the quantitative and qualitative characteristics of the displacements are strongly affected by the ratio h/ℓ and this is for the first time shown. Furthermore, the rotation at the point of the application of the load is bounded in the frame of couple stress elasticity while it is singular in the frame of classical elasticity. Furthermore, as h/ℓ varies, the rotation field is strongly affected. It is furthermore shown, that when $h/\ell \geq 50$ the classical elasticity solution adequately predicts the behavior of the layer and the microstructural effects are of minor importance.

The results are important for the construction and the solution of more complicated contact problems towards the understanding of experimental details involved in the indentation technique for the mechanical characterization of coatings and thin films. Furthermore, the present results shed light to contact problems that take place in structural engineering given that structures are founded in reinforced concrete footings or pads buried at relatively shallow depths beneath the ground surface and large scale contacts take place between the footings and the deformable ground.

As a final comment, we note that the present approach and results are applicable to systems in which the substrate is much stiffer than the layer. Such systems can be found, among other areas, in aerospace applications. For example during the *high temperature* erosion of thermal barrier coatings experimental findings suggest that the observed deformation of the substrate is confined compared to the columnar ceramic layer (zirconia 8% yttria stabilized)—see for example [[Chen et al. 2003](#); [Fleck and Zisis 2010](#); [Zisis and Fleck 2010](#)] as well as the references therein. On the other hand, there are systems that the substrate is less stiff than the layer. Such systems are among others, titanium nitride and diamond like carbon thin films deposited on aluminium substrates that are used in magnetic hard disk industry. In this case it is of great interest to present the corresponding solutions, in the context of couple stress elasticity, incorporating in addition to the deformable layer a deformable substrate. It is expected that, apart from ratio of the classical material properties, the ratio of the characteristic lengths will be important to the system response and cases where the layer is stiffer than the substrate can be evaluated. This is within our scope for a future work.

Appendix

System of eight linear equations for the solution of $B_i(\xi)$ and $C_i(\xi)$ with $i = 1, \dots, 4$. Depending upon the boundary conditions at the bottom of the layer we have (for $\xi \geq 0$):

(1) Vanishing displacements and rotations at the bottom of the layer:

$$\begin{pmatrix} -\xi^2 & -\xi^2 & -\xi^2 & -\xi^2 & -i\xi^2 & i\xi & i\xi^2 & i\xi \\ -\xi & -\gamma & \xi & \gamma & 0 & 0 & 0 & 0 \\ i\xi^2 & i\xi\gamma & -i\xi^2 & -i\xi\gamma & -\xi^2 & 0 & -\xi^2 & 0 \\ \frac{e^{-h\xi}\xi}{2\mu} & \frac{e^{-h\gamma}\gamma}{2\mu} & -\frac{e^{h\xi}\xi}{2\mu} & -\frac{e^{h\gamma}\gamma}{2\mu} & \frac{ie^{-h\xi}\xi}{2\mu} & -\frac{ie^{-h\xi}(2(1-\nu)-h\xi)}{2\mu} & \frac{ie^{h\xi}\xi}{2\mu} & \frac{ie^{h\xi}(2(1-\nu)+h\xi)}{2\mu} \\ -\frac{ie^{-h\xi}\xi}{2\mu} & -\frac{ie^{-h\gamma}\gamma}{2\mu} & -\frac{ie^{h\xi}\xi}{2\mu} & -\frac{ie^{h\gamma}\gamma}{2\mu} & \frac{e^{-h\xi}\xi}{2\mu} & \frac{e^{-h\xi}(1-2\nu+h\xi)}{2\mu} & -\frac{e^{h\xi}\xi}{2\mu} & \frac{e^{h\xi}(1-2\nu-h\xi)}{2\mu} \\ 0 & -\frac{e^{-h\gamma}}{4\ell^2\mu} & 0 & -\frac{e^{h\gamma}}{4\ell^2\mu} & 0 & \frac{ie^{-h\xi}(1-\nu)\xi}{\mu} & 0 & \frac{ie^{h\xi}(1-\nu)\xi}{\mu} \\ 1 & 0 & 0 & 0 & 0 & 4i\ell^2(1-\nu)\xi & 0 & 0 \\ 0 & 0 & 1 & 0 & 0 & 0 & 0 & 4i\ell^2(1-\nu)\xi \end{pmatrix} \begin{pmatrix} B_1(\xi) \\ B_2(\xi) \\ B_3(\xi) \\ B_4(\xi) \\ C_1(\xi) \\ C_2(\xi) \\ C_3(\xi) \\ C_4(\xi) \end{pmatrix} = \begin{pmatrix} 0 \\ 0 \\ P \\ 0 \\ 0 \\ 0 \\ 0 \\ 0 \end{pmatrix}$$

(2) Vanishing displacements and couple stresses at the bottom of the layer:

$$\begin{pmatrix} -\xi^2 & -\xi^2 & -\xi^2 & -\xi^2 & -i\xi^2 & i\xi & i\xi^2 & i\xi \\ -\xi & -\gamma & \xi & \gamma & 0 & 0 & 0 & 0 \\ i\xi^2 & i\xi\gamma & -i\xi^2 & -i\xi\gamma & -\xi^2 & 0 & -\xi^2 & 0 \\ \frac{e^{-h\xi}\xi}{2\mu} & \frac{e^{-h\gamma}\gamma}{2\mu} & -\frac{e^{h\xi}\xi}{2\mu} & -\frac{e^{h\gamma}\gamma}{2\mu} & \frac{ie^{-h\xi}\xi}{2\mu} & -\frac{ie^{-h\xi}(2(1-\nu)-h\xi)}{2\mu} & \frac{ie^{h\xi}\xi}{2\mu} & \frac{ie^{h\xi}(2(1-\nu)+h\xi)}{2\mu} \\ -\frac{ie^{-h\xi}\xi}{2\mu} & -\frac{ie^{-h\gamma}\gamma}{2\mu} & -\frac{ie^{h\xi}\xi}{2\mu} & -\frac{ie^{h\gamma}\gamma}{2\mu} & \frac{e^{-h\xi}\xi}{2\mu} & \frac{e^{-h\xi}(1-2\nu+h\xi)}{2\mu} & -\frac{e^{h\xi}\xi}{2\mu} & \frac{e^{h\xi}(1-2\nu-h\xi)}{2\mu} \\ -e^{-h\xi}\xi & -e^{-h\gamma}\gamma & e^{h\xi}\xi & e^{h\gamma}\gamma & 0 & 0 & 0 & 0 \\ 1 & 0 & 0 & 0 & 0 & 4i\ell^2(1-\nu)\xi & 0 & 0 \\ 0 & 0 & 1 & 0 & 0 & 0 & 0 & 4i\ell^2(1-\nu)\xi \end{pmatrix} \begin{pmatrix} B_1(\xi) \\ B_2(\xi) \\ B_3(\xi) \\ B_4(\xi) \\ C_1(\xi) \\ C_2(\xi) \\ C_3(\xi) \\ C_4(\xi) \end{pmatrix} = \begin{pmatrix} 0 \\ 0 \\ P \\ 0 \\ 0 \\ 0 \\ 0 \\ 0 \end{pmatrix}$$

where $\gamma \equiv \gamma(\xi) = (1/\ell^2 + \xi^2)^{1/2}$.

References

[Bacca et al. 2013] M. Bacca, D. Bigoni, F. Dal Corso, and D. Veber, "Mindlin second-gradient elastic properties from dilute two-phase Cauchy-elastic composites, I: Closed form expression for the effective higher-order constitutive tensor", *Int. J. Solids Struct.* **50** (2013), 4010–4019.

[Barber 2010] J. R. Barber, *Elasticity*, 3rd ed. ed., Solid mechanics and its applications **172**, Springer, 2010.

[Begley and Hutchinson 1998] M. R. Begley and J. W. Hutchinson, "The mechanics of size-dependent indentation", *J. Mech. Phys. Solids* **46** (1998), 2049–2068.

[Bigoni and Drugan 2007] D. Bigoni and W. J. Drugan, "Analytical derivation of cosserat moduli via homogenization of heterogeneous elastic materials", *J. Appl. Mech. (ASME)* **74** (2007), 741–753.

[Biot 1935] M. A. Biot, "Effect of certain discontinuities on the pressure distribution in a loaded soil", *J. Appl. Phys.* **6**:12 (1935), 367–375.

[de Borst 1993] R. de Borst, "A generalisation of J2-flow theory for polar continua", *Computer Methods Appl. Mech. Eng.* **103**:3 (1993), 347–362.

[Burmister 1943] D. M. Burmister, "Theory of stress and displacement in layered system and applications to the design of airport", in *Proceedings of Annual Meeting of the Transportation Research Board*, Highway Research Board, Washington, DC, 1943.

- [Burmister 1945a] D. M. Burmister, “The general theory of stresses and displacements in layered systems, I”, *J. Appl. Phys.* **16**:2 (1945), 89–94.
- [Burmister 1945b] D. M. Burmister, “The general theory of stresses and displacements in layered soil systems, III”, *J. Appl. Phys.* **16**:5 (1945), 296–302.
- [Burmister 1956] D. M. Burmister, “Stress and displacement characteristics of a two-layer rigid base soil system: influence diagrams and practical applications”, *Proc. Highway Res. Board* **35** (1956), 773–814.
- [Burmister et al. 1944] D. M. Burmister, L. A. Palmer, E. S. Barber, and T. A. Middlebrooks, “The theory of stress and displacements in layered systems and applications to the design of airport runways”, *Highway Res. Board Proc.* **23** (1944), 126–148.
- [Chen et al. 1998] J. Y. Chen, Y. Huang, and M. Ortiz, “Fracture analysis of cellular materials: a strain gradient model”, *J. Mech. Phys. Solids* **46** (1998), 789–828.
- [Chen et al. 2003] X. Chen, R. Wang, N. Yao, A. G. Evans, J. W. Hutchinson, and R. W. Bruce, “Foreign object damage in a thermal barrier system: mechanisms and simulations”, *Mater. Sci. Eng. A* **352** (2003), 221.
- [Davis and Poulos 1963] E. H. Davis and H. G. Poulos, “Triaxial testing and three-dimensional settlement analysis”, research report, Peter Nicol Russell School of Civil Engineering, University of Sydney, 1963.
- [Davis and Taylor 1961] E. H. Davis and H. Taylor, “The surface displacement of an elastic layer due to horizontal and vertical surface loading”, pp. 621– in *Proc. 5th Intern. Conf. Soil Mechanics and Foundation Engineering* (Paris, 1961), vol. 1, Dunod, Paris, 1961.
- [Fleck and Zisis 2010] N. A. Fleck and T. Zisis, “The erosion of EB-PVD thermal barrier coatings: The competition between mechanisms”, *Wear* **268** (2010), 1214–1224.
- [Fung 1965] Y. C. Fung, *Foundations of solid mechanics*, Prentice-Hall, Englewood Cliffs, NJ, 1965.
- [Georgiadis and Anagnostou 2008] H. G. Georgiadis and D. S. Anagnostou, “Problems of the Flamant–Boussinesq and Kelvin type in dipolar gradient elasticity”, *J. Elasticity* **90** (2008), 71–98.
- [Gourgiotis 2017] P. A. Gourgiotis, “Shear crack growth in brittle materials modeled by constrained Cosserat elasticity”, *J. Eur. Ceram. Soc.* **38**:8 (2017), 3025–3036.
- [Gourgiotis and Bigoni 2016] P. A. Gourgiotis and D. Bigoni, “Stress channelling in extreme couple-stress materials Part I: Strong ellipticity, wave propagation, ellipticity, and discontinuity relations”, *J. Mech. Phys. Solids* **88** (2016), 150–168.
- [Gourgiotis and Bigoni 2017] P. A. Gourgiotis and D. Bigoni, “The dynamics of folding instability in a constrained Cosserat medium”, *Phil. Trans. R. Soc. A* **375**:2093 (2017), 20160159.
- [Gourgiotis and Piccolroaz 2014] P. A. Gourgiotis and A. Piccolroaz, “Steady-state propagation of a Mode II crack in couple stress elasticity”, *Int. J. Fract.* **188** (2014), 119–145.
- [Gourgiotis and Zisis 2016] P. Gourgiotis and T. Zisis, “Two-dimensional indentation of microstructured solids characterized by couple-stress elasticity”, *J. Strain Anal. Eng. Des.* **51**:4 (2016), 318–331.
- [Gourgiotis et al. 2018] P. A. Gourgiotis, T. Zisis, and H. G. Georgiadis, “On concentrated surface loads and Green’s functions in the Toupin–Mindlin theory of strain-gradient elasticity”, *Int. J. Solids Struct.* **130** (2018), 153–171.
- [Green and Zerna 1968] A. E. Green and W. Zerna, *Theoretical elasticity*, Oxford University Press, Oxford, 1968.
- [Hills and Nowell 1994] D. Hills and D. Nowell, *Mechanics of fretting fatigue*, Kluwer, Dordrecht, 1994.
- [Johnson 1985] K. Johnson, *Contact mechanics*, Cambridge University Press, Cambridge, UK, 1985.
- [Koiter 1964a] W. T. Koiter, “Couple stresses in the theory of elasticity, I”, *Proc. Kon. Nederl. Akad. Wetensch. B* **67** (1964), 17–29.
- [Koiter 1964b] W. T. Koiter, “Couple stresses in the theory of elasticity, II”, *Proc. Kon. Nederl. Akad. Wetensch. B* **67** (1964), 30–44.
- [Love 1952] A. E. H. Love, *A treatise on the mathematical theory of elasticity*, Cambridge University Press, New York, 1952.
- [Maranganti and Sharma 2007] R. Maranganti and P. Sharma, “A novel atomistic approach to determine strain-gradient elasticity constants: Tabulation and comparison for various metals, semiconductors, silica, polymers and the (Ir) relevance for nanotechnologies”, *J. Mech. Phys. Solids* **55** (2007), 1823–1852.

- [Marguerre 1931] K. Marguerre, "Druckverteilung durch eine elastische Schicht auf starrer rauher Unterlage", *Arch. Appl. Mech.* **2**:1 (1931), 108–117.
- [Mindlin 1963] R. D. Mindlin, "Influence of couple-stresses on stress concentrations", *Experim. Mech.* **3**:1 (1963), 1–7.
- [Mindlin and Tiersten 1962] R. D. Mindlin and H. F. Tiersten, "Effects of couple-stresses in linear elasticity", *Arch. Ration. Mech. Anal.* **11** (1962), 415–448.
- [Mishuris et al. 2012] G. Mishuris, A. Piccolroaz, and E. Radi, "Steady-state propagation of a Mode III crack in couple stress elastic materials", *Int. J. Eng. Sci.* **61** (2012), 112–128.
- [Morini et al. 2013] L. Morini, A. Piccolroaz, G. Mishuris, and E. Radi, "On fracture criteria for dynamic crack propagation in elastic materials with couple stresses", *Int. J. Eng. Sci.* **71** (2013), 45–61.
- [Morini et al. 2014] L. Morini, A. Piccolroaz, and G. Mishuris, "Remarks on the energy release rate for an antiplane moving crack in couple stress elasticity", *Int. J. Solids Struct.* **51**:18 (2014), 3087–3100.
- [Muki and Sternberg 1965] R. Muki and E. Sternberg, "The influence of couple-stresses on singular stress concentrations in elastic solids", *Z. Angew. Math. Phys.* **16** (1965), 611–648.
- [Nix and Gao 1998] W. D. Nix and H. Gao, "Indentation size effects in crystalline materials: a law for strain gradient plasticity", *J. Mech. Phys. Solids* **46** (1998), 411–425.
- [Piccolroaz et al. 2012] A. Piccolroaz, G. Mishuris, and E. Radi, "Mode III interfacial crack in the presence of couple stress elastic materials", *Eng. Fract. Mech.* **80**:1 (2012), 60–71.
- [Pickett 1938] G. Pickett, pp. 35–47 in *Proc. Highw. Res. Board*, vol. 18, 1938.
- [Poole et al. 1996] W. J. Poole, M. F. Ashby, and N. A. Fleck, "Micro-hardness of annealed and work-hardened copper polycrystals", *Scr. Mater.* **34** (1996), 559–564.
- [Poulos 1967] H. G. Poulos, "Stresses and displacements in an elastic layer underlain by a rough rigid base", *Géotechnique* **17**:4 (1967), 378–410.
- [Radi 2008] E. Radi, "On the effects of the characteristic lengths in bending and torsion on Mode III crack in couple stress elasticity", *Int. J. Solids Struct.* **45**:10 (2008), 3033–3058.
- [Schiffman 1957] R. L. Schiffman, "The numerical solution for stresses and displacements in a three-layer soil system", pp. 169–173 in *Proceedings of the 4th International Conference on Soil Mechanics and Foundation Engineering*, vol. 2, 1957.
- [Shodja et al. 2013] H. M. Shodja, A. Zaheri, and A. Tehranchi, "Ab initio calculations of characteristic lengths of crystalline materials in first strain gradient elasticity", *Mech. Mater.* **61** (2013), 73–78.
- [Shu and Fleck 1998] J. Y. Shu and N. A. Fleck, "The prediction of a size effect in microindentation", *Int. J. Solids Struct.* **35** (1998), 1363–1383.
- [Tekoglu and Onck 2008] C. Tekoglu and P. R. Onck, "Size effect in two dimensional Voronoi foams. A comparison between generalized continua and discrete models", *J. Mech. Phys. Solids* **56** (2008), 3541–3564.
- [Timoshenko and Goodier 1970] S. P. Timoshenko and J. N. Goodier, *Theory of elasticity*, McGraw-Hill, New York, 1970.
- [Toupin 1964] R. A. Toupin, "Theories of elasticity with couple-stress", *Arch. Ration. Mech. Anal.* **17** (1964), 85–112.
- [Wei and Hutchinson 2003] Y. Wei and J. W. Hutchinson, "Hardness trends in micron scale indentation", *J. Mech. Phys. Solids* **51** (2003), 2037–2056.
- [Zisis 2017] T. Zisis, "Anti-plane loading of microstructured materials in the context of couple stress theory of elasticity: half-planes and layers", *Arch. Appl. Mech.* (2017), 1–14.
- [Zisis and Fleck 2010] T. Zisis and N. A. Fleck, "The elastic-plastic indentation response of a columnar thermal barrier coating", *Wear* **268** (2010), 443–454.
- [Zisis et al. 2014] T. Zisis, P. A. Gougiotis, K. P. Baxevanakis, and H. G. Georgiadis, "Some basic contact problems in couple-stress elasticity", *Int. J. Solids Struct.* **51** (2014), 2084–2095.

Received 31 Jan 2018. Revised 13 Mar 2018. Accepted 19 Mar 2018.

THANASIS ZISIS: zisis@mail.ntua.gr

Mechanics Division, National Technical University of Athens, Athens, Greece

MULTIPLE CRACK DAMAGE DETECTION OF STRUCTURES USING SIMPLIFIED PZT MODEL

NARAYANAN JINESH AND KRISHNAPILLAI SHANKAR

A novel damage identification scheme for multiple cracks in beams is presented based on the one-dimensional (1-D) piezoelectric patch with beam model. A hybrid element constituted of a 1-D beam element and a PZT sensor is used with reduced material properties. This model is more convenient and simpler for crack identification of beams than using a complex 3-D patch model. The hybrid beam element and the multiple crack identification procedure is verified experimentally. The crack identification is carried out as an inverse problem whereby location and depth parameters are identified by minimizing the deviation between the predicted and measured voltage responses of the patch when subjected to excitations. In the proposed method, a patch is attached to either end of the fixed beam. The numerical and experimental results show that there is significant improvement in identification accuracy compared to other methods.

1. Introduction

Structural health monitoring (SHM) is the process in which the state of structural health is directly assessed using a nondestructive approach. Damage occurs during service because of the operational cyclic loading, aging, mechanical vibration, changing ambient conditions, shocks, and chemical attack. Hence, the early detection of damage, location, and its severity is very important in the current scenario. Generally, damage identification methods such as acoustic, radiography, magnetic field, and thermal field methods are used for damage detection. All of these techniques are expensive and require that the zone of the damage is known a priori and the structural element being inspected is readily accessible. As an alternative, vibration-based damage detection methods using the inverse concept deserve further investigation.

A crack in a structural element increases the local flexibility, which is a function of crack depth and location. Lee and Shin [2002] identified the location and magnitude of local damage of a beam structure from the dynamic stiffness equation of the beam structure. In that paper, experimentally measured frequency response function data from the damage structure were required as the input data and applicability was limited to cases for which exact dynamic stiffness matrices are obtainable. Yang and Wang [2010] introduced a new damage detection method based on the concept of a natural frequency vector (NFV) and the natural frequency vector assurance criterion (NFVAC), which was verified by both simulative and experimental examples. Wang et al. [2001] suggested a two-stage identification algorithm utilizing changes in natural frequencies and static displacements for identifying structural damage. Liu et al. [2011] identified the presence of structural damage using multiobjective optimization, keeping variations in natural frequency and mode shapes as individual objective functions. Viola et al. [2001] formulated shape functions of a cracked Timoshenko beam element based on the Hamilton principle,

Keywords: crack identification, voltage matching, PZT patches, inverse problem.

with crack sections represented as elastic hinges. A nondestructive evaluation procedure for identifying the magnitude and location of the structure based on experimentally measured frequency and mode shape was developed. Viola et al. [2002] investigated the effect of cracks in the stiffness matrix which neglect the crack closure effect by assuming an open crack.

Patil and Maiti [2005] predicted the location and size of multiple cracks on a slender beam based on experimentally measured frequencies. A strategy to overcome failure in the prediction for cases where one of the cracks is located near an antinode was presented. Douka et al. [2004] investigated the effect of two transverse cracks on the mechanical impedance of a double-cracked cantilever beam both analytically and experimentally. They found significant change of antiresonance frequency due to the presence of cracks, and this additional information was used along with natural frequency changes to identify cracks. Ding et al. [2017] identified multiple cracks using the improved artificial bee colony algorithm (I-ABC) based on an objective function which consists of a limited number of measured natural frequencies. Sekhar [2008] reviewed multiple crack identification in beam, rotor, and pipe structures. The aforementioned study summarized the effects, modeling of cracks, and various vibration identification methods for multiple cracks. Sinha et al. [2002] developed a multicrock model in an Euler–Bernoulli beam based on a small modification of the local flexibility in the vicinity of the crack. In that paper, crack models were incorporated into the finite element model of the structure, and crack location and size were estimated using the model updating from the experimentally measured modal data.

Philips Adewuyi et al. [2009] identified single/multiple damage in beam using the combined measurement of displacement modes from an accelerometer and distributed strain modes with fiber Bragg grating (FBG) sensors. Nandakumar and Shankar [2014] identified multiple crack parameters in the beam using the concept of double-crack transfer matrices with the combined measurements of an accelerometer and a strain gauge. Verhese and Shankar [2014] applied the combined instantaneous power flow balance and conventional acceleration matching concept for the substructural identification of multiple crack parameters of the beam. In the above described method, accelerometers were used as sensors for structural parameter identification.

The high reliability, sensitivity, and electromechanical coupling property of PZT has gained significant attention for potential application as sensors for structural health monitoring. Bendary et al. [2010] formulated a one-dimensional integrated beam element using Hermite cubic and Lagrangian interpolation functions which are carried out for static and dynamic analysis. Zemčík and Sadílek [2007] developed the one-dimensional hybrid PZT element based on the Euler–Bernoulli beam using the bilinear Lagrangian interpolation polynomial for electric potential which is carried out for modal analysis. Later, the same element was used for frequency response analysis and the results were experimentally verified in [Sadílek and Zemčík 2010]. Sulbhewar and Raveendranath [2015] formulated the one-dimensional Euler–Bernoulli beam with PZT structure using a coupled field polynomial that is independent of the material configuration of the piezoelectric beam cross section. A two-stage identification strategy was proposed by Fukunaga et al. [2002] using a limited number of PZT sensors in the time and frequency domain. It identified crack depth up to 10% depth, but it strongly depends on reliable modal data of undamaged structure.

In most of the literature available, accelerometer signals are used for structural identification. However, compared to accelerometers, PZT patches have the advantages of low cost with negligible weight and wide dynamic range. The most notable feature of PZT patches is their miniaturized appearance and ability

to be implanted in civil structures for in situ health monitoring of the structure. Moreover, because of their light weight, PZT patches are not likely to alter the dynamic properties, and their output voltage is less likely to be contaminated with signal noise. In the present proposed method, an integrated beam structure with a PZT sensor is incorporated into the finite element model of the structure and is used for the direct identification of damage at various locations in structure. Damage identification using a one-dimensional piezobeam hybrid model is not reported in the literature. Hence, it is a novel contribution. The objective function consists of the mean square of the deviation between measured and estimated voltage from the PZT patches. Multiple crack identification using the one-dimensional PZT patch model and the effect of patch length are not reported in the literature. The one-dimensional hybrid element is especially convenient and simple for modeling beam-type structures as compared to more complex 3-D PZT patch models. The computational complexity is significantly reduced using a one-dimensional element. The theory is validated with numerical and experimental examples in the sections below.

2. Constitutive equations of PZT

Piezoelectric materials transform mechanical displacement into an electrical field (voltage potential), in which case the piezoelectric material acts as a sensor (direct effect), and its converse effect acts as an actuator. The constitutive equations for the transversely isotropic piezoelectric medium which define the interaction between the stress (σ), strain (ε), electric displacement (D), and electric field (E) are of the form [Benjeddou 2000]

$$\sigma_j = C_{jk}\varepsilon_k - e_{jm}E_m, \quad (1)$$

$$D_l = e_{lj}\varepsilon_k + \epsilon_{lm}E_m, \quad (2)$$

where C_{jk} , ϵ_{lm} , and e_{lj} ($j, k = 1, \dots, 6$ and $l, m = 1, \dots, 3$) are the elastic, dielectric, and piezoelectric coupling coefficients, respectively. The transversely poled piezoelectric material is bonded/embedded in the host structure. The complete coupled three dimensional constitutive equation of a piezoelectric material with principal material axes (x , y and z) can be written as [Sulbhewar and Raveendranath 2015]

$$\begin{bmatrix} \sigma_x \\ \sigma_y \\ \sigma_z \\ \tau_{yz} \\ \tau_{xz} \\ \tau_{xy} \\ D_x \\ D_y \\ D_z \end{bmatrix} = \begin{bmatrix} C_{11} & C_{12} & C_{13} & 0 & 0 & 0 & 0 & 0 & -e_{31} \\ C_{12} & C_{22} & C_{23} & 0 & 0 & 0 & 0 & 0 & -e_{32} \\ C_{13} & C_{23} & C_{33} & 0 & 0 & 0 & 0 & 0 & -e_{33} \\ 0 & 0 & 0 & C_{44} & 0 & 0 & 0 & -e_{24} & 0 \\ 0 & 0 & 0 & 0 & C_{55} & 0 & -e_{15} & 0 & 0 \\ 0 & 0 & 0 & 0 & 0 & C_{66} & 0 & 0 & 0 \\ 0 & 0 & 0 & 0 & e_{15} & 0 & \epsilon_{11} & 0 & e_{32} \\ 0 & 0 & 0 & e_{24} & 0 & 0 & 0 & \epsilon_{22} & 0 \\ e_{31} & e_{32} & e_{33} & 0 & 0 & 0 & 0 & 0 & \epsilon_{33} \end{bmatrix} \begin{bmatrix} \varepsilon_x \\ \varepsilon_y \\ \varepsilon_z \\ \gamma_{yz} \\ \gamma_{xz} \\ \gamma_{xy} \\ E_x \\ E_y \\ E_z \end{bmatrix}, \quad (3)$$

where τ and γ are shear stress and shear strain, respectively.

3. One-dimensional beam geometry

The three-dimensional beam with axes is shown in Figure 1. The Euler–Bernoulli beam theory is applied for a one-dimensional beam with a piezoelectric patch, which neglects the shear effect. The model is

assumed to be plane stress and width in the y -direction is stress free. Therefore, it is possible to set $\sigma_y = \sigma_z = \tau_{xy} = \tau_{xz} = \tau_{yz} = \gamma_{xy} = \gamma_{xz} = \gamma_{yz} = 0$ while $\varepsilon_y \neq 0$, $\varepsilon_z \neq 0$ [Sulbhewar and Raveendranath 2015]. The polarization axis z is aligned with the thickness direction of the beam, thus only D_z is taken and for electric field $E_x = E_y = 0$. Applying these conditions, (3) is reduced to the form

$$\begin{bmatrix} \sigma_x \\ D_z \end{bmatrix} = \begin{bmatrix} \hat{C} & -\hat{e} \\ \hat{e} & \hat{\epsilon} \end{bmatrix} \begin{bmatrix} \varepsilon_x \\ E_z \end{bmatrix}, \quad (4)$$

where $\hat{C} = Q_{11} - Q_{12}^2/Q_{22}$ and $Q_{ij} = C_{ij} - C_{i3}C_{j3}/C_{33}$ ($i, j = 1, 2$); $\hat{e} = \bar{e}_{31} - \bar{e}_{32}(Q_{12}/Q_{22})$ and $\bar{e}_{3i} = e_{3i} - e_{33}(C_{13}/C_{33})$ ($i = 1, 2$); $\hat{\epsilon} = \bar{\epsilon}_{33} + \bar{e}_{32}^2/Q_{22}$ and $\bar{\epsilon}_{33} = \epsilon_{33} + e_{32}^2/C_{33}$ [Kapuria and Hagedorn 2007]. Here, \hat{C} , $\hat{\epsilon}$, and \hat{e} are the reduced elastic, dielectric, and piezoelectric coupling coefficients respectively and the calculated values are shown in Table 1. This reduced property is used for further numerical study of the one-dimensional (1-D) beam with a PZT patch in MATLAB.

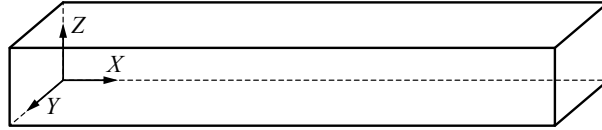


Figure 1. Three-dimensional beam.

<i>material</i>	<i>properties</i>	
aluminum	$E = 71 \text{ GPa}$	$\nu = 0.3 \quad \rho = 2210 \text{ kg} \cdot \text{m}^{-3}$
PZT 5H	$C_{11} = C_{22} = 126 \text{ GPa}$	$C_{12} = 79.5 \text{ GPa}$
	$C_{13} = C_{23} = 84.1 \text{ GPa}$	$C_{33} = 117 \text{ GPa}$
	$C_{44} = C_{55} = 23 \text{ GPa}$	$C_{66} = 23.25 \text{ GPa}$
	$e_{31} = e_{32} = -6.5 \text{ C} \cdot \text{m}^{-2}$	$e_{33} = 23.3$
	$e_{15} = e_{24} = 17 \text{ C} \cdot \text{m}^{-2}$	$\epsilon_{11} = \epsilon_{22} = 1.503 \times 10^{-8} \text{ F} \cdot \text{m}^{-1}$
	$\epsilon_{33} = 1.3 \times 10^{-8} \text{ F} \cdot \text{m}^{-1}$	$\rho = 7500 \text{ kg} \cdot \text{m}^{-3}$
reduced properties	$\hat{C} = 60.013 \text{ GPa}$	$\hat{e} = -16.4921 \text{ C} \cdot \text{m}^{-2} \quad \hat{\epsilon} = 2.5885 \times 10^{-8} \text{ F} \cdot \text{m}^{-1}$

Table 1. Material properties of the beam.

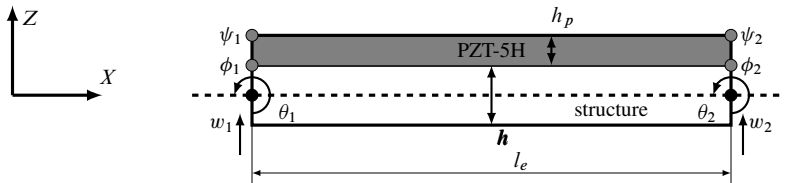


Figure 2. One-dimensional beam element: PZT and supporting structure sharing common nodes.

4. FEM formulation and elemental matrices

The one-dimensional beam formulation has been presented in [Sadřlek and Zemčřık 2010; Sulbhewar and Raveendranath 2015], but not used for time domain dynamic response with damping and inverse problems. The finite element formulation of the structure is briefly explained here. The beam element is based on the Euler–Bernoulli theory and the element has two nodes. Two independent polynomials are used for interpolation of mechanical and electrical field variables. First, the Hermite cubic polynomial is used for the interpolation of mechanical quantities of vertical displacement (w) and rotation (θ) as shown in Figure 2. The vertical displacement (w) is approximated across the length as

$$w(x) = a_0 + a_1x + a_2x^2 + a_3x^3 = [N_w]\{w^e\}, \quad (5)$$

where N_w is the shape interpolation function of the structural part and structural nodal degree of freedom per element is arranged as $w^e = [w_1, \theta_1, w_2, \theta_2]^T$. The bending strain is

$$\varepsilon(x, z) = \frac{\partial u}{\partial x} = -z \frac{\partial^2 w}{\partial x^2} = [B_w]\{w^e\}, \quad (6)$$

where $[B_w]$ is the strain-displacement matrix consisting of derivatives of shape functions.

The electric potential is $\phi(x, z)$, considered as a function of the thickness and the length of the beam. Hence, let Langrangian bilinear function be estimated for the interpolation as

$$\phi(x, z) = a_4 + a_5x + a_6z + a_7xz = [\Phi_\phi]\{\phi^e\}. \quad (7)$$

Here, ϕ and ψ are the lower and upper electrical potentials of PZT surface. The electrical nodal degrees of freedom per element can be ordered as $\{\phi^e\} = [\phi_1, \psi_1, \phi_2, \psi_2]^T$. The electric field $E(x, z)$ can be written as

$$E(x, z) = [B_\phi]\{\phi^e\}, \quad (8)$$

where $[B_\phi]$ is the electrical field potential matrix consisting of derivatives of shape functions.

Here, a homogeneous electrical boundary condition is imposed on the bottom surface of PZT patch to eliminate rigid body modes, i.e., the lower surface is grounded with $\phi = 0$ V, while the upper surface is left open. The dynamic potential energy density G for the piezoelectric medium can be written as [Xu and ShengPeng 2013]

$$G = \frac{1}{2}\varepsilon^T c \varepsilon - \frac{1}{2}E^T \epsilon E - \varepsilon^T e E. \quad (9)$$

The elemental matrices are calculated by applying the variational principle to potential, kinetic energy, and external forces (mechanical and electrical loading). This must be satisfied for any arbitrary variation of the displacements and electrical potentials and thus the equations of motion of elemental matrices with damping can be represented as

$$\begin{bmatrix} [M_{ww}^e] & [0] \\ [0] & [0] \end{bmatrix} \begin{Bmatrix} \{\ddot{w}^e\} \\ \{\ddot{\phi}^e\} \end{Bmatrix} + \begin{bmatrix} [C_{ww}^e] & [0] \\ [0] & [0] \end{bmatrix} \begin{Bmatrix} \{\dot{w}^e\} \\ \{\dot{\phi}^e\} \end{Bmatrix} + \begin{bmatrix} [K_{ww}^e] & [K_{w\phi}^e] \\ [K_{w\phi}^e]^T & [K_{\phi\phi}^e] \end{bmatrix} \begin{Bmatrix} \{w^e\} \\ \{\phi^e\} \end{Bmatrix} = \begin{Bmatrix} \{F^e\} \\ \{Q^e\} \end{Bmatrix}. \quad (10)$$

The damping matrix $[C_{ww}^e]$ is defined as a proportional damping, i.e., $[C_{ww}^e] = \alpha[M_{ww}^e] + \beta[K_{ww}^e]$ and α, β are Rayleigh's damping coefficients. Equation (10) is the elemental equilibrium in the discretized form, where $[M_{ww}^e]$ is the mass matrix, and $[K_{ww}^e]$, $[K_{w\phi}^e]$, and $[K_{\phi\phi}^e]$ are the stiffness matrices corresponding

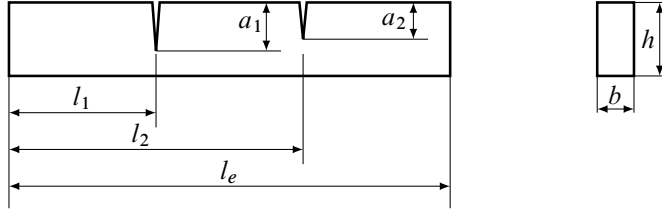


Figure 3. Beam element with two cracks.

to the mechanical coupling, electromechanical coupling, and electrical degrees of freedom, respectively. $\{F^e\}$ and $\{Q^e\}$ are the mechanical and electrical charge load vectors, respectively. The size of the element matrices are $[4 \times 4]$ and are given by

$$\begin{aligned} [M_{ww}^e] &= \int_V [N_w]^T \rho [N_w] dV, & [K_{ww}^e] &= \int_V [B_w]^T \hat{C} [B_w] dV, \\ [K_{w\phi}^e] &= \int_V [B_w]^T \hat{e} [B_\phi] dV, & [K_{\phi\phi}^e] &= \int_V [B_\phi]^T \hat{\epsilon} [B_\phi] dV. \end{aligned} \quad (11)$$

In order to solve this, the global matrix equation (10) can be expanded and written as

$$\begin{aligned} [M_{ww}]\{\ddot{w}\} + [C_{ww}]\{\dot{w}\} + [K_{ww}]\{w\} + [K_{w\phi}]\{\phi\} &= \{F\}, \\ [K_{w\phi}]^T\{w\} + [K_{\phi\phi}]\{\phi\} &= \{Q\}. \end{aligned} \quad (12)$$

The second part of (12) is simplified as

$$\{\phi\} = [K_{\phi\phi}]^{-1}\{Q\} - [K_{\phi\phi}]^{-1}[K_{w\phi}]^T\{w\}. \quad (13)$$

The above equation is substituted in the first part of (12) and is written as

$$[M_{ww}]\{\ddot{w}\} + [C_{ww}]\{\dot{w}\} + [K_{ww}]^*\{w\} = \{F\}^*, \quad (14)$$

where

$$\begin{aligned} [K_{ww}]^* &= [K_{ww}] - [K_{w\phi}][K_{\phi\phi}][K_{w\phi}]^T, \\ \{F\}^* &= \{F\} - [K_{w\phi}][K_{\phi\phi}]^{-1}\{Q\}. \end{aligned} \quad (15)$$

For the sensor problem, displacement histories are obtained by solving (14), and by substituting into (13), the voltage vector across the sensor patch is obtained.

5. FEM formulation of beam element with multiple cracks

5.1. Double crack per beam element model. The finite element formulation of the double crack per element model is explained here and it is identified as two cracks per beam element. This has hitherto not been incorporated in a one-dimensional PZT patch model, and also its application in an inverse problem of crack identification is novel. The crack per beam element and corresponding finite element model are shown in Figures 3 and 4 respectively. Let l_e be the length of the element, l_1 and l_2 are the locations of the crack from its left end, a_1 and a_2 respectively are the crack depths measured from the top of the beam.

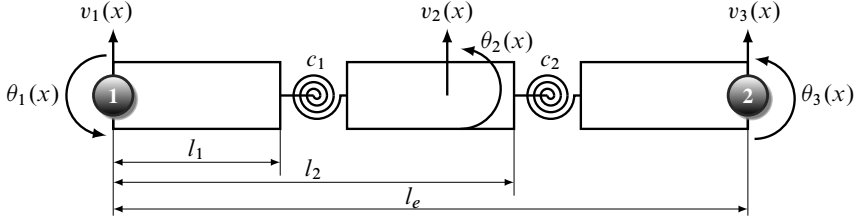


Figure 4. Equivalent model of cracked beam element.

The finite element model of two cracks per beam element contains three segments connected by two massless hinges of flexibility c_1 and c_2 , respectively, as shown in Figure 4. Three different polynomials are assumed for the field variables of this element since it has three different segments:

$$\left. \begin{aligned} v_1(x) &= b_1 + b_2x + b_3x^2 + b_4x^3 \\ \theta_1(x) &= v_1'(x) = b_2 + 2b_3x + 3b_4x^2 \end{aligned} \right\} 0 \leq x \leq l_1; \\
 \left. \begin{aligned} v_2(x) &= b_5 + b_6x + b_7x^2 + b_8x^3 \\ \theta_2(x) &= v_2'(x) = b_6 + 2b_7x + 3b_8x^2 \end{aligned} \right\} l_1 \leq x \leq l_2; \\
 \left. \begin{aligned} v_3(x) &= b_9 + b_{10}x + b_{11}x^2 + b_{12}x^3 \\ \theta_3(x) &= v_3'(x) = b_{10} + 2b_{11}x + 3b_{12}x^2 \end{aligned} \right\} l_2 \leq x \leq l_e;
 \end{aligned} \quad (16)$$

where b_1 – b_{12} are the polynomial constants. The following are the nodal values and conditions applied to the cracked beam element:

$$\begin{aligned} v_1(0) &= Y_1, \quad \theta_1(0) = \Theta_1, \quad v_3(l_e) = Y_2, \quad \theta_3(l_e) = \Theta_2, \\ v_1(l_1) &= v_2(l_1), \quad v_1'(l_1) = v_2'(l_1), \quad v_1''(l_1) = v_2''(l_1), \\ v_2(l_2) &= v_3(l_2), \quad v_2'(l_2) = v_3'(l_2), \quad v_2''(l_2) = v_3''(l_2), \\ v_2''(l_1) &= \frac{1}{K_{c_1}}(\theta_2(l_1) - \theta_1(l_1)), \quad v_3''(l_2) = \frac{1}{K_{c_2}}(\theta_3(l_2) - \theta_2(l_2)). \end{aligned}$$

The flexibility coefficients $K_{c_1} = EIc_1$ and $K_{c_2} = EIc_2$ at crack locations. EI is the flexural stiffness and c is the torsional flexibility of the crack; Y_1 , Θ_1 , Y_2 , and Θ_2 are the displacement and rotation at the nodes 1 and 2 respectively. The flexibility coefficient at the crack location can be also expressed as [Viola et al. 2001]

$$K_{c1,c2} = hf(\xi)/2, \quad (17)$$

where $f(\xi)$ is a correction function which takes into account the body and crack geometry and depends on the dimensionless crack ratio $\xi_{1,2} = a_{1,2}/h$ which can be represented as follows [Viola et al. 2001]:

$$\begin{aligned} f(\xi) &= \xi^2(12 - 19.5\xi + 70.1\xi^2 - 97.6\xi^3 + 142\xi^4 - 138\xi^5 + 128\xi^6 - 132\xi^7 \\ &\quad + 379\xi^8 - 417\xi^9 + 131\xi^{10} + 313\xi^{12} - 357\xi^{13} + 102\xi^{14}), \quad 0 \leq \xi < 0.5; \\ f(\xi) &= \frac{1.32}{(1 - \xi^2)} - 1.78, \quad 0.5 \leq \xi \leq 1. \end{aligned} \quad (18)$$

The shape function matrix $[N(x)]$ of size 6×4 relates the nodal DOF with the field variables as follows:

$$\begin{Bmatrix} v_1(x) \\ \theta_1(x) \\ v_2(x) \\ \theta_2(x) \\ v_3(x) \\ \theta_3(x) \end{Bmatrix} = \begin{bmatrix} N_{11}(x) & N_{12}(x) & N_{13}(x) & N_{14}(x) \\ N_{21}(x) & N_{22}(x) & N_{23}(x) & N_{24}(x) \\ N_{31}(x) & N_{32}(x) & N_{33}(x) & N_{34}(x) \\ N_{41}(x) & N_{42}(x) & N_{43}(x) & N_{44}(x) \\ N_{51}(x) & N_{52}(x) & N_{53}(x) & N_{54}(x) \\ N_{61}(x) & N_{62}(x) & N_{63}(x) & N_{64}(x) \end{bmatrix} \begin{Bmatrix} Y_1 \\ \Theta_1 \\ Y_2 \\ \Theta_2 \end{Bmatrix}. \quad (19)$$

From the finite element procedure, the stiffness and mass matrices of the cracked element can be obtained as

$$[k_{cr}^e] = EI \left(\int_0^{l_1} B_1^T B_1 dx + \int_{l_1}^{l_2} B_2^T B_2 dx + \int_{l_2}^{l_e} B_3^T B_3 dx \right), \quad (20)$$

$$[m_{cr}^e] = \rho A \left(\int_0^{l_1} N_1(x)^T N_1(x) dx + \int_{l_1}^{l_2} N_3(x)^T N_3(x) dx + \int_{l_2}^{l_e} N_5(x)^T N_5(x) dx \right). \quad (21)$$

where $B_1 = d^2[N_1(x)]/dx^2$, $B_2 = d^2[N_3(x)]/dx^2$, and $B_3 = d^2[N_5(x)]/dx^2$. Here, $N_1(x)$, $N_2(x)$, $N_3(x)$, $N_4(x)$, $N_5(x)$, and $N_6(x)$ are the respective rows of the shape function matrix $N(x)$. Since the effect of rotation of the beam element is very small when compared with translation of beam, it may be neglected. This can be extended to any number of cracks per element. When either K_{c1} or K_{c2} is zero, the element becomes a single crack per element model as in previous literature [Krawczuk et al. 2000; Viola et al. 2001]. The single crack per element with one-dimensional PZT patch in structural identification (SI) has not yet been reported. When the values of $K_{c1} = K_{c2} = 0$, the structure is considered as an intact element.

6. Particle swarm optimization (PSO) algorithm

A heuristic optimization technique referred to as particle swarm optimization PSO is used here which mimics the social behavior of swarms. It was first proposed by James and Eberhart [Kennedy and Eberhart 1995]. Heuristic methods are preferred over calculus-based methods due to their robustness and ability to attain the global optima. It imitates the social behavior of a swarm of birds. Each bird tends to follow the general swarm direction in search of the target (food), but it has a component of its own intelligence and memory (i.e., local search) which influences its action. Each bird is visualized as a ‘‘particle’’ which approaches the target (i.e., the global optima) with a ‘‘velocity’’. The number of particles (i.e., population) and their initial random positions are specified. As the particles progress to the global optima through many generations, their current position is updated using two parameters: G_{best} , which represent the historically best coordinate of all the particles in the population, and $P_{best,i}$, the historically best coordinate of the i -th particle. The equations giving the velocity v and position x for the i -th particle in the $k + 1$ generation are given by

$$v_i(k+1) = \varphi(k)v_i(k) + \alpha_1[\gamma_{1i}(P_{best,i} - x_i(k))] + \alpha_2[\gamma_{2i}[(G_{best} - x_i(k))], \quad (22)$$

$$x_i(k+1) = x_i(k) + v_i(k+1), \quad (23)$$

where i is the particle index, k the discrete time index, v the velocity of the i -th particle, and x the position of the i -th particle in the present solution. Here, γ_1 and γ_2 represent two random numbers between zero

and one, φ is an inertia term uniformly decreasing from 0.9 to 0.4 with passing generations, and α_1 and α_2 are two acceleration constants set to two [Perez and Behdinan 2007]. Several studies have pointed out the superiority of the PSO algorithm over the more conventional heuristic algorithms such as the genetic algorithm (GA) for inverse problem applications [Mohan et al. 2014; Mouser and Dunn 2005].

7. Crack identification using one-dimensional PZT patch

In the proposed method, a patch is attached to either end of the beam member whose crack parameters have to be identified. The time-domain-based approach is used and the voltage history of the patch is used as the main response quantity in the identification of structural stiffness and crack parameters. A few experimentally measured voltage potential responses ϕ^m are measured from PZT patches. The estimated voltage potential ϕ^e is obtained from the mathematical model using (13). For exact identification, ϕ^e has to match with the experimentally measured responses ϕ^m . In this method, experimental responses are simulated from a known numerical model and polluted with Gaussian noise of zero mean and a certain standard deviation. Using the particle swarm optimization (PSO) algorithm, the following fitness (objective) function is minimized, which is the sum of squares of deviations between the measured and estimated voltage. The fitness or objective function is

$$f = \frac{\sum_{i=1}^M \sum_{j=1}^L |\phi^m(i, j) - \phi^e(i, j)|^2}{ML} \tag{24}$$

The superscripts m and e denote measured and estimated responses for fitness evaluation, M is the number of measurement sensors used, and L is the number of time steps. Ideally, it must be minimized to zero, but usually it approaches a value close to zero. The minimization of the fitness function gives the identified crack depth and location variables.

8. Numerical examples and results

Here, three different types of numerical studies are carried out for validating the proposed identification method. A fixed-fixed beam with two cracks (assuming a single crack per element), the same beam with four cracks, and substructures (SS) of the frame structure with nine members and four cracks (assuming two cracks per element). A patch is attached to either end of the beam member. The structural parameters, such as mass and stiffness of the undamaged structure, are assumed to be known. Experimental measured responses are numerically simulated from a fully defined model in MATLAB using Newmark’s constant acceleration scheme. The structure is excited by an impulse or harmonic force and the corresponding voltage responses are measured at the PZT patches. The crack parameters such as location and depth are estimated using the inverse formulation with a single objective approach. In order to simulate the effect of noise in experiments, a Gaussian random noise level of 5% (standard deviation) and zero mean is added to all the measured signals. The noise is added with simulated responses in such a way that

$$\text{Noise} = g \times \text{RMS}_{\text{signal}} \times NL \tag{25}$$

where g is the standard Gaussian variable, $\text{RMS}_{\text{signal}}$ is the root mean square (RMS) value of the numerically simulated signal, and NL is noise level.

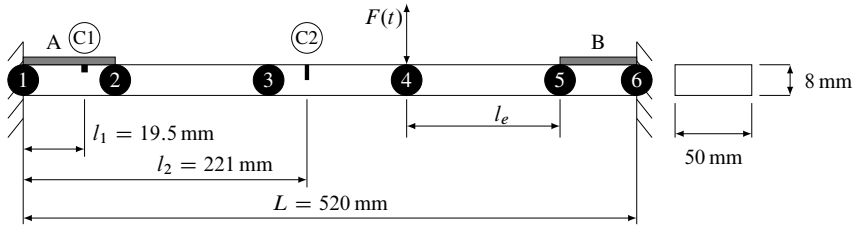


Figure 5. Finite element model of two single cracks per beam element with PZT patch.

In this numerical study, three different PZT patch lengths are investigated, and they are PZT : 5%, PZT : 10%, and PZT : 20%. They respectively represent the length of the patch expressed as percentage of beam length. The width of PZT is the same as the host structure and a constant thickness of 1 mm is used for this study.

8.1. Example 1: fixed-fixed beam with multiple cracks using single crack per element. The crack detection by the proposed method is applied on the fixed-fixed beam structure to determine the magnitude (crack depth) and locations of two cracks simultaneously. The same cracked steel beam was studied in [Verhese and Shankar 2014; Viola et al. 2001]: it is 520 mm long, 50 mm wide, and 8 mm thick with a Young's modulus (E) of 206 GPa and density of 7850 kg/m^3 . The two open edge cracks are assumed to be located at 19.5 mm and 221 mm from the left end of beam, respectively, and it is also assumed that the cracks in different elements do not interact with each other. The absolute normalized crack location measured from the left end of the beam are $\lambda_{C1}(l_1/L) = 0.0375$ and $\lambda_{C2}(l_2/L) = 0.425$. Crack depths of 0.4 mm and 4 mm are considered and the corresponding normalized crack depths are $\xi_{C1}(a/h) = 0.05$ and $\xi_{C2}(a/h) = 0.5$ respectively. The beam is divided into five Euler finite elements as shown in Figure 5 and cracks lie in the first and third elements. It may be noted that the first crack is located under the PZT patch.

In this study, as in the first case, two PZT patches with size PZT : 5%, i.e., $(26 \times 50 \times 1 \text{ mm}^3 \text{ PZT})$ is bonded on either end of the structure as shown in Figure 5. The first and second natural frequency of the modes of vibration of the cracked structure are 151.29 Hz and 430.97 Hz respectively. Rayleigh damping with a modal damping ratio of 3% is used for the first two modes of vibration. The beam is subjected to a harmonic excitation of $F(t) = 2.5 \sin(2\pi 130t)$ N in the vertical (upward) direction at node 4. The displacement, velocity, and acceleration time history data are calculated for each nodal point using Newmark's method with a constant time step of 0.001 s. Using the displacement response history, voltage responses are measured through two PZT patches. Figure 6 shows the undamaged and damaged responses available at the measurement PZT patch sensor A for multiple crack locations. The shift in damaged response for multiple cracks is greater than a single crack. The numerically calculated voltages are polluted by artificially adding Gaussian white noise with zero mean and a standard deviation of 5% to simulate experimental errors.

The mass and intact stiffness EI of the structure are assumed to be known a priori. The proposed algorithm identifies multiple cracks assuming that each element contains a single crack. The normalized crack location in element 1 with respect to left end of the element is $\lambda_{e1} = 0.75$ and the same in element 3 is $\lambda_{e3} = 0.25$. Here, crack magnitude and location are set as the unknown variables for each element and

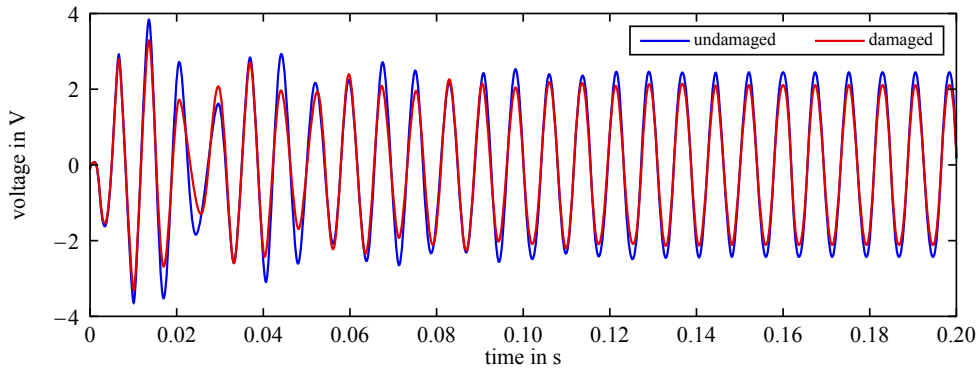


Figure 6. Harmonic response at measurement (PZT A) with multiple crack locations.

patch length	crack depth ξ (exact)	crack location λ (exact)	crack depth ξ (identified)		crack location λ (identified)	
			noise-free (% error)	5% noise (% error)	noise-free (% error)	5% noise (% error)
PZT: 5%	0.05 (C1)	0.0375	0.0478 (4.4)	0.0535 (7)	0.0382 (-1.87)	0.0385 (-2.67)
	0.5 (C2)	0.425	0.4967 (0.66)	0.5062 (-1.24)	0.4245 (-0.12)	0.4298 (-1.13)
PZT: 10%	0.05 (C1)	0.0375	0.0519 (-3.8)	0.0469 (6.2)	0.0369 (1.6)	0.0383 (-2.13)
	0.5 (C2)	0.425	0.5031 (-0.62)	0.4951 (1.18)	0.4255 (0.12)	0.4208 (0.99)
PZT: 20%	0.05 (C1)	0.0375	0.0483 (3.4)	0.0529 (-5.8)	-0.0380 (1.33)	0.0368 (1.87)
	0.5 (C2)	0.425	0.4978 (0.44)	0.5055 (-1.1)	0.4253 (-0.07)	0.4292 (0.96)

Table 2. Crack damage magnitude and location with voltage matching. All values are normalized.

hence there are ten unknown variables in this problem. Thus the optimization variables to be identified are the normalized crack depth ξ and normalized location $\lambda_e = l_1/l_e$ in five elements. The experimentally measured voltage response of PZT patches is required for the fitness evaluation. The mean square error (MSE) between measured and predicted voltage response at PZT patches are minimized by particle swarm optimization. The lower and upper bounds for PSO optimization for identifying crack magnitude are set at zero and one. Similarly the lower and upper bounds to identify normalized crack locations are set as zero and l_e , respectively. Here, PSO parameters are set to 100 particles (swarm size) and 500 generations. Similar numerical studies are carried out with larger patch lengths, such as PZT: 10%, i.e., ($52 \times 50 \times 1 \text{ mm}^3$ PZT) and PZT: 20%, i.e., ($104 \times 50 \times 1 \text{ mm}^3$ PZT). The crack depth and location are estimated using different sets of iterations and the mean identified crack parameters are presented in Table 2.

The smallest crack depth $\xi = 0.05$ located under the PZT patch is identified with an absolute error of 7%, 6.2%, and 5.8%, respectively for PZT: 5%, PZT: 10%, and PZT: 20% with noisy condition. From Table 2, it can be seen that crack location identification is better than crack depth estimation. Here, the smallest patch length (PZT: 5%) identified the crack location with an absolute error of 2.67% under the noisy condition. The element-wise details of crack depth identification using different patch lengths are shown in Figure 7 for the noise-free and noisy cases. Figure 8 shows the comparison of convergence

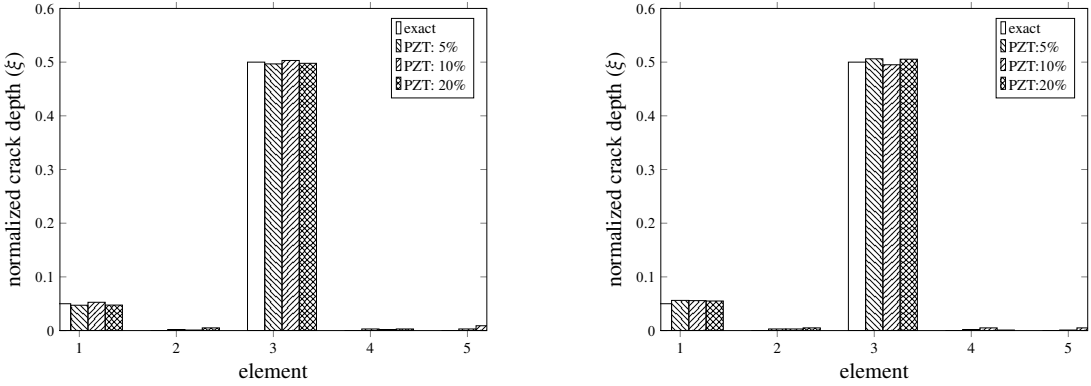


Figure 7. Normalized damage magnitude of multiple cracks. Left: noise-free case. Right: 5% noise case.

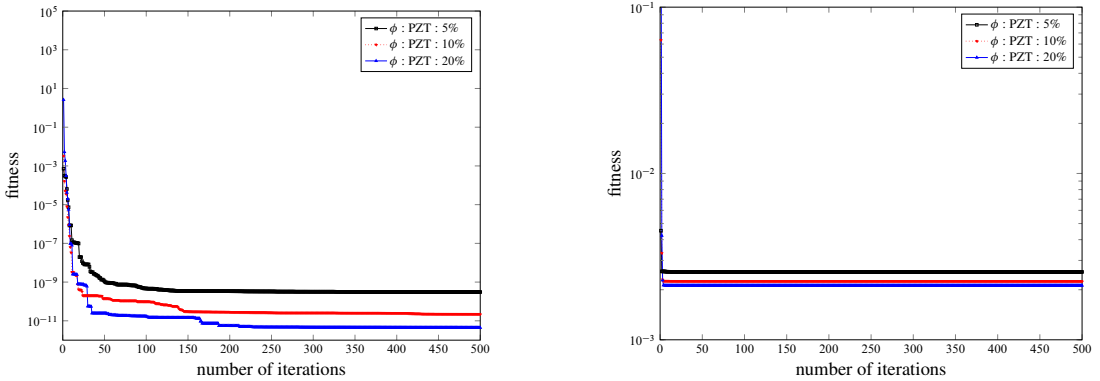


Figure 8. Convergence plot for $\xi = 0.05$. Left: noise-free case. Right: 5% noise case.

studies of different PZT patch lengths. Here, the objective function of PZT: 20% has minimized better than smaller patch lengths and is most accurate in identification. However, it is not required to use such a large patch length. As compared to PZT: 5%, the percentage decrease of error by PZT: 20% is only 8–15%. Thus for practical and economical aspects, PZT: 5% is sufficient for estimating crack parameters.

Now, the proposed method is compared with similar existing published results. Viola et al. [2002] identified the crack depth $\xi = 0.5$ and location $\lambda = 0.76$ based on the modal approach using experimentally measured results. The identified crack parameters are 0.486 and 0.756 and the percentage of the absolute error is 2.8% and 0.53% respectively for crack depth and location. It may be noted that here only a single crack is identified. The very same multicrack problem of similar crack depth $\xi = 0.5$ was solved by Verhese and Shankar [2014] using a combined transient power flow and acceleration matching technique with a substructure approach. There, normalized crack depth and location of the same crack depth were identified with absolute errors of 3.26%, 4.04%, and 1.59%, 2.98% respectively for the noise-free and 5% noisy cases. The proposed method using PZT : 5% estimated the crack depth and location of a similar crack with errors of 0.66%, 1.24%, and 0.117%, 1.13%, respectively for the noise-free and noisy cases. Here, mean computational time is only about 140 s whereas in the other study it was 3000 s.

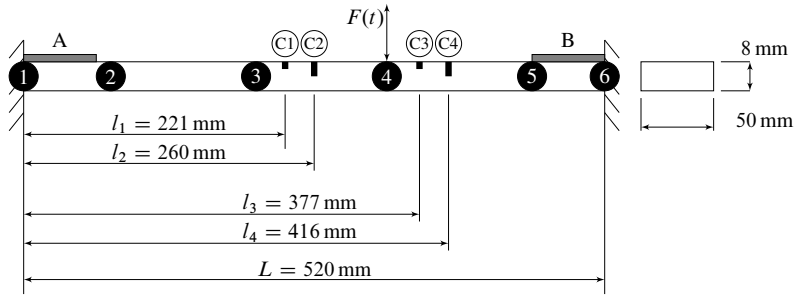


Figure 9. Finite element model of two double cracks per beam element with PZT patch.

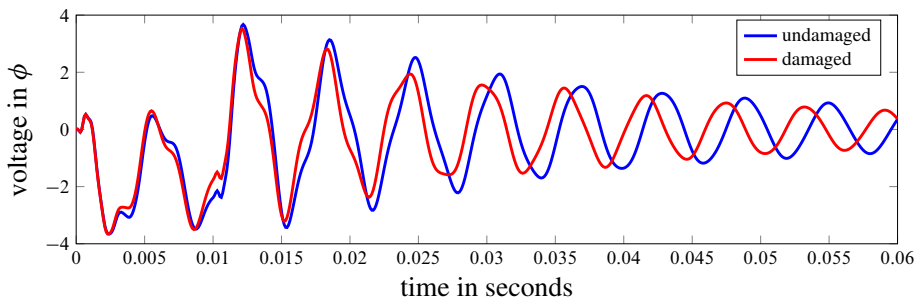


Figure 10. Impulse response at measurement (PZT A) with multiple double crack locations.

8.2. Example 2: fixed-fixed beam with two double crack per element. The same beam in Section 8.1 is considered for the crack identification with a double crack per beam element. Here, four open edge cracks of depths 0.4 mm, 4 mm, 0.8 mm, and 2 mm are assumed to be located at a distances of 221 mm, 260 mm, 377 mm, and 416 mm respectively from the fixed end. In this study, the beam is divided into five elements; two open edge cracks C_1, C_2 are placed in element 3, and C_3, C_4 are placed in element 4, as shown in Figure 9. It is assumed that cracks are not interacting with each other. The normalized crack depths ($\xi = a/h$) are $\xi_{C1} = 0.05$, $\xi_{C2} = 0.5$, $\xi_{C3} = 0.1$, and $\xi_{C4} = 0.25$ and the corresponding absolute crack locations are $\lambda_{C1} = 0.425$, $\lambda_{C2} = 0.5$, $\lambda_{C3} = 0.725$, and $\lambda_{C4} = 0.8$.

In this study, PZT: 5% and PZT: 10% are used for the crack parameter estimation. As in the first case, two PZT patches of size PZT: 5% are bonded on either side of the structure as shown in Figure 9. Here, the normalized crack locations in the element 3 with respect to left end of the element are $\lambda_{e31} = 0.25$ and $\lambda_{e32} = 0.5$, and the same in the element 4 are $\lambda_{e41} = 0.25$ and $\lambda_{e42} = 0.5$. (Here, λ_{e31} represents crack 1 in element 3, i.e., C_1 .)

The fundamental natural frequency of the cracked structure is 150.87 Hz. Rayleigh damping with the modal damping ratio of 3% is used for the first two modes of vibration. The beam is excited by providing an impulse force of 5 N at node 4 over a time of 0.01 s in a time step of 0.001 s and a voltage response is measured through PZT patches. Figure 10 shows the comparison between the damaged and undamaged response of the beam at the PZT patch A and the change in dynamic response is greater than a single crack.

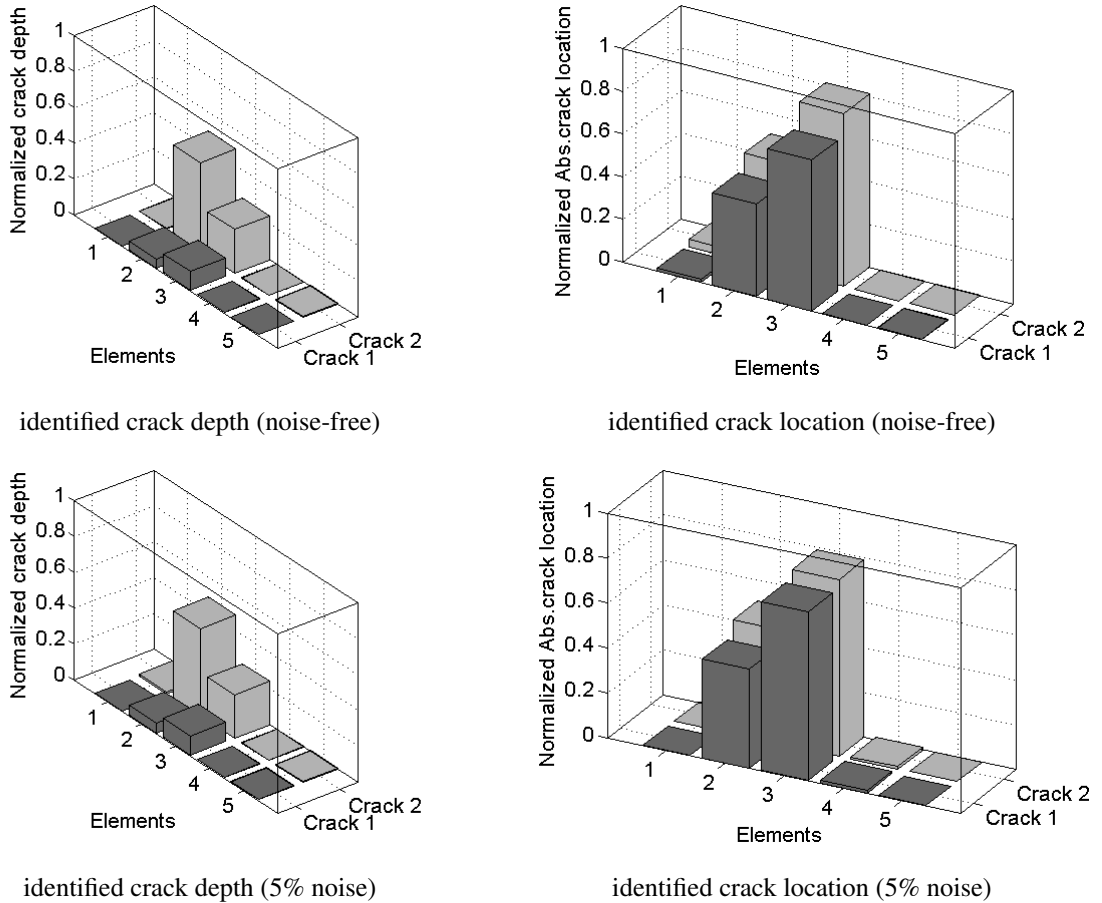


Figure 11. Identified crack parameters of fixed-fixed beam with PZT: 5%.

Here, for crack parameter estimation, it is assumed that each finite element of the model contains two cracks at different positions. Crack magnitude and location are unknown variables and thus each element contains four unknown variables. Hence, a total of twenty variables are searched between the value of zero to one by PSO. The MSE between the measured and predicted voltage responses is minimized by PSO with a swarm size of 100 and with 500 iterations. The identified parameters with PZT: 5% is shown in Figure 11 and the percentage of absolute error of identified parameters of each crack is shown in Figure 12. The smallest crack of depth ($\xi = 0.05$) is identified with an absolute error of 4.89% for noise-free measurement and 9.05% with 5% noise level measurement. The normalized location of the same crack is identified with an error of 1.76% without noise and 3.36% with 5% noise in measurements.

The numerical study was carried out for PZT: 10% with similar crack depth and location for the same beam. Figure 13 shows the comparison of convergence of fitness (objective) functions for PZT: 5% and PZT: 10% for four cracks (noise-free and noisy case), respectively. The better minimization of PZT: 10% when compared with PZT: 5% is seen from the plot. Hence, the error of both magnitude and location is reduced. The identified parameters are shown in Figure 14 and absolute errors in those parameters are

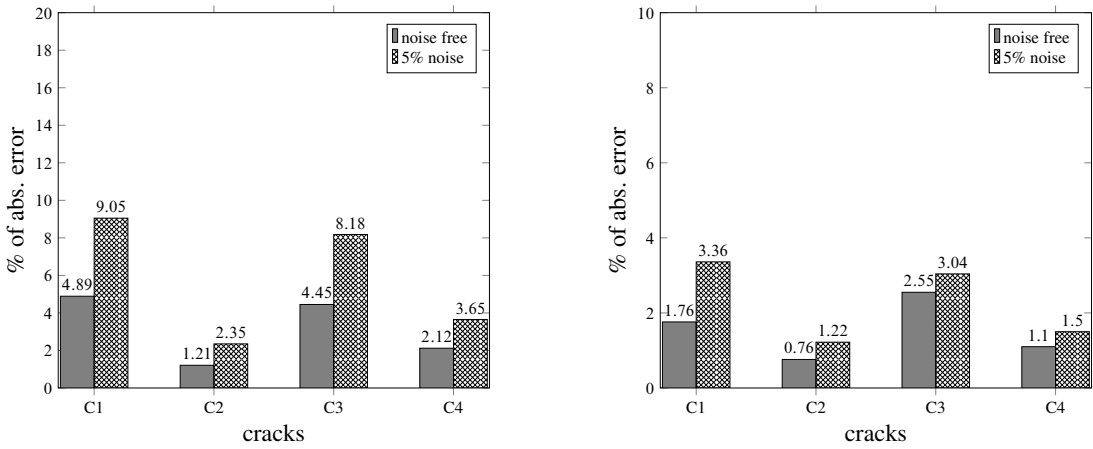


Figure 12. Absolute error in identified parameters in fixed-fixed beam with PZT: 5%. Left: depth. Right: location.

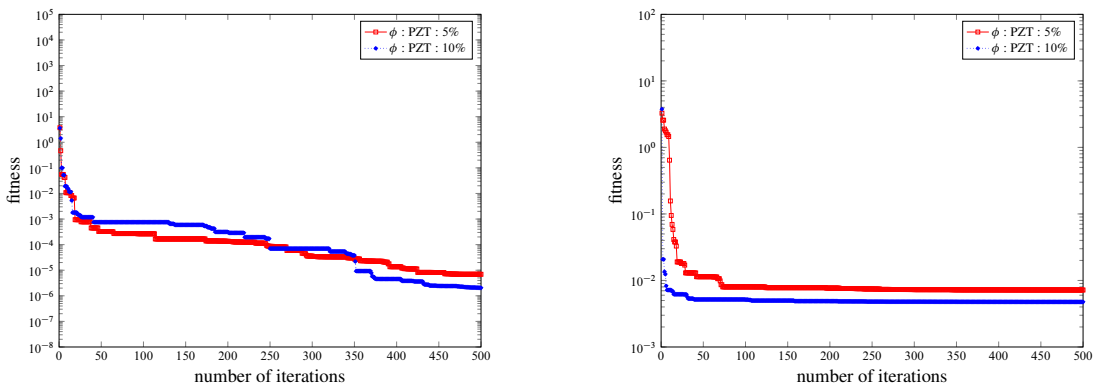


Figure 13. Convergence plot for multiple cracks with two double-cracks per beam element. Left: noise-free case. Right: 5% noise case.

shown in Figure 15. In this case, the smallest crack depth ($\xi = 0.05$) is identified with an absolute error of 4.03% with noise-free measurement and 8.75% with 5% noise level measurement. The error in its location is 1.5% without noise and 3.21% with 5% noise. Here, due to an increase in sensitivity, it can be observed that there is an improvement in identification of smaller crack depth and location. It is also seen that both patch lengths identified the location more accurately than crack depth.

8.3. Example 3: substructure (SS) of frame with double crack per beam element. In this example, a steel frame structure consisting of nine members is fixed at two supports, as shown in Figure 16 as per [Nandakumar and Shankar 2014]. The density of the frame material is 7850 kg/m³ and its Young’s modulus (E) is 200 GPa. Each member has a flexural rigidity (EI) of 43.2 N · m², and a cross-section of 12 × 6 mm. Four open edge cracks of depth 0.3 mm, 1.5 mm, 3 mm, and 2 mm are considered at a distances of 200 mm, 275 mm, 725 mm, and 800 mm respectively from the left end of member 4, as shown in Figure 16. The fundamental natural frequency of the cracked structure is 11.9 Hz. The normalized

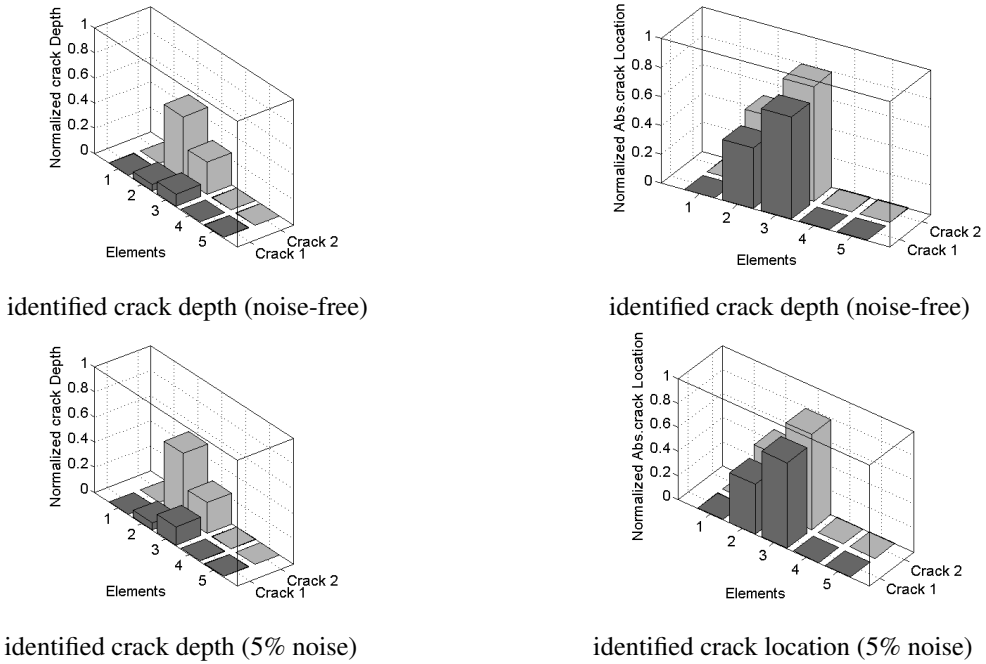


Figure 14. Identified crack parameters of fixed-fixed beam with PZT: 10%.

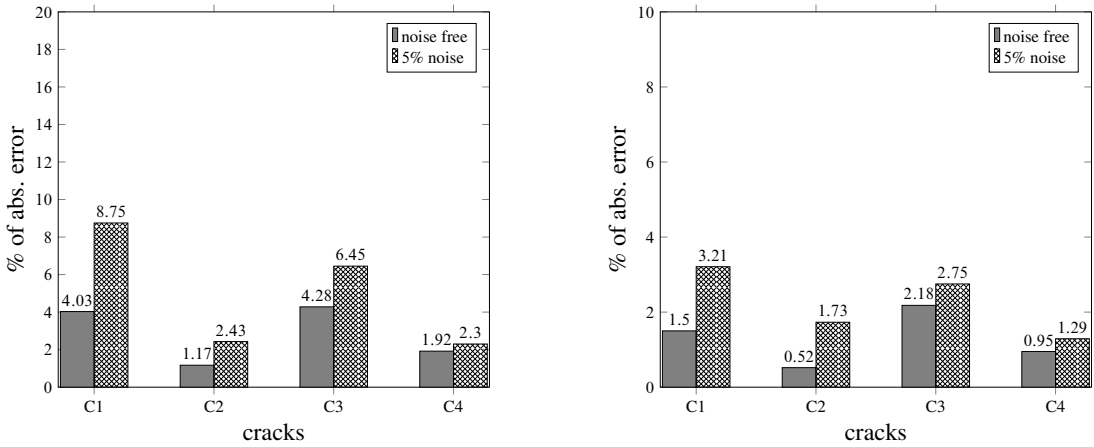


Figure 15. Absolute error in identified parameters in fixed-fixed beam with PZT: 10%. Left: depth. Right: location.

crack depths for the above cracks are $\xi_{c1} = 0.05$, $\xi_{c2} = 0.25$, $\xi_{c3} = 0.5$, and $\xi_{c4} = 0.33$ and their absolute normalized locations from the left end of member 4 are $\lambda_{c1} = 0.2$, $\lambda_{c2} = 0.275$, $\lambda_{c3} = 0.725$, and $\lambda_{c4} = 0.8$. It is proposed to detect the cracks locally in the SS (member 4) of the frame using PZT : 5%, which is shown inside the dotted box in [Figure 16](#), left.

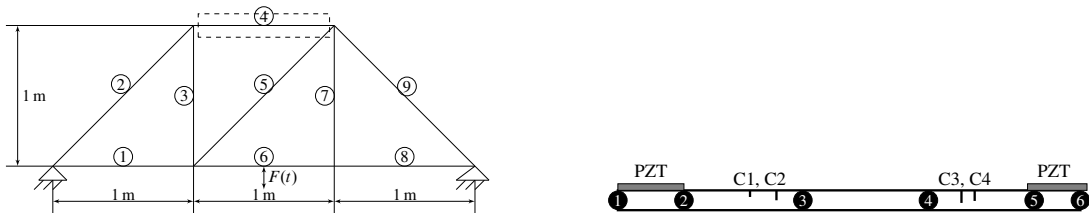


Figure 16. Frame structure. Left: global structure. Right: substructure of member four with six nodes.

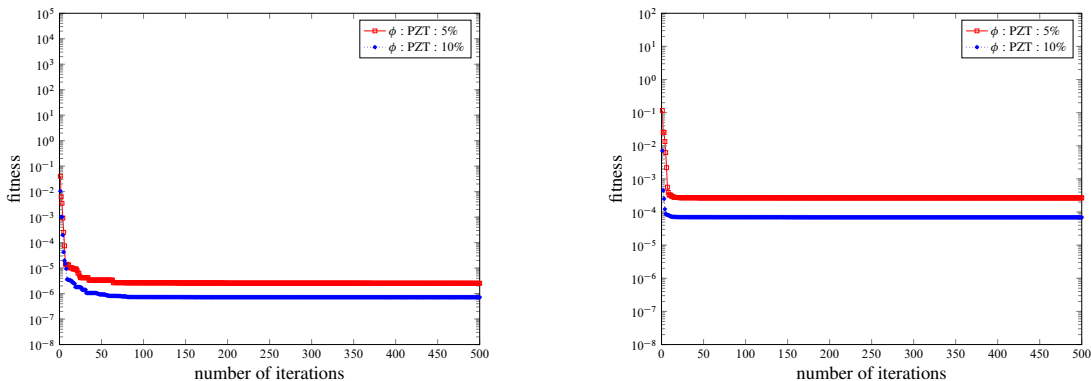


Figure 17. Convergence plot for multiple cracks with two double-cracks per beam element. Left: noise-free case. Right: 5% noise case.

The damping effect in the structure is modeled using Rayleigh’s damping model, with a damping ratio of 3%. The structure is excited by an impulse response of 10N over a time of 0.01 s, with a time step of 0.001 s, at the midpoint of member 6. Frame member 4 is divided into five elements as shown in Figure 16, right; the first two cracks lie on the element 2 and the remaining two cracks lie on the element 4. The normalized locations from the left end of the respective elements are $\lambda_{e2,1} = 0.5$, $\lambda_{e2,2} = 0.75$, $\lambda_{e4,1} = 0.25$, and $\lambda_{e4,2} = 0.5$ ($\lambda_{e2,1}$ means that crack 1 is in the element 2). The crack parameters are searched by PSO with swarm size 100 and 500 generations, as explained in the previous example. The identified parameters of absolute error are shown in Figure 18. The crack with smallest depth ($\xi = 0.05$) is identified with an absolute error of 5.3% without noise and 12.97% with 5% noise in measurement. The location of this crack is identified with an absolute error of 2.52% and 4.05% without and with 5% noise in measurement, respectively. The total time taken for the convergence is 215 s.

9. Experimental verification: fixed-fixed beam with PZT patches

A fixed-fixed beam made of acrylic material with dimensions 452 mm × 25 mm × 12 mm is used for the experimental study. Here two PZT patch of dimensions 25 mm × 25 mm × 1 mm each are bonded at the fixed ends of the structure as shown in Figure 19. The modulus of elasticity (E) was estimated to be 3.9 GPa from a simple bending test and the density was measured to be 1190 kg/m³. The actual flexural rigidity (EI) of the beam is 14.04 N · m². The damping ratio (ζ) was calculated from a simple free

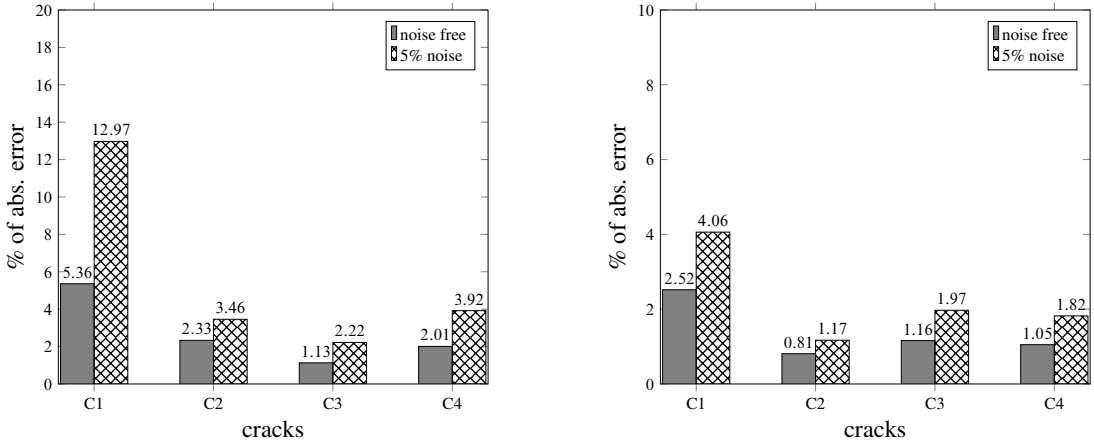


Figure 18. Absolute error in identified parameters in SS of frame with PZT: 5%. Left: depth. Right: location.

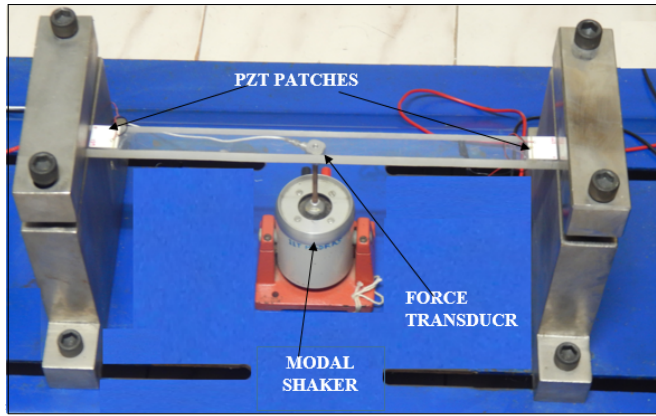


Figure 19. Experimental set up of fixed-fixed intact beam with PZT patch.

vibration decay test using logarithmic decrement and was estimated as 8%. The natural frequencies for the first two modes of the structure were calculated from the frequency domain as 110 Hz and 306 Hz.

The beam is excited by a sinusoidal force of $2.2 \sin(2\pi \times 68.3t)$ N at the middle of the structure by a LDS permanent magnet 20 N modal shaker with a maximum displacement of 5 mm with an operating frequency range of 5 Hz–13 kHz. The applied force is measured by using a KISTLER force transducer and is acquired with a sampling frequency of 1000 Hz using a DEWE 43 DAQ system. The dynamic voltage response is measured through two piezoelectric patches and it is sampled at a rate of 1000 Hz. The comparison of experimental and simulated voltage response (time and frequency domain) of the given intact beam is shown in Figure 20. One can find that difference in measured and calculated response is very small, which shows the one-dimensional (1-D) hybrid model is accurate.

Next, two open edge cracks of depths 6 mm and 1.5 mm are introduced on the same beam at a distances of 92 mm and 393.5 mm from the fixed end. The width of cut is 0.4 mm and close-up views of the cracks

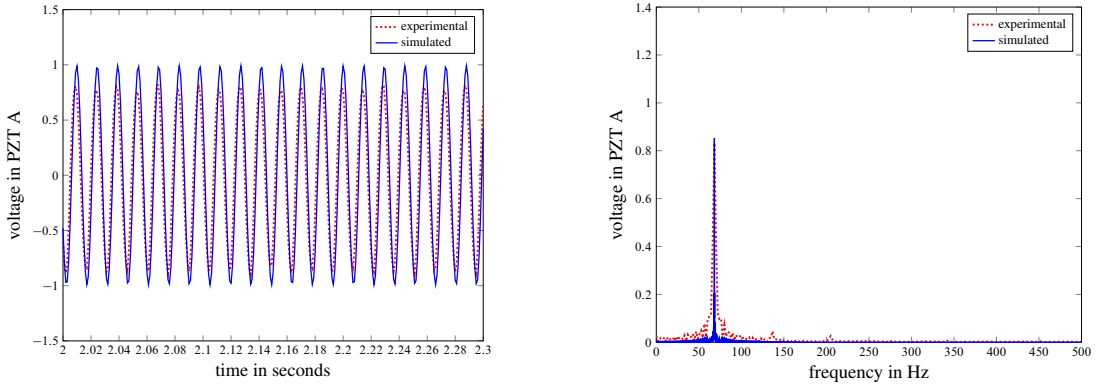


Figure 20. Experimental and simulated voltage response at PZT A. Left: time domain. Right: frequency domain.

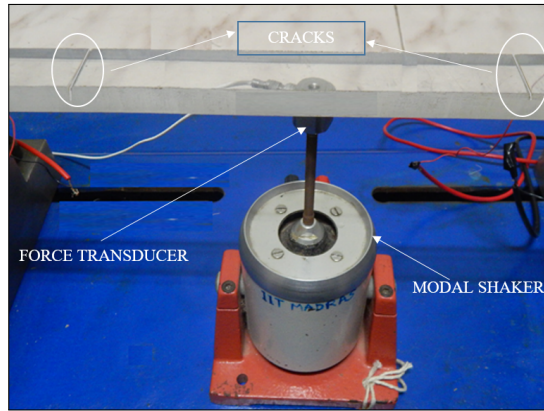


Figure 21. Cracks in the fixed-fixed beam.

are shown in [Figure 21](#). The nondimensional crack depth of each crack is $\xi_1 = 0.5$ and $\xi_2 = 0.125$, and their absolute location from the fixed end are $\lambda_1 = 0.2$ and $\lambda_2 = 0.87$, respectively. The beam is divided into five elements as in the previous numerical study, and here, the crack lies in the second and fourth elements, respectively. The nondimensional element-wise crack locations measured from the left node of the element are $\lambda_{e2} = 0.5$ and $\lambda_{e4} = 0.75$, respectively. The cracked structure is excited by a harmonic force of $2.8 \sin(2\pi \times 60.7t)$ N at a distance of 292 mm from the left fixed end. The voltage responses are measured through the PZT patches and it is sampled at a rate of 1000 Hz. From the acquired data, a portion of time histories of 5 s is considered for parameter identification. The parameters are searched between the feasible search range of zero and one by PSO (swarm size: 200, generations: 500) using the proposed voltage matching technique. Damage parameters are identified from six different trials of reading and mean values are presented in [Table 3](#). The smallest crack depth ($\xi = 0.125$) is identified with an absolute error of 12.56% in magnitude and 2.2% in its location. Similar to the numerical study, here identifying the crack location is more accurate than depth estimation.

exact crack depth ξ	exact absolute crack location λ	identified crack depth (% error)	identified crack location (% error)
0.5	0.2	0.5262 (−5.24)	0.1961 (1.95)
0.125	0.87	0.1093 (12.56)	0.8509 (2.2)

Table 3. Experimental identification (crack depth and location) of a multiple crack.

Now, the proposed method is compared with other similar experimental results in literature. Ding et al. [2017] estimated the crack parameters of two cracks (crack depth ratio $\xi = 0.1$) with crack locations ($\lambda_1 = 0.2$, $\lambda_2 = 0.45$) of a fixed-fixed beam using an improved artificial bee colony algorithm based on experimental frequency measurement data from [Khiem and Toan 2014]. There, the maximum identified crack depth and location error are 24% and 4% respectively. The proposed method has identified multiple cracks with a maximum absolute error of 12.56% and 2.2% respectively for crack and location.

10. Conclusions

This study presents a multiple crack detection scheme in beam structures by minimizing measured and predicted voltage responses of PZT patches. Unlike conventional accelerometer sensors, PZT patches have low cost and negligible weight, and a wide band width with the ability of dynamic measurement of distributed nature. A one-dimensional (1-D) hybrid beam element with a PZT sensor bonded to the beam represented by reduced material properties is used. Hitherto, the one-dimensional (1-D) patch with beam model was not used for structural identification, thereby unfolding a new model which is simple and convenient. The effect of different PZT lengths is investigated with numerical examples and the convergence of the fitness function of the cases are studied. Numerical examples show that the smallest patch length PZT: 5% (5% of the length of the beam) under study is sufficient enough for effective and accurate crack parameter identification. The proposed method estimated the crack depth error in the range of 0.66% to 12% and the location error in the range of 0.11% to 4% (noise-free and noisy case). The validation of the proposed method has also been carried out using experiments. The accuracy of the proposed method using the one-dimensional hybrid element model is found to be comparable or superior to some of the existing methods reviewed here.

References

- [Bendary et al. 2010] I. M. Bendary, M. Adnan Elshafei, and A. M. Riad, “Finite element model of smart beams with distributed piezoelectric actuators”, *J. Intell. Mater. Syst. Struct.* **21**:7 (2010), 747–758.
- [Benjeddou 2000] A. Benjeddou, “Advances in piezoelectric finite element modeling of adaptive structural elements: a survey”, *Compos. Struct.* **76**:1-3 (2000), 347–363.
- [Ding et al. 2017] Z. Ding, Z. Lu, M. Huang, and J. Liu, “Improved artificial bee colony algorithm for crack identification in beam using natural frequencies only”, *Inverse Probl. Sci. Eng.* **25**:2 (2017), 218–238.
- [Douka et al. 2004] E. Douka, G. Bamnios, and A. Trochidis, “A method for determining the location and depth of cracks in double-cracked beams”, *Appl. Acoust.* **65**:10 (2004), 997–1008.
- [Fukunaga et al. 2002] H. Fukunaga, N. Hu, and F.-K. Chang, “Structural damage identification using piezoelectric sensors”, *Int. J. Solids Struct.* **39**:2 (2002), 393–418.
- [Kapuria and Hagedorn 2007] S. Kapuria and P. Hagedorn, “Unified efficient layerwise theory for smart beams with segmented extension/shear mode, piezoelectric actuators and sensors”, *J. Mech. Mater. Struct.* **2**:7 (2007), 1267–1298.

- [Kennedy and Eberhart 1995] J. Kennedy and R. Eberhart, “Particle swarm optimization”, pp. 1942–1948 Proc. IEEE Int. Conf. Neural Netw. **1995**:4, IEEE, 1995.
- [Khiem and Toan 2014] N. T. Khiem and L. K. Toan, “A novel method for crack detection in beam-like structures by measurements of natural frequencies”, *J. Sound Vib.* **333**:18 (2014), 4084–4103.
- [Krawczuk et al. 2000] M. Krawczuk, A. Żak, and W. Ostachowicz, “Elastic beam finite element with a transverse elasto-plastic crack”, *Finite Elem. Anal. Des.* **34**:1 (2000), 61–73.
- [Lee and Shin 2002] U. Lee and J. Shin, “A frequency-domain method of structural damage identification formulated from the dynamic stiffness equation of motion”, *J. Sound Vib.* **257**:4 (2002), 615–634.
- [Liu et al. 2011] H. Liu, K. Xin, and Q. Qi, “Study of structural damage detection with multi-objective function genetic algorithms”, *Procedia Eng.* **12** (2011), 80–86.
- [Mohan et al. 2014] S. C. Mohan, A. Yadav, D. K. Maiti, and D. Maity, “A comparative study on crack identification of structures from the changes in natural frequencies using GA and PSO”, *Eng. Computation.* **31**:7 (2014), 1514–1531.
- [Mouser and Dunn 2005] C. R. Mouser and S. A. Dunn, “Comparing genetic algorithms and particle swarm optimisation for an inverse problem exercise”, *ANZIAM J.* **46** (2005), C89–C101.
- [Nandakumar and Shankar 2014] P. Nandakumar and K. Shankar, “Multiple crack damage detection of structures using the two crack transfer matrix”, *Struct. Health Monit.* **13**:5 (2014), 548–561.
- [Patil and Maiti 2005] D. Patil and S. Maiti, “Experimental verification of a method of detection of multiple cracks in beams based on frequency measurements”, *J. Sound Vibration* **281**:1 (2005), 439–451.
- [Perez and Behdinan 2007] R. E. Perez and K. Behdinan, “Particle swarm approach for structural design optimization”, *Comput. Struct.* **85**:19-20 (2007), 1579–1588.
- [Philips Adewuyi et al. 2009] A. Philips Adewuyi, Z. Wu, and N. H. M. Kammrujaman Serker, “Assessment of vibration-based damage identification methods using displacement and distributed strain measurements”, *Struct. Health Monit.* **8**:6 (2009), 443–461.
- [Sadílek and Zemčík 2010] P. Sadílek and R. Zemčík, “Frequency response analysis of hybrid piezoelectric cantilever beam”, *Eng. Mech.* **17**:2 (2010), 73–82.
- [Sekhar 2008] A. S. Sekhar, “Multiple cracks effects and identification”, *Mech. Syst. Signal Process.* **22**:4 (2008), 845–878.
- [Sinha et al. 2002] J. K. Sinha, M. I. Friswell, and S. Edwards, “Simplified models for the location of cracks in beam structures using measured vibration data”, *J. Sound Vib.* **251**:1 (2002), 13–38.
- [Sulbhewar and Raveendranath 2015] L. N. Sulbhewar and P. Raveendranath, “A numerically accurate and efficient coupled polynomial field interpolation for Euler–Bernoulli piezoelectric beam finite element with induced potential effect”, *J. Intell. Mater. Syst. Struct.* **26**:12 (2015), 1539–1550.
- [Verhese and Shankar 2014] C. K. Verhese and K. K. Shankar, “Damage identification using combined transient power flow balance and acceleration matching technique”, *Struct. Control Health Monit.* **21**:2 (2014), 135–155.
- [Viola et al. 2001] E. Viola, L. Federici, and L. Nobile, “Detection of crack location using cracked beam element method for structural analysis”, *Theor. Appl. Fract. Mech.* **36**:1 (2001), 23–35.
- [Viola et al. 2002] E. Viola, L. Nobile, and L. Federici, “Formulation of cracked beam element for structural analysis”, *J. Eng. Mech. (ASCE)* **128**:2 (2002), 220–230.
- [Wang et al. 2001] X. Wang, N. Hu, H. Fukunaga, and Z. H. Yao, “Structural damage identification using static test data and changes in frequencies”, *Eng. Struct.* **23**:6 (2001), 610–621.
- [Xu and ShengPeng 2013] L. Xu and S. ShengPeng, “Dynamic analysis of Bernoulli–Euler piezoelectric nanobeam with electrostatic force”, *Sci. China G Phys. Mech. Astronom.* **56**:10 (2013), 1930–1937.
- [Yang and Wang 2010] Z. Yang and L. Wang, “Structural damage detection by changes in natural frequencies”, *J. Intell. Mater. Syst. Struct.* **21**:3 (2010), 309–319.
- [Zemčík and Sadílek 2007] R. Zemčík and P. Sadílek, “Modal analysis of beam with piezoelectric sensors a actuators”, *Appl. Comput. Math.* **1** (2007), 381–386.

Received 15 Jun 2017. Revised 9 Oct 2017. Accepted 17 Apr 2018.

NARAYANAN JINESH: jineshkarthi@gmail.com

Department of Mechanical Engineering, Indian Institute of Technology, Chennai, India

KRISHNAPILLAI SHANKAR: skris@iitm.ac.in

Department of Mechanical Engineering, Indian Institute of Technology, Chennai, India

SUBMISSION GUIDELINES

ORIGINALITY

Authors may submit manuscripts in PDF format online at the Submissions page. Submission of a manuscript acknowledges that the manuscript is original and has neither previously, nor simultaneously, in whole or in part, been submitted elsewhere. Information regarding the preparation of manuscripts is provided below. Correspondence by email is requested for convenience and speed. For further information, write to contact@msp.org.

LANGUAGE

Manuscripts must be in English. A brief abstract of about 150 words or less must be included. The abstract should be self-contained and not make any reference to the bibliography. Also required are keywords and subject classification for the article, and, for each author, postal address, affiliation (if appropriate), and email address if available. A home-page URL is optional.

FORMAT

Authors can use their preferred manuscript-preparation software, including for example Microsoft Word or any variant of $\text{T}_{\text{E}}\text{X}$. The journal itself is produced in $\text{L}^{\text{A}}\text{T}_{\text{E}}\text{X}$, so accepted articles prepared using other software will be converted to $\text{L}^{\text{A}}\text{T}_{\text{E}}\text{X}$ at production time. Authors wishing to prepare their document in $\text{L}^{\text{A}}\text{T}_{\text{E}}\text{X}$ can follow the example file at www.jomms.net (but the use of other class files is acceptable). At submission time only a PDF file is required. After acceptance, authors must submit all source material (see especially Figures below).

REFERENCES

Bibliographical references should be complete, including article titles and page ranges. All references in the bibliography should be cited in the text. The use of $\text{BibT}_{\text{E}}\text{X}$ is preferred but not required. Tags will be converted to the house format (see a current issue for examples); however, for submission you may use the format of your choice. Links will be provided to all literature with known web locations; authors can supply their own links in addition to those provided by the editorial process.

FIGURES

Figures must be of publication quality. After acceptance, you will need to submit the original source files in vector format for all diagrams and graphs in your manuscript: vector EPS or vector PDF files are the most useful. (EPS stands for Encapsulated PostScript.)

Most drawing and graphing packages—Mathematica, Adobe Illustrator, Corel Draw, MATLAB, etc.—allow the user to save files in one of these formats. Make sure that what you’re saving is vector graphics and not a bitmap. If you need help, please write to graphics@msp.org with as many details as you can about how your graphics were generated.

Please also include the original data for any plots. This is particularly important if you are unable to save Excel-generated plots in vector format. Saving them as bitmaps is not useful; please send the Excel (.xls) spreadsheets instead. Bundle your figure files into a single archive (using zip, tar, rar or other format of your choice) and upload on the link you been given at acceptance time.

Each figure should be captioned and numbered so that it can float. Small figures occupying no more than three lines of vertical space can be kept in the text (“the curve looks like this:”). It is acceptable to submit a manuscript with all figures at the end, if their placement is specified in the text by means of comments such as “Place Figure 1 here”. The same considerations apply to tables.

WHITE SPACE

Forced line breaks or page breaks should not be inserted in the document. There is no point in your trying to optimize line and page breaks in the original manuscript. The manuscript will be reformatted to use the journal’s preferred fonts and layout.

PROOFS

Page proofs will be made available to authors (or to the designated corresponding author) at a Web site in PDF format. Failure to acknowledge the receipt of proofs or to return corrections within the requested deadline may cause publication to be postponed.

Journal of Mechanics of Materials and Structures

Volume 13, No. 2

March 2018

- A simple technique for estimation of mixed mode (I/II) stress intensity factors**
SOMAN SAJITH, KONDEPUDI S.R.K. MURTHY and PUTHUVEETIL S. ROBI 141
- Longitudinal shear behavior of composites with unidirectional periodic nanofibers of some regular polygonal shapes**
HAI-BING YANG, CHENG HUANG, CHUAN-BIN YU and CUN-FA GAO 155
- Fracture initiation in a transversely isotropic solid: transient three dimensional analysis** LOUIS M. BROCK 171
- Eshelby inclusion of arbitrary shape in isotropic elastic materials with a parabolic boundary** XU WANG, LIANG CHEN and PETER SCHIAVONE 191
- Burmister's problem extended to a microstructured layer** THANASIS ZISIS 203
- Multiple crack damage detection of structures using simplified PZT model**
NARAYANAN JINESH and KRISHNAPILLAI SHANKAR 225